Rupert Draxelmayr, Graz University of Technology, BSc

Persistent Luminescence of Strontiumaluminate Doped and Co-doped with Rare Earth Ions

MASTER'S THESIS

to achieve the university degree of

Master of Science

Master's degree programme: Chemistry

submitted to

Graz University of Technology

Supervisor

Ao.Univ.-Prof.Dipl.-Ing.Dr.techn. Karl Gatterer

Institute of Physical and Theoretical Chemistry

Graz, September 2015

AFFIDAVIT

I declare that I have authored this thesis independently, that I have not used other than the declared sources/resources, and that I have explicitly indicated all material which has been quoted either literally or by content from the sources used. The text document uploaded to TUGRAZonline is identical to the present master‘s thesis dissertation.

Date

Signature

Danksagung

Zu aller erst und möchte ich meinem Betreuer Ao.Univ.-Prof. Dipl.-Ing. Dr.techn. Karl für das zur Verfügung stellen des Themas, für seine großartige Unterstützung und auch für seine menschliche Art ein herzliches und lautes Dankeschön aussprechen.

Weiters gilt mein Dank auch Ao.Univ.-Prof. Dipl.-Ing. Dr.techn. Franz-Andreas Mautner und Oberrätin Dipl.-Ing. Dr.techn. Brigitte Bitschnau, die für mich die Röngenbeugungsexperimente durchgeführt haben und mir bei der Auswertung der Spektren zur Verfügung gestanden sind.

Ein weiteres Dankeschön geht an Amtsrätin Ing. Josefine Hobisch, welche die TGA-Messungen vorgenommen hat.

Auch möchte ich mich bei Oberrat Dipl.-Ing. Dr.techn. Univ.-Doz. Peter Pölt, Dipl.-Ing. Dr.techn. Angelika Reichmann sowie auch den Laborantinnen und Laboranten des Instituts für Elektronenmikroskopie und Nanoanalytik bedanken, die für mich die Probenvorbereitungen und elektromikroskopischen Messungen durchgeführt haben.

Überdies bedanke ich mich bei Ing. Helmut Eisenkölbl, der mir bei der technischen Durchführung immer dann wenn es nötig war geholfen hat, sowie auch bei Hilde Freißmuth und Ines Anna Gössler, die mir die Chemikalien zur Verfügung gestellt haben.

Zu guter letzt bedanke ich mich bei meiner Familie und allen mir Nahestehenden, die mich die ganze Arbeit über unterstützt haben und mir beigestanden sind.

Abstract

Eu-doped $SrAl_2O_4$ is known as a phosphor showing an extremely long afterglow. In the frame of this thesis undoped $SrAl_2O_4$, singly doped $SrAl_2O_4$: RE (RE = Eu, Dy, Nd, Pr, Sm) and co-doped $SrAl_2O_4$: Eu, RE (RE = Dy, Nd, Pr, Sm) were synthesised by the solution combustion method followed by sintering under reducing atmosphere. The samples were analysed by X-ray diffraction (XRD), scanning electron microscopy (SEM), reflectance spectroscopy and fluorescence spectroscopy. The XRD shows that a single sintering step yields the best results in terms of crystallinity, purity and preparative effort. The optical band gap was calculated via a Tauc plot by using the reflectance spectrum. The SEM showed that the microstructure of $SrAl_2O_4$ is dominated by domains. The co-doped samples revealed that the afterglow can be influenced by co-doping and temperature. The rare earths Dy and Nd promoted the afterglow considerably, Pr promoted it slightly and Sm even diminished it. Furthermore, the persistent luminescence is upgraded by low temperatures and downgraded by high temperatures.

Kurzfassung

Eu-dotiertes $SrAl_2O_4$ ist als Leuchtstoff mit einem extrem langen Nachleuchten bekannt. In dieser Arbeit wurde undotiertes $SrAl_2O_4$, einfach dotiertes $SrAl_2O_4$: RE (RE = Eu, Dy, Nd, Pr, Sm) und co-dotiertes $SrAl_2O_4$: Eu, RE (RE = Dy, Nd, Pr, Sm) mittels *solution combustion*, gefolgt von einer Sinterung unter reduzierender Atmosphäre, hergestellt. Die Proben wurden mit den Methoden der Röntgenbeugung, Rasterelektronenmikroskopie, Reflexionsspektroskopie und Fluoreszenzspektroskopie untersucht. Die Röntgenbeugung zeigte, dass ein einzelner Sinterschritt die besten Ergebnisse bezüglich Kristallinität, Reinheit und präparativem Aufwand liefert. Die optische Bandlücke wurde mit Hilfe einer Tauc-Auftragung, unter Verwendung des Reflexionsspektrums, berechnet. Die rasterelektronenmikroskopischen Untersuchungen zeigten, dass die Mikrostruktur von $SrAl_2O_4$ von Domänen beherrscht wird. Die co-dotierten Proben legten offen, dass das Nachleuchten durch Co-Dotierung und Temperatur beeinflusst werden kann. Die Seltenenerdionen Dy und Nd verlängern das Nachleuchten erheblich, Pr nur leicht und Sm verkürzt es sogar. Weiters verlängern tiefe Temperaturen das Nachleuchten, wohingegen hohe Temperaturen es verkürzen.

Contents

Abstract vii

1. Introduction 1

1.1. Luminescence . . . 1

1.1.1. The Origin of Luminescence . . . 1

1.1.2. Luminescent Materials and Applications . . . 2

1.1.3. Eu-doped and co-doped $SrAl_2O_4$ - State of the Art . . . 5

1.2. Theoretical Part . . . 6

1.2.1. Rare-Earth Spectroscopy . . . 7

1.2.2. Crystal Field (CF) - Theory and its Effect on Eu^{2+} . . . 12

1.2.3. Possible Mechanisms . . . 15

1.3. Overview and Objectives . . . 23

2. Used Equipment, Chemicals and Methods 26

2.1. Instruments and Equipment . . . 26

2.2. Chemicals . . . 26

2.3. Solution Combustion . . . 27

3. Experimental Part 29

3.1. Sample Preparation . . . 29

3.2. Optical Measurements . . . 34

3.3. Scanning Electron Microscopy . . . 36

3.4. X-ray Diffraction . . . 36

4. Results and Discussion 38

4.1. The Host Material . . . 38

4.1.1. Crystallographic Characterisation . . . 38

4.1.2. Scanning Electron Microscopy 44
4.1.3. Optical Characterisation 51
4.2. $SrAl_2O_4$:RE - Singly Doped $SrAl_2O_4$ 53
4.2.1. Optical Characterisation with the UV Lamp 53
4.2.2. Optical Characterisation with the Fluorescence Spectrometer . . 55
4.3. $SrAl_2O_4$:Eu,Dy – Eu and Dy doped $SrAl_2O_4$ 70
4.3.1. Optical Characterisation with the UV Lamp 70
4.3.2. Optical Characterisation with the Fluorescence Spectrometer . . 71
4.4. $SrAl_2O_4$:Eu,RE – Co-doped $SrAl_2O_4$ 83
4.4.1. Optical Characterisation with the UV Lamp 83
4.4.2. Optical Characterisation with the Fluorescence Spectrometer . . 84
4.4.3. Temperature Dependence of Co-doped $SrAl_2O_4$ 92
4.4.4. Mechanism of the Afterglow of Co-doped $SrAl_2O_4$ 95

5. Summary **100**

Appendix **103**

A. Eu Containing Compounds **104**

B. $SrAl_2O_4$: Nd (100%) **111**

C. Dieke Diagram **114**

D. EDXA of Figure 4.14 **116**

Bibliography **119**

1. Introduction

1.1. Luminescence

1.1.1. The Origin of Luminescence

Imagine you are roused on a Monday morning by your alarm clock. You search the red digits of your timer and realize that it is time to go to work. You have breakfast while you are watching the six o'clock news on your plasma TV. You get out of your house as your smart phone rings. You read the message from its flat illuminated display and get into your car. The headlights of your car lighten the dark streets. You pass some flashing advertising while you take a quick look onto the greenish glowing hands of your wristwatch. You are in time ...

This short introduction makes clear that luminescence is a phenomenon that is an omnipresent part of our modern life style. However, what exactly is luminescence? According to IUPAC luminescence is a *"spontaneous emission of radiation from an electronically or vibrationally excited species not in thermal equilibrium with its environment"* [1]. Expressed in more detail the process of luminescence consists of three steps: energy absorption, energy transfer and emission of a photon [2]. The absorption of energy can be implemented by chemical reactions, ultra sound, heat, mechanical energy or by interaction with highly energetic particles, light or voltage [3]. After absorption the energy is transferred to the active luminescence centre. This can either happen via migration of electric charge (hole or electron), via excitons, via resonance of atoms with overlapping orbitals or via reabsorption of photons that were emitted by another excited atom [2]. If the energy is not lost during the transfer process it will cause an excitation of the active luminescence centre. Finally the excited atom relaxes by emitting a photon of certain energy. The most common relaxation steps are intra-configuration

transitions (e.g. $Eu^{3+}(4f^6)^* \rightarrow Eu^{3+}(4f^6) + h\nu$), inter-configuration (IC) transitions (e.g. $Eu^{2+}(4f^6 5d^1)^* \rightarrow Eu^{2+}(5f^7) + h\nu$), recombinations ($h^+ + e^- \rightarrow h\nu$) and charge transfer (CT) transitions (e.g. $O^{2-} + Mn^{7+} \rightarrow O^{1-} + Mn^{6+} + h\nu$). Independent of the mechanism the materials can glow for a certain length of time. This phenomenon is called afterglow or persistent luminescence. It can last for hours after energy absorption. The term afterglow is sometimes mixed with the term phosphorescence [4]. Phosphorescence is a process that is delayed because forbidden transitions are engaged in the excitation-emission process. Persistent luminescence, however, is a process that is delayed due to a trapping-de-trapping mechanism. Holes or electrons are captured by traps and released depending on the particles thermal energy. This mechanism is mostly different for each compound.

1.1.2. Luminescent Materials and Applications

This section will introduce some common luminescent materials. It will focus on inorganic materials. Roughly speaking they usually consist of an activator atom embedded into a matrix - the host material. These activator atoms are mostly transition metals or rare earth ions. Their doping concentrations are usually small.

One of the first well investigated luminescent materials was ZnS [4]. Depending on its dopants it can glow in different colours. Doping with Ag will lead to a blue luminescence whereas Au and Al causes a green and the substitution of Zn with Cd a red emission. The mechanism is based on a CT from a Cl ion (impurities) to the transition metal ion. However, its persistent luminescence is short and weak. Therefore radioactive atoms (Pm) were added to enhance the afterglow. This and its instability against moisture were the reasons why it was rejected for technological applications.

Another luminescent material is $CdSiO_3$: Mn^{2+}, RE^{3+} where RE equals Tb, Eu and Nd [5]. The RE co-dopants do not influence the colour of the afterglow which is orange. However, they effect the duration of the afterglow that can last up to five hours by doping with Eu. The emission is based on a $5d \rightarrow 5d$ transition of Mn^{2+}. The co-dopants supply the traps for the electrons. The host material $CdSiO_3$ forms an edge-sharing chain of SiO_4 tetrahedra. This allows an embedding of ions with different sizes leading to a wide variability of trap depths.

Y_2SiO_5:Ce^{3+} is a material that shows a green emission [6]. There are two different Ce sites. The illumination light excites the electrons from the VB to some defect levels in the band gap. This leads to the creation of a hole. When the hole and the electron recombine the energy is transferred to the Ce ion leading to an excitation to the 5d state. The resulting emission is an IC transition.

$Ca_2MgSi_2O_7$: Eu^{2+} is another luminescence material doped with rare earth ions [7]. The transition is a IC and corresponds to blue light. Co-dopants like Nd can again influence the duration and intensity of the afterglow. The host material is comparatively stable and shows a good luminescence efficiency. Moreover, the material is easy and cheap to synthesise [4].

However, one of the currently most researched luminescent materials is $SrAl_2O_4$ doped with Eu^{2+} and co-doped with other REs. This material is the subject of the master thesis and will be discussed in the next section in more detail.

All these materials differ in their intensity, hue, saturation, afterglow duration and maintenance. Hence they can be used for different applications that have diverse demands for the luminescence properties of the materials [2].

One big field of application is the illumination industry. The luminescent materials need to feature a high light output and a high colour rendering. Moreover, its maintenance should be as high as possible. About 90% of the artificially generated light originates from discharge lamps. The most widespread discharge lamp is based on mercury. The energy of the emitted light depends on the pressure in the lamp.

A low pressure will lead to the emission of sharp lines within the UV and only weak lines in the blue and green range of the visible light. The latter are, however, too weak for lighting applications. Therefore the emitted UV is used do excite a mix of luminescent materials coated on the lamp's mantle. The emitted light will depend on the composition of the luminophores. Their application field exceeds the conventional fluorescence lamps. It is also used for applications like sun-tanning, photocopy machines, blacklight, advertising billboards and display backlights.

At high pressures, however, a mercury discharge lamp will lead to broad emissions of blue and green light. This emissions can be used for illumination but there is still a lack of red light. This can be compensated by using materials that show red luminescence.

Another element that can be used in discharge lamps is Xe. It has some advantages to Hg. However, there is still a lot of research to do.

An alternative to light sources based on discharge lamps are light emitting diodes (LEDs). They are based on converting an electric current to luminescence. There are two different concepts to obtain LEDs that emit white light. The first is based on combining a UV emitting LED with three different materials that emit blue, green and red light under UV excitation, respectively. They are called cluster-lamps. The second possibility is by combining a blue LED source with materials that absorb parts of this initial source and converts it to green, yellow or red light. As a result white light is emitted. Although their efficiency is currently worse than that one for low pressure discharge lamps they have much future potential.

The next important field of application is the screen and display industry. In contrast to materials for illumination purposes they must have a high colour saturation to generate as much colours as possible within the colour triangle of the chromaticity diagram. Two old and well researched concepts for TV and PC screens are the cathode ray tube (CRT) and projection TV (PTV). They are based on luminescent materials. Although their mechanisms are different they both use the combination of red, green and blue light to generate all possible colours within the colour triangle. However, more modern implementations for flat displays of smart phones, note books, TVs and other devises are required. The technology used for smaller screens will mostly be based on liquid crystal technology (LCT), which is a non-emissive display. For larger displays, however, a number of different technologies using luminescence as light source are used. Three examples are the low voltage display (analogous to CRT), the plasma display (based on plasma discharge) and the electroluminescence (analogous to LED).

The applications and technologies mentioned above have revolutionized the lighting market. Efficiency and light quality were considerably improved in the last years. Further research and development of technology based on luminescent materials is therefore likely. However, there is still a long way to go and further research is necessary.

1.1.3. Eu-doped and co-doped $SrAl_2O_4$ - State of the Art

Up to now there have been published over 100 papers dealing with $SrAl_2O_4$: Eu and its co-doped variants. To review all of them would be beyond the scope of the following discussion. Hence only research work that is important for the work of this master thesis will be mentioned.

The host material $SrAl_2O_4$ exists in different modifications [8]. At ambient temperatures it has a primitive monoclinic lattice. This modification is called α-phase. Moreover there exist two further modifications at higher temperatures. They are called β- and β'-phases. The transitions take place at 680°C and 860°C, respectively.

Matsuo et al. did detailed investigations with electron microscopy relating to the microstructure of the α-phase [8]. It was found out that there are three microstructures which consist of different variants of the α-phase. They form domains which differ in their twin relationship.

The first doped variant - $SrAl_2O_4$: Eu^{2+} - was discovered by Lange in 1966 [9]. The material shows green luminescence at a wavelength of 520 nm. Lange synthesised the material by a solid state reaction under reducing conditions.

In 1996 Matsuzawa et al. synthesised the first Dy and Nd co-doped material [10]. It was found that co-doping enhances the intensity of the afterglow considerably and also proposed a possible mechanism. This mechanism, however, was questioned and rebutted by several other researches (see section 1.2.3). Moreover it was figured out that the doping concentrations of 1% Eu and 2% Dy reveal the best afterglow properties.

The composition of the host material and the doping concentration of singly doped $SrAl_2O_4$ were investigated by other research groups. The best Sr-Al mole fraction for luminescence was determined by Katsumata et al. [11]. It was figured out that from all samples with 0.5% Eu and Dy the sample with the composition of $Sr_{0.95}Al_{1.95}O_4$: Eu, Dy (0.05;0.05) shows the most intense luminescence and afterglow. However, the composition $Sr_{1-(x+y)}Al_2O_4$: Eu, Dy (x;y) was preferred by many other groups. Wang et al. figured out that the fluorescence for singly doped $SrAl_2O_4$ is highest at a doping concentration of 6.6% Eu [12]. The co-doping was further investigated by Katsumata et al. [13]. It was found out that the fluorescence intensity as well as the intensity of the afterglow depend on the co-dopants. They were classified into strong, mid and weak

promoters. The rare earths Dy, Nd and Tm are strong whereas the elements Y and Sm are weak promoters. All other rare earth ions lead to a mid promotion of the afterglow.

Other research groups focused on the parameters of the synthesis. In 1990 Kingsley et al. discovered a new synthesis method by coincidence [14]. It became commonly known as the solution combustion method (see section 2.3). This method usually needs a post-annealing step to obtain an adequate reduction of the Eu^{3+}. It was, however, shown by Qiu et al. that Eu^{2+} is already reduced during the solution combustion by using an excess of the fuel [15]. It was figured out that using a lid during the combustion in the furnace leads to higher luminescence intensities.

A complete reduction, however, is only possible with a post-annealing step. The temperature and duration of the post-annealing and the used reducing agent varies from paper to paper. The temperature reached from 1000°C up to over 1500°C and the duration varied from 2 to 6 hours. The reducing agents were mostly a mixture of H_2 and N_2 or active carbon. Peng et al. for instance prepared their samples by solution combustion followed by a post-annealing at 1100°C for 2 hours in an active carbon atmosphere [16]. They compared them with samples prepared by solid state reaction. It was found out that the luminescence properties of the samples prepared by solid state reaction are better than those prepared by solution combustion. They have, however, a worse crystallinity and are less single phase. Some other parameters for the solution combustion were optimised by Yu et al. [17]. It was found out that a combustion temperature of 600°C yields the best results in terms of purity and crystallinity. Moreover, they claimed that a fuel to oxidant ratio of 1.5 leads to the highest extent of Eu reduction. Shafia et al. agreed with the combustion temperature but not with the oxidant to fuel ratio [18]. They claimed that a ratio of 2.5 will yield the best emission intensity.

1.2. Theoretical Part

This section gives an overview on all concepts that are required to follow the thesis' work, results and conclusions. It will start with a brief introduction into rare earth spectroscopy and takes some basic knowledge about solid state spectroscopy for granted. The first part of this section will discuss the electron configurations of rare-earths and

the Hamiltonian describing their energy level structure. From this the general features of rare earth spectra are deduced and are followed by an overview of the crystal field theory. Hence the effect of the immediate surrounding of a rare-earth ion on its spectroscopic properties will be discussed. The focus will be on the differences in the spectra of Eu^{3+} and Eu^{2+} in solids. Finally there will be a discussion of several concepts or models that were published over the last years in order to explain the long persistent afterglow of co-doped $SrAl_2O_4$: Eu^{2+}.

In the following sections the term rare-earth will be abbreviated by RE for reasons of convenience.

1.2.1. Rare-Earth Spectroscopy

The seventeen rare-earth elements, as defined by *IUPAC*, consist of the fifteen lanthanides and the two elements scandium and yttrium. In their elemental state they show the typical metallic lustre. This has its origin in the reflection of light on a metal surface. In compounds, however, the REs exist mainly in the oxidation state of 3+ [19]. Their electron configuration is [Xe]$4f^n$. (For Sc it is: [Ar] and for Y it is: [Kr]). The ionic state of the lanthanides is responsible for the chromophoric absorption and emission processes. The existence of an unfilled 4f-shell and the possibility of transitions within this shell (f-f transitions) are of vital importance. As is shown in figure 1.1 the 4f-orbitals penetrate the core much better than the orbitals of the next higher shells. Nevertheless they are a partly filled shell and enable therefore transitions of electrons. In addition, they are almost perfectly shielded by the 5s and 5p orbitals or additionally by the 6s in the case of the elemental REs. This makes the energy levels of 4f electrons nearly independent of the surrounding as long as transitions occur within the same configuration. Hence trivalent ions embedded in an arbitrary matrix will always show the same colours (i.e. they will have absorption or emission bands at the same wavelengths). However, certain rules must be obeyed in order to give rise to visible optical phenomena. First, an unfilled electron shell must exist. Elements with noble gas configuration (i.e. filled shells) do not feature electrons that can be excited easily. One example is La^{3+}. Here the unoccupied 4f orbitals that constitute the next higher energy levels are about 5 eV over the top of the valence band. This corresponds to a wavelength that is much

shorter than that of visible light. Thus lanthanum ions do not directly contribute to the colouring of a material. Consequently, the elements scandium, yttrium, lanthanum and lutetium do not come into consideration when optical phenomena in the visible range are of interest. Second, the transitions between the considered energy states must be in the visible range. This requires knowledge about the energy level diagram of a given ion and the spacing of its energy levels. A possible derivation of these energy levels can be given by quantum chemistry.

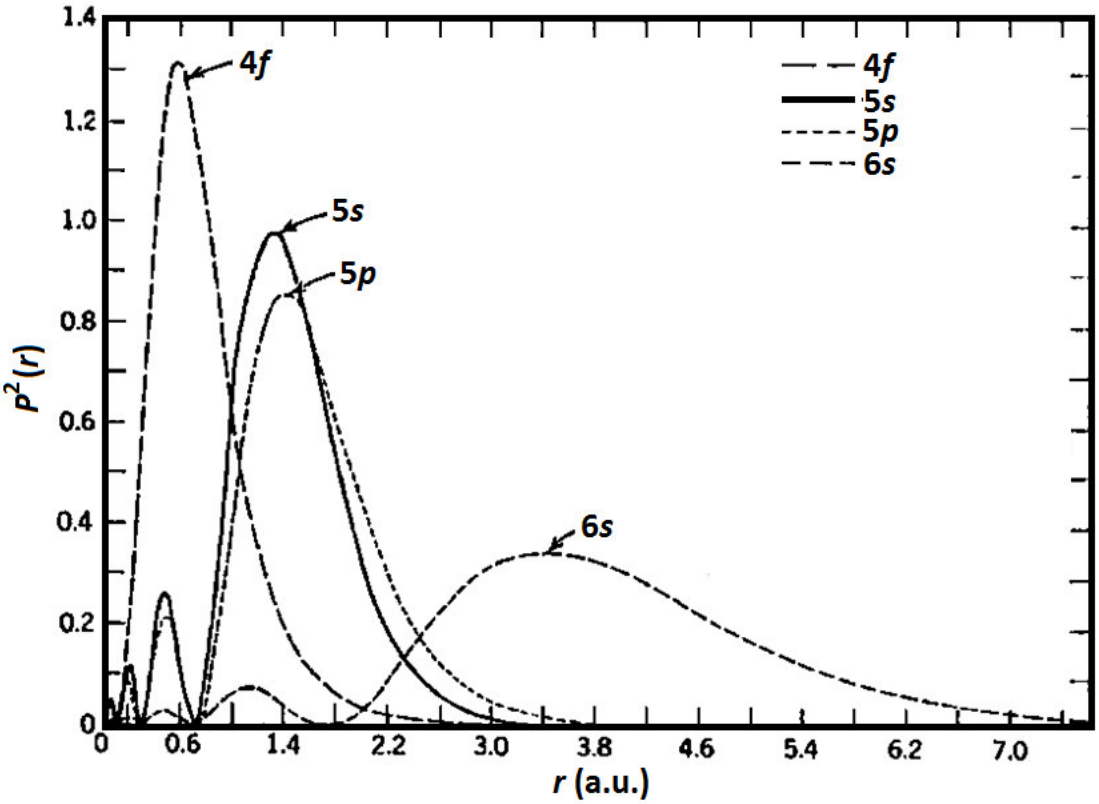

Figure 1.1.: The hydrogen type radial probability density $P^2(r)$ (= $\Psi(x)^2$) [20]: they show that 4f penetrates the core much better than the next higher shells with n=5, 6.

Here the problem can be represented as an eigenvalue equation involving perturbation theory

$$\hat{H}\Psi_i = E_i\Psi_i \qquad \text{with} \qquad \hat{H} = \hat{H}_0 + \hat{H}_1 \tag{1.1}$$

Here $\hat{H}_0$ is the unperturbed Hamiltonian operator, $\hat{H}_1$ the perturbation, Ψ_i the wave

function and E_i are the corresponding energies. Because transitions take place between electronic states the system can be adequately described by an electronic wave function. Closed shells are not taken into account because they barely influence the relative energies. A convenient formulation for such a function is a Slater Determinant. It is a mathematical concept that allows the description of an antisymmetric wave function and additionally satisfies the Pauli Exclusion Principle.

$$\Psi(x_1, x_2, ..., x_n) = (n!)^{-1/2} \begin{vmatrix} \chi_i(x_1) & \chi_j(x_1) & ... & \chi_k(x_1) \\ \chi_i(x_2) & \chi_j(x_2) & ... & \chi_k(x_2) \\ ... & ... & ... & ... \\ \chi_i(x_n) & \chi_j(x_n) & ... & \chi_k(x_n) \end{vmatrix} \tag{1.2}$$

Here the x_i represent the three spatial coordinates of an electron and its spin. The χ_i are one-electron wavefunctions. The Slater Determinant depends on the quantum numbers n, l, m_l, s and m_s. Because in this model only transitions between 4f configurations are considered there is an easy way to find out how many possible Slater Determinants exist for the perturbation ansatz. It can be treated as the problem of distributing n particles (electrons or holes) into 14 boxes (the spin orbitals). Because electrons are indistinguishable particles the number of possibilities (i.e. the number of Slater Determinants) can be easily obtained from the binomial coefficient

$$\frac{N!}{(N-n)!n!} \tag{1.3}$$

With N as the number of boxes and n as the number of electrons or holes (here holes are empty spin orbitals). The distribution does not depend on the nature of the particles, hence electrons and holes are equivalent. Here applies the so-called electron-hole formalism. It states that two configurations whose number of electrons and holes are the same coincide in the number and type of energy levels.

For the $4f^2$ or $4f^{12}$ configuration for example N equals 14 and n equals 2 or 12 respectively. This gives 91 possible ways to distribute the 2 or 12 electrons or more precisely 91 different micro states. Hence 91 Slater Determinants will be necessary to describe such a configuration. For the unperturbed system they are all degenerate. In

the case of Eu^{3+} ([Xe]$4f^6$) the impressive number of 3003 Slater Determinants results. In order to arrive at an energy level structure a further treatment with the perturbation operator is necessary. $\hat{H}_1$ consists of

$$\hat{H}_1 = \hat{H}_C + \hat{H}_{SO} + (\hat{H}_{CF}) \tag{1.4}$$

Here $\hat{H}_C$ describes the Coulomb interaction of the 4f electrons, $\hat{H}_{SO}$ the spin-orbit coupling and $\hat{H}_{CF}$ the influences of the crystal field (CF). The two perturbations $\hat{H}_C$ and $\hat{H}_{SO}$ are much larger than the $\hat{H}_{CF}$ and are therefore discussed in more detail. Their influence on the electronic energy levels is shown in figure 1.2.

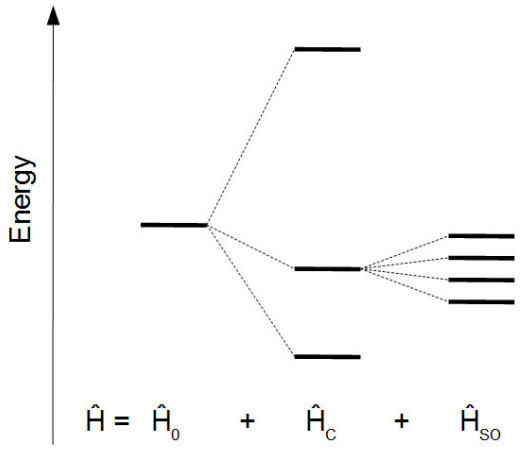

Figure 1.2.: The Hamiltonian and its effect on the splitting of the energy levels: every additional perturbation term leads to a splitting of the energy levels.

In the unperturbed situation there is no electron correlation included. Each electron is in its individual state described by m_l and m_s. In the real situation, however, the movement of the electrons is correlated. Hence the formerly independent angular and spin momenta need to be coupled. As a result the fully degenerate micro states are split by $\hat{H}_C$. These energy states are called Russell-Saunders terms and depend on the total quantum numbers L and S. For convenience in the following discussion the term Russell-Saunders will be abbreviated as RS. Each of them can be described as a linear combination of the Slater determinants that generate the orthonormal basis of a Hilbert space. Consequently the RS wave functions conceal the information about the

individual electrons.

The perturbation of $\hat{H}_{SO}$ is of about the same magnitude as the $\hat{H}_C$ when rare-earth ions are considered. It involves the coupling of the orbital angular momentum L with the spin angular momentum S to a total angular momentum J. The energy levels are split further into the so-called RS multiplets. The spin orbit coupling wave functions can be again described as a linear combination of RS wave functions. For a state with a given value of J all RS terms whose S and L vectors can generate the demanded value of J will contribute to the linear combination. Consequently, there are also included terms with different spin multiplicity and orbital angular momenta. The RS multiplets are therefore mixtures of states with different S and L. Thus, the spin selection rule plays a negligible role in RE spectroscopy.

Which of the RS terms is the lowest in energy (i.e. the ground state) can be derived from Hund's rules. These rules demand that terms with highest spin multiplicity are always the lowest in energy. Furthermore if there are several terms with the same spin multiplicity the term with the highest L is the lowest. If there are again terms with the same values of S and L for less than half-filled shells the term with the smallest J value is the ground state and for more than half-filled shells the state with the highest J value is the ground state.

The CF operator leads to a further splitting of the RS multiplets. Because the spacing is, however, only approximately 100 cm^{-1} in many cases it can be neglected and the REs can be considered as free ions. This is due to the inner-shell nature of 4f electrons as was explained earlier. The CF operator will not be considered in this thesis for Eu^{3+} because it does not affect the eigenvalues a great deal. CF effects will, however, turn out to be important for the Eu^{2+} ion (see section 1.2.2).

The total energy of the resulting states are obtained as eigenvalues of the perturbation ansatz. Because the radial integrals include many-body expressions these integrals cannot be solved exactly. Hence, it is common practice in RE spectroscopy to introduce adjustable parameters, the Racah parameters, for these integrals. These parameters are then chosen such that the calculated energy levels fit perfectly with experimental spectra. A very convenient diagram showing the energy levels of all RE ions is the Dieke diagram (see figure C.1 in appendix). With its help bands in the spectra can

be easily assigned to transitions between corresponding energy levels. Incidentally, the Dieke diagram nicely displays the electron-hole formalism. Ce^{3+} and Yb^{3+}, for example, have the same RS multiplets but the order is inverted.

The previous paragraphs explain why transition metal spectra look so much different from RE spectra. The latter seem more atom-like. This is because the 4f electrons are well shielded from electrostatic fields in their environment by the next higher fully occupied shells. As a result the bands are sharp and do not depend much on the details of the surrounding. This is a difference to transition metal spectra that show broad bands and are highly sensitive to variations of the CF. Another difference is the much larger number of bands in the RE spectra. This is because REs have much more energy levels available. This can be easily proven by equation 1.3. For transition metals N equals 10 where as for REs N equals 14. Therefore much more transitions are possible. In addition the spin orbit coupling also allows more transitions. Another difference of RE and transition metal spectra lies in their temperature dependence. Both show a broadening of bands as the temperature increases. The excitation spectra of RE, however, also show another phenomenon: The emergence of additional peaks. These are called "hot bands" and have their origin in energy levels that are close to the ground state. At higher temperatures these states are sufficiently populated and transitions from them can be observed. At lower temperatures they are scarcely populated and the hot bands vanish. Eu^{3+} and Nd^{3+} are two RE ions that show these hot bands at high temperatures. For the Eu^{3+} ion it is the ${}^7F_1$ state that is responsible for the emergence of hot bands. In Nd^{3+} however the next RS multiplet ${}^4I_{11/2}$ is too high above the ground state to be populated adequately even at high temperatures. Here the hot bands arise because of the CF splitting of the ${}^4I_{9/2}$ ground state.

1.2.2. Crystal Field (CF) - Theory and its Effect on Eu^{2+}

In the last section the crystal field operator was neglected because of the inner-shell nature of the 4f electrons. For some RE ions, however, the CF is crucial and cannot be neglected. Two of these ions are Ce^{3+} and Eu^{2+}. The second one plays the central role in this master thesis. This different behaviour is due to the unoccupied 5d orbitals which are highly sensitive to the CF as it can be seen in figure 1.3. If the CF is strong enough

the lower levels of the CF split 5d configuration is even lowered below the RS term that is usually responsible for the emission. Consequently transitions will take place from the 5d orbitals. Transitions that change from one to an other configuration (e.g. $4f^6 5d^1 \rightarrow 4f^7$) are called interconfiguration (IC) transitions. Because these transitions are much stronger than pure 4f transitions (they are not parity forbidden) they will dominate the spectrum. Therefore a brief introduction into the CF theory will be given to provide a better understanding of such spectra.

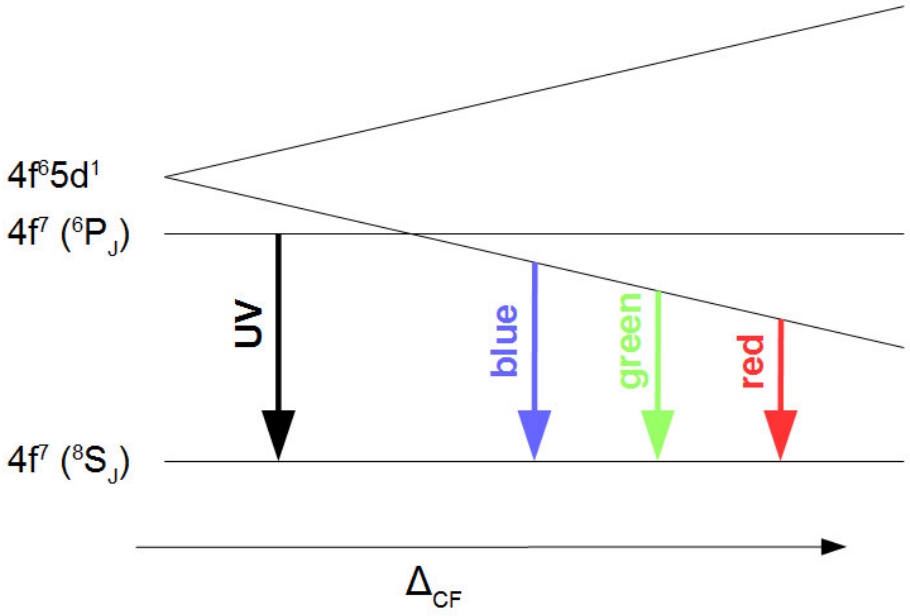

Figure 1.3.: Effect of CF to the energy levels of Eu^{2+}: when the CF is strong enough emissions inside the visible window are possible.

This discussion will only focus on the 5d electrons if not otherwise stated. It describes the unfavourable interactions of the ligands with the 5d electrons of the central atom. Both are negatively charged and hence repel each other. Because the ligands are not distributed spherically the perturbation is anisotropic. This leads to a splitting of energy levels which can be described with qualitative (number and nature) and quantitative (spacing) aspects.

The spacing is given by the strength of the CF. It depends on the coordination number (CN), the geometry of the coordination sphere and the nature of the ligands. The latter depends on the charge, the electronegativity and the electron distribution and density. The spectrochemical series arranges the ligands with increasing CF strength:

$$I^- < Br^- < S^{2-} < SCN^- < Cl^- < NO_3^- <$$
$$F^- < H_2O < NH_3 < NO_2^- < CN^- < CO$$

The number and nature of the generated energy levels depend on CN, the geometry of the coordination sphere and the number of electrons on the central ion but not on the ligands. Thus the energy depends on the spatial arrangement of the electrons in respect to the ligands. Configurations that allow an avoiding of the interactions will be more favourable than configurations where electrons and ligands are forced to face each other. The resulting energy levels can therefore be described by designations that represent the symmetry of the coordination polyhedron. Depending on the strength of the CF compared to the other perturbations (see Equation 1.4) there are two possibilities. If $\hat{H}_{CF}$ is regarded as weaker than $\hat{H}_C$ the already split RS terms are further fanned out. The corresponding designations are irreducible representations (irreps) of the corresponding point group. This is called the weak field approach. In the strong field approach, however, the CF is considered to be the most important contribution to the perturbation of the free ion. Here splitting occurs from the fully degenerate d configurations. The energy levels are strong field terms.

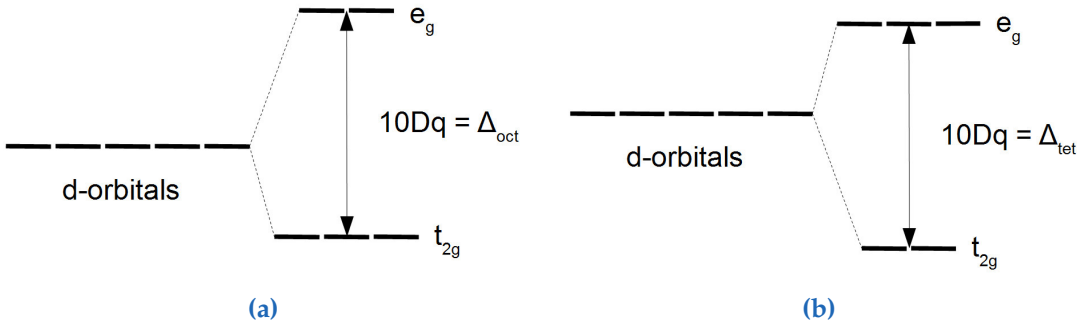

Figure 1.4.: CF splitting of an octahedral (a) and tetrahedral (b) coordination sphere. 10Dq is the historical designation for the magnitude of the splitting.

Figure 1.4a and 1.4b show the CF splitting of a tetrahedrally and an octahedrally coordinated d^1 configuration with its corresponding strong field terms. Historically the splitting is called 10Dq or Δ. It is larger in the octahedral coordination because of

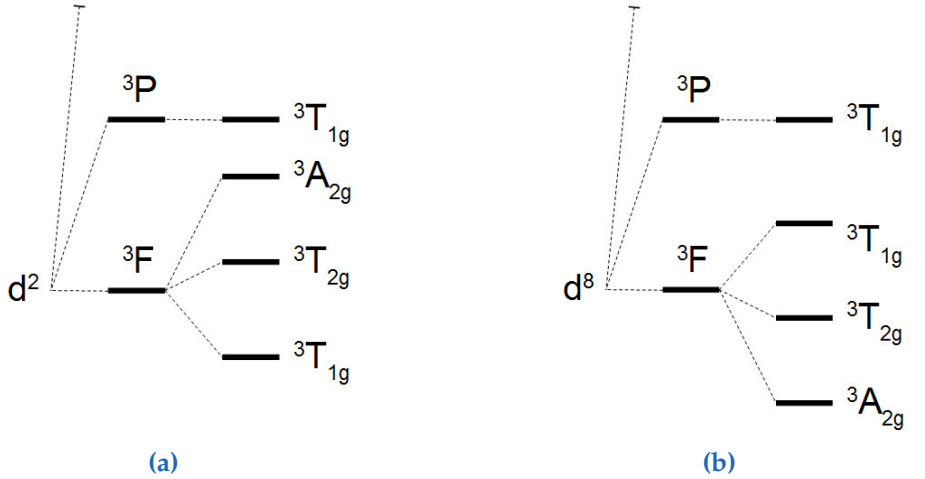

Figure 1.5.: CF splitting of the d^2 (a) and d^8 (b) configuration: notice that the order of irreps for the two configurations is inverted.

the higher CN and the shorter distances. The order of the irreps, however, obeys the electron-hole formalism. Consequently a d^9 configuration shows an inverted order of the irreps. This is shown in figure 1.5 for the weak field approximation of the d^2 and d^8 configuration.

1.2.3. Possible Mechanisms

As already mentioned $SrAl_2O_4$: Eu, RE (where RE denotes an additionally doped rare-earth ion, e.g. Dy) is a well investigated but still not fully understood persistent luminescent material. There are a great deal of theories that try to explain the observed afterglow. Their basic concepts are different but they are nearly all based on the existence of vacancies in the material. Hence a brief overview on the defects possible in an insulator is given but the focus is on the host material $SrAl_2O_4$.

One can distinguish between intrinsic and extrinsic defects. The former occur in pure but also in doped materials whereas the latter occur only in doped materials.

An intrinsic defect occurs when a particle is not where it should be. These defects are unavoidable because they increase the entropy and hence lower the Gibbs energy of the crystal. One common kind of defect is the Schottky defect. Here one anion and one

cation leave the crystal and generate a pair of vacancies.

$$Sr_{Sr} + O_O \longrightarrow V''_{Sr} + V^{\bullet\bullet}_O + SrO \tag{1.5}$$

Because of the charge balance the number of anion and cation vacancies must be stoichiometric. Another possibility for generating vacancies is by Frenkel defects. Here an ion leaves its crystallographic site and occupies an interstitial site leaving behind a vacancy at its original position.

$$O_O \longrightarrow O''_i + V^{\bullet\bullet}_O \tag{1.6}$$

This defect can be generated by just one sort of ions because no charges are removed from the crystal. The number of Schottky as well as Frenkel defects depend on temperature - both increase with temperature.

The extrinsic defects are produced by impurities (dopants). If the valance of the ion in the host material does not coincide with the valence of the dopant replacing this ion, defects must be generated because charge neutrality has to be guaranteed. The number of extrinsic defects hence depends on the concentration of the dopants.

In $SrAl_2O_4$ V_{Sr} but also V_O can be generated. These vacancies can be formed during the synthesis that is implemented at comparatively high temperatures. If Sr^{2+} is replaced by Dy^{3+} the charge balance must be maintained. This can be achieved by removing three Sr^{2+} and adding just two Dy^{3+}. The net result is that one V_{Sr} is generated.

$$3Sr_{Sr} + 2Dy^{3+} \longrightarrow 2Dy^{\bullet}_{Sr} + V''_{Sr} + 3Sr^{2+} \tag{1.7}$$

Oxygen can leave the crystal during a reducing treatment.

$$O_O \longrightarrow V^{\bullet\bullet}_O + 1/2O_2 + 2e^- \tag{1.8}$$

If the electrons remain in the host matrix no additional cation vacancies are formed.

The electrons can for example be taken up by an Eu^{3+} ions which are then reduced to Eu^{2+}.

$$2Eu_{Sr}^{\bullet} + 2e^{-} \longrightarrow 2Eu_{Sr} \tag{1.9}$$

Energetically all these vacancies are located in between the valence band (VB) and the conduction band (CB) of the host material.

For the mechanisms that will be discussed below both effects are important.

One of the first models that attempted to explain the afterglow of co-doped $SrAl_2O_4$:Eu^{2+},Dy^{3+} was suggested by Matsuzawa et al. in 1996 [10]. The model is shown in figure 1.6.

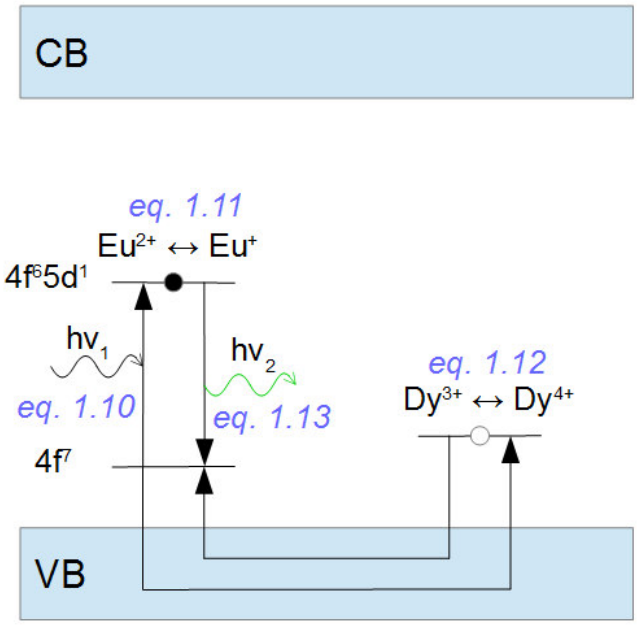

Figure 1.6.: Mechanism proposed by Matsuzawa.

In this paper Abbruscato's hypothesis that holes are the charge carriers and therefore responsible for the afterglow process was confirmed [21]. This assumption was supported by photocurrent measurements. It was claimed that the $4f^7$ state of Eu^{2+} is near the valence band (0.06 eV). After UV light is irradiated Eu^{2+} is excited to the $4f^65d^1$ state.

$$Eu_{Sr} + h\nu_1 \longrightarrow (Eu_{Sr})^{*} \tag{1.10}$$

In addition the $4f^7$ state releases a hole to the VB and reduces therefore Eu^{2+} to Eu^{+}.

$$(Eu_{Sr})^* \longleftrightarrow (Eu'_{Sr})^* + h^+ \tag{1.11}$$

The hole migrates to a Dy^{3+} site which is about 0.65 eV above the VB. The hole is trapped and Dy^{3+} is oxidized to Dy^{4+}.

$$h^+ + Dy^{\bullet}_{Sr} \longleftrightarrow Dy^{\bullet\bullet}_{Sr} \tag{1.12}$$

After a certain time the hole is again thermally released to the VB and migrates to the Eu site (reverse to equation 1.12). It recombines with the $4f^7$ (reverse to equation 1.11) state which causes the luminescence.

$$(Eu_{Sr})^* \longrightarrow Eu_{Sr} + h\nu_2 \tag{1.13}$$

Eu and Dy are again in their initial oxidation states 2+ and 3+. This mechanism was criticized because of several reasons. First because it involves unlikely oxidation states. Eu^{+} and Dy^{4+} are believed to be not stable in $SrAl_2O_4$. Second it was argued that this model is based on a wrong concept of a hole state. And third the photocurrent measurements were also questioned. Thus also electrons can be possible charge carriers in this material.

Another mechanism was proposed by Aitasalo et al. in 2003 (see figure 1.7) [22].

It was developed for a $CaAl_2O_4$ matrix but should also apply for $SrAl_2O_4$ because of the same crystal structure. Here it is assumed that electrons of the VB are excited by UV light into vacancies of unknown origin leaving behind holes in the VB. These holes migrate in the VB and are finally captured by a V_{Sr}. The electron is eventually trapped in a V_O.

$$SrAl_2O_4 + h\nu \longrightarrow e^- + h^- \xrightarrow{V^{\bullet\bullet}_O} \xrightarrow{V''_{Sr}} V^{\bullet}_O + V'_{Sr} \tag{1.14}$$

If these vacancies are close together recombination can take place. There is energy

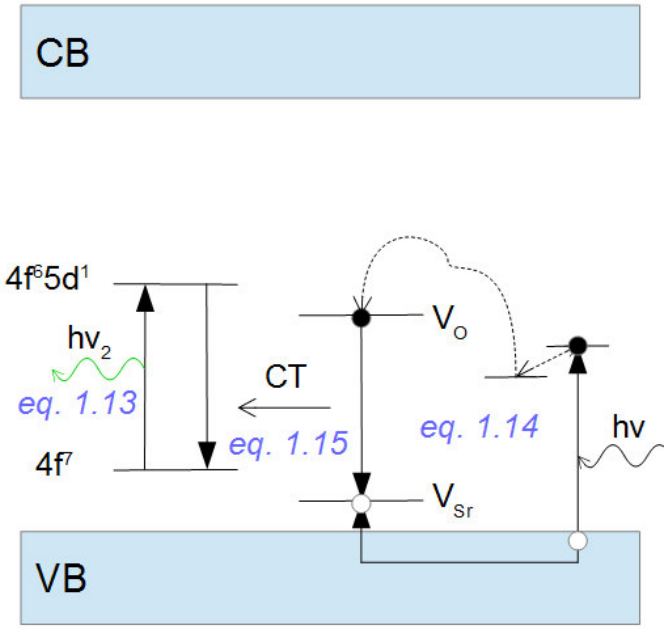

Figure 1.7.: Mechanism proposed by Aitasalo.

released which can be absorbed by an Eu^{2+} if it is in the vicinity of the recombination centre. Hence Eu^{2+} is excited into the $4f^65d^1$ state.

$$V_O^{\bullet} + V_{Sr}' + Eu_{Sr} \xrightarrow{CT} (Eu_{Sr})^* + V_O^{\bullet\bullet} + V_{Sr}'' \tag{1.15}$$

Eu^{2+} relaxes again and emits a photon (equation 1.13).

A similar process was suggested by Beauger in 1999 [23]. He claimed that the electron is not trapped in an V_O. It directly recombines from the above mentioned vacancies of unknown origin to the VB. The central role of both models, however, is the energy transfer that requires the recombination centre to be close to the Eu site. Up to now no other co-dopants are involved. Thus it does not explain the different impacts of the RE ions to the duration of afterglow. Aitasalo et al. explained this by the formation of defects. Co-dopands like Dy^{3+} and Nd^{3+} that cause a long afterglow generate additional extrinsic defects to enable charge balance. They are only stable in their trivalent state. However, ions like Sm and Yb are also stable divalent ions. Therefore no additional V_{Sr} needs to be formed. This decreases the probability of recombination centres being near to the Eu sites. In this process neither Eu nor the co-dopants change

their oxidation state.

Clabau et al., however, showed with Electron Paramagnetic Resonance measurements (EPR) that the Eu^{2+} concentration decreases during excitation [24]. Hence they suggested a new mechanism in 2005 (see figure 1.8) [24, 25].

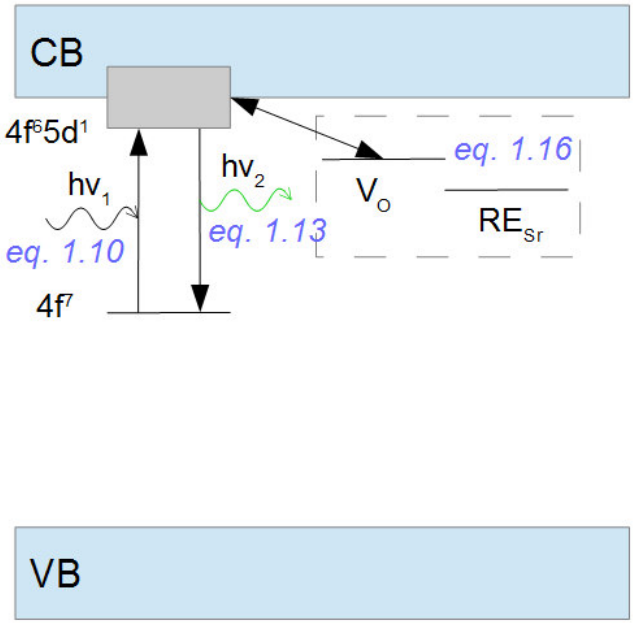

Figure 1.8.: Mechanism proposed by Clabau.

Many results of this work were derived from thermoluminescence measurements (TL). First Eu^{2+} is excited by UV light (equation 1.10). Then the electron is directly captured by a V_O and does not migrate in the CB.

$$(Eu_{Sr})^* + [V_O^{\bullet\bullet}][RE_{Sr}^{\bullet}] \longleftrightarrow Eu_{Sr}^{\bullet} + [V_O^{\bullet}][RE_{Sr}^{\bullet}] \tag{1.16}$$

This vacancies are stabilized by the co-doped RE. The RE shift electron density to the V_O. The lower the ionisation potential of the RE the higher the stabilization of the vacancy is. Therefore there are differences between the REs referring to their ability to promote the afterglow. When the electron is released it enables the $4f^6 5d^1 \rightarrow 4f^7$ transition.

Dorenbos published his mechanism in 2005 (see figure 1.9) [26].

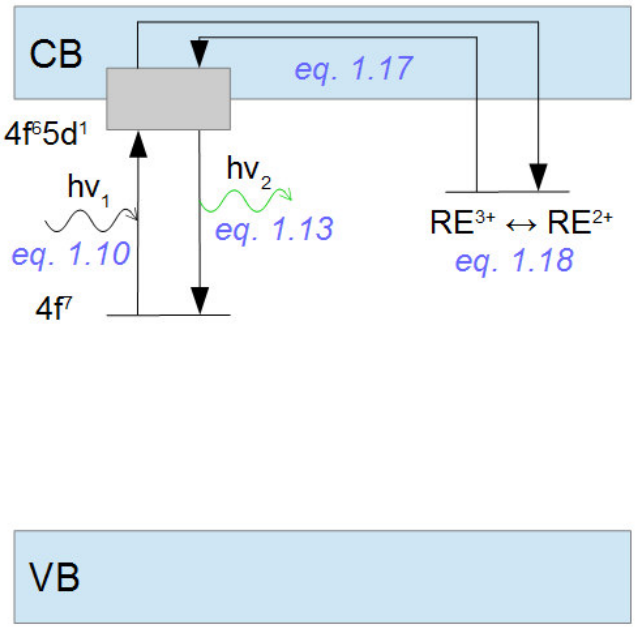

Figure 1.9.: Mechanism proposed by Dorenbos.

In this model Eu^{2+} is excited by UV light (equation 1.10). The electron is then released into the CB.

$$(Eu_{Sr})^* \longleftrightarrow Eu^{\bullet}_{Sr} + e^- \tag{1.17}$$

The electron migrates to a RE site where it is trapped.

$$e^- + RE^{\bullet}_{Sr} \longleftrightarrow RE_{Sr} \tag{1.18}$$

Here it remains until it is eventually thermally released. It returns back to Eu and produces the luminescence (equation 1.13). In this mechanism the depth of the traps is crucial. They were determined for all REs by Dorenbos. Traps that are too shallow or too deep and do not support a long afterglow. They are either too easy or too difficult to vacate at ambient temperatures. Traps that are about 1 eV below the CB, however, support the persistent luminescence. This is the case for Nd, Dy, Er and Ho. In this model the co-dopants are reduced.

In 2006 Aitasalo et al. formulated a new mechanism that combines the models of Clabau et al. and Dorenbos (see figure 1.10) [27].

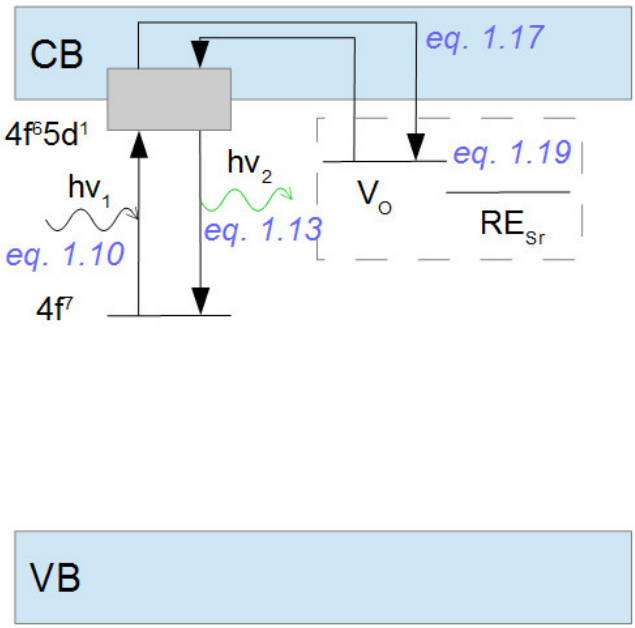

Figure 1.10.: New mechanism proposed by Aitasalo.

These studies are based on TL. Eu^{2+} is excited and releases an electron to the CB (equation 1.17). The electron is then captured by an V_O and passed on to other vacancies till it reaches the RE site.

$$e^- + [V_O^{\bullet\bullet}][RE_{Sr}^{\bullet}] \longleftrightarrow [V_O^{\bullet}][RE_{Sr}^{\bullet}] \tag{1.19}$$

It is claimed that the trap depth of the RE is not important for promoting the afterglow. It is more the different reduction potential and the ionic radius that decide whether the electrons are more or less easily released by the REs. Moreover it is assumed that the trivalent RE form RE^{3+}-e^- pairs. Hence they are not reduced. The only exceptions are Sm^{3+} and Yb^{3+} because they are stable in the divalent state. The main differences to Clabau's mechanism are the migration of the electron through the CB and a possible reduction of the RE. Furthermore he claimed that the ionisation potential and the ionic radius but not the ionisation potential is crucial.

In 2009/10, however, this was questioned by Hölsä et al. using X-ray absorption near edge finestructure measurements (XANES) [28, 29]. It was found that the oxidation state of REs does not change during excitation. Hence there are only formed RE^{3+}-e^-

pairs.

Furthermore it was found out by thermostimulated luminescence (TSL) that the trap depth of co-doped and not co-doped $SrAl_2O_4$ is the same [30]. Hence the trap must origin from a site that also exists in the not co-doped material.

1.3. Overview and Objectives

In the frame of this master work several samples of doped and co-doped $SrAl_2O_4$ were prepared by the solution combustion method followed by a sintering step under reducing atmosphere. The aim was to find a material where the afterglow period is maximised and to investigate the influence of the co-dopants and temperature on its optical properties. In this way it was hoped to obtain clues about the dominating mechanism leading to the long lasting phosphorescence .

This section gives a detailed overview over the project and shows which steps were taken and what information can be obtained from them. It concludes with a table of short-cut names for the samples that are used in the next chapters to provide a convenient designation for the samples.

First of all $SrAl_2O_4$ was synthesised via solution combustion. One preparation was followed by a single sintering step another one by a twofold sintering step. After that the samples were measured by XRD to figure out how many sintering steps are needed to yield samples with adequate crystallinity. In addition the XRD gave information about the crystal structure including data of the environment of the two Sr sites. This is important because in the doped material the rare-earth ions replace Sr ions.

Next, doped $SrAl_2O_4$ samples were synthesised. The used dopants were Eu^{2+}, Eu^{3+}, Dy^{3+}, Nd^{3+}, Pr^{3+} and Sm^{3+}. The samples were prepared via solution combustion followed by a sintering step under reducing atmosphere to enable and promote the formation of Eu^{2+}. The Eu^{3+} doped sample, however, was prepared under oxidizing conditions. The optical characterisation was carried out by a fluorescence spectrometer. This was done to find out their oxidation state and their optical characteristics. This was useful because the co-doped systems in principle can show a high number of bands of different origin.

After that co-doped $SrAl_2O_4$: Eu, Dy (x,x) samples were prepared. They were syn-

thesised and measured analogously to the singly doped samples. This was done to figure out which Eu-RE ratio is the best to show persistent luminescence for as long as possible.

Finally, $SrAl_2O_4$: Eu, RE samples were synthesised. Here RE stands for Nd, Pr and Sm. Together with the corresponding co-doped Dy sample they were optically characterized at different temperatures. The results of these experiments could give information about the influence of the co-dopant and the temperature.

All these steps and their resulting conclusions are shown in a flow chart (figure 1.11) to give a vivid overview over the work that was done in the course of this diploma thesis.

In addition some experiments with $NdAl_2O_4$, Eu_2O_4 and $Eu(NO_3)_3$ were performed. The results can be found in the appendix.

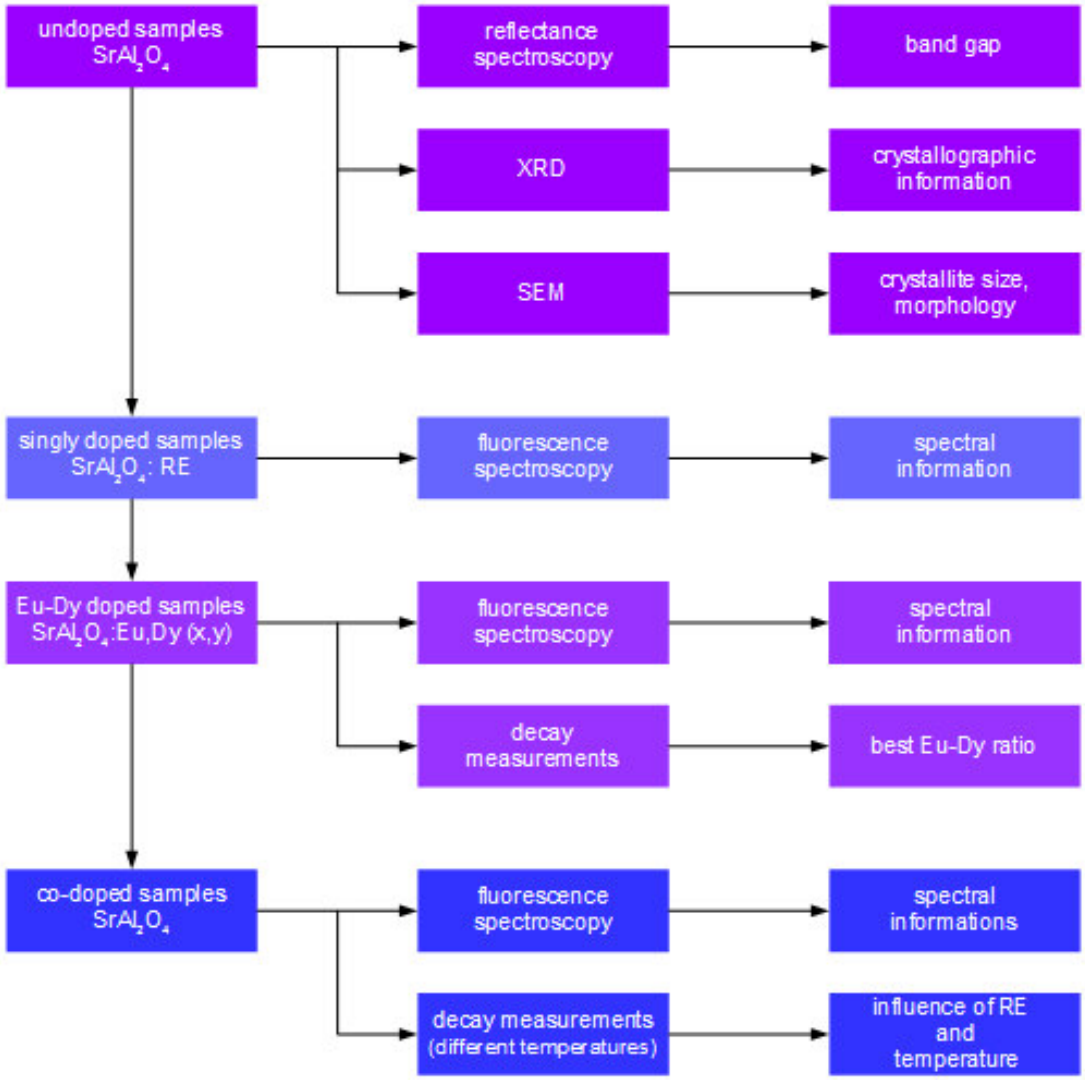

Figure 1.11.: Flow chart of the master thesis' work: the left column gives information about the constitution of the samples, the middle column tells about the used technique of measurement and the right column reveal the results that were hoped to be received from the measurements.

2. Used Equipment, Chemicals and Methods

2.1. Instruments and Equipment

All instruments and equipment used in this master thesis can be found in table 2.1.

Table 2.1.: Instruments and equipment used in this master thesis.

Application	Equipment
fluorescence spectroscopy	*PerkinElmer LS-55*
reflectance spectroscopy	*PerkinElmer Lambda 950*
XRD	*Bruker D8 Advance*
SEM	*Zeiss Ultra 55*
SC and sintering	*Nabertherm L3/S27* muffle furnace
sintering	*Gero SR 70-500/12* tube furnace

The set up of the tube furnace was modified in order to provide a closed system when samples were to be prepared under reducing conditions. A long quartz tube with two vents was inserted into the furnace. The vents were linked with the gas bottle and an overpressure unit by hoses, respectively. The overpressure unit consisted of a bubbler filled with silicone oil and a safety valve and was placed in a fume hood.

2.2. Chemicals

All chemicals used for the synthesises are listed in table 2.2. There were used two different products of $Al(NO_3)_3 \cdot 9H_2O$. Only the undoped samples were prepared by

the first product (marked with an (*) in the table).

Table 2.2.: The chemicals used for the preparations.

Substance	M_r [g/mol]	Manufacturer
$Sr(NO_3)_2$	211.63	*Merck & Co.*
$Al(NO_3)_3 \cdot 9\,H_2O$*	375.13	*Merck & Co.*
$Al(NO_3)_3 \cdot 9\,H_2O$	375.13	*Carl Roth*
Urea (CH_4N_2O)	60.06	*LobaChemie*
Eu_2O_3	351.93	*Treibacher Chemische Werke AG*
Dy_2O_3	373.00	*Sigma-Aldrich*
Nd_2O_3	336.48	*Treibacher Chemische Werke AG*
Pr_5O_{11}	880.54	*Fluka Chemie AG*
$Sm(NO_3)_3 \cdot 6\,H_2O$	336.38	self-produced
HNO_3 (53%)	63.01	*Fluka Chemie AG*

2.3. Solution Combustion

A conventional method for synthesizing materials doped with REs is the solid state method in which oxides of the starting materials are ground, well mixed and then sintered. It requires temperatures over 1000°C because of the mainly refractory nature of the host materials. It is a diffusion controlled reaction and therefore needs repeated grinding and heating. Also the atmosphere needs to be controlled to avoid unwanted redox reactions. The solid state reaction has some limitations. The doping with low concentrations is difficult to handle. Furthermore the obtained product has usually low homogeneity and large particle sizes. Hence post treatments are necessary that can lead to contamination.

These problems can be avoided by using wet-chemical methods. The obtained product is homogeneous. However, they usually need a calcination step because of low crystallinity.

An exception is the solution combustion method (SC) that does not need any fur-

ther treatment [31]. It was accidentally discovered in an Indian laboratory. The big advantages are the low synthesis temperatures (600°C) and very short preparation times of approximately five minutes. The idea is to mix fuel and oxidizer in an aqueous solution, put it into a furnace at comparatively low temperatures and let it react. Metal nitrates are used as oxidizer. Compounds that do not consist of nitrates need to be transformed by a pre-treatment. The fuel is usually a hydrazine based compound. Urea and glycine are examples. The oxidant to fuel ratio (O/F) is crucial. According to propellant chemistry the best combustion process is achieved by an O/F of one. In this concept metals, carbon, hydrogen and boron have a valency according to their oxidation state in the oxides. Oxygen has a valency of -2. Nitrogen is taken to have a valency of 0 because it is assumed that the whole nitrogen leaves the reaction as N_2. However, in practice also NO_x is formed. Some compounds including their valencies are entered in table 2.3. For instance using $Si(NO_3)_4$ as oxidant and carbohydrazide as fuel would require a stoichiometric ratio of 1 : 2.5.

Table 2.3.: Some oxidisers and fuels with their valencies.

Compound	valency
MNO_3	-5
$M(NO_3)_2$	-10
$M(NO_3)_3$	-15
$M(NO_3)_4$	-20
Carbohydrazide ($CH_6N_4O_2$)	$+8$
Glycine ($C_2H_5NO_2$)	$+9$
Urea (CH_4N_2O)	$+6$

The combustion is a highly exothermic process and self-propagating. Once ignited it does not need to be heated anymore. The process of SC is as follows. The solution boils, followed by a considerable formation of gases. Eventually the combustion starts and a highly porous foam is formed.

All samples in these master thesis were prepared by SC.

3. Experimental Part

3.1. Sample Preparation

As was mentioned in chapter 1.3 it was decided to prepare undoped $SrAl_2O_4$ and three series of samples of doped material (SA,RE; SA,Eu,Dy(x,y); SA,Eu,RE). In table 3.1 all samples of the different series are listed. Because all samples were prepared more or less analogously the details will be only described once using the undoped $SrAl_2O_4$ as an example. Possible deviations from this method of preparation will be mentioned in the text.

It was decided to prepare about 2 g of undoped $SrAl_2O_4$ by solution combustion. Before preparation the quantities of the reactants had to be determined. The oxidisers were $Sr(NO_3)_2$ and $Al(NO_3)_3 \cdot 9H_2O$. Urea (CH_4N_2O) was used as the fuel. As mentioned in section 2.3 the ideal O/F ratio is 1. The reaction of the chemicals with their corresponding O/F-valency can be formulated with following theoretical reaction equation

$$Sr(NO_3)_2 + 2Al(NO_3)_3 + xCH_4N_2O \longrightarrow SrAl_2O_4 + (4+x)N_2 + 2xH_2 \tag{3.1}$$

Here x is the unknown to be determined. Because the sum of valencies of oxidants and fuel needs to be 0 equation 3.1 can be interpreted as

$$1(-10) + 2(-15) + x(6) = 0$$

Here the chemical formulas of the substances were substituted by the O/F valencies (see table 2.3). Hence x equals $6.\overline{6}$ (= 20/3). Now all stoichiometric coefficients necessary to calculate the masses for the reaction are known. For this purpose the amount of

Table 3.1.: The sample series and their samples.

sample series	samples
$SrAl_2O_4$	SA(untr.); SA(1xsint); SA(2xsint)
$SrAl_2O_4$: RE (x%)	SA,Eu^{2+}(1); SA,Eu^{3+}(1); SA,Dy(1);
	SA,Nd(10); SA,Pr(1); SA,Sm(1)
$SrAl_2O_4$: Eu, Dy (x%;y%)	SA,Eu,Dy(0.5;0.25); SA,Eu,Dy(0.5;0.5);
	SA,Eu,Dy(0.5;1); SA,Eu,Dy(1;0.5);
	SA,Eu,Dy(1;1); SA,Eu,Dy(1;2)
$SrAl_2O_4$: Eu, RE (x%;y%)	SA,Eu,Dy(1;1); SA,Eu,Nd(1;1);
	SA,Eu,Pr(1;1); SA,Eu,Sm(1;1)

substance n was taken as the hundredth of the stoichiometric coefficients (meaning 0.01 mol for $Sr(NO_3)_2$; 0.02 mol for $Al(NO_3)_3 \cdot 9H_2O$ and $0.0\overline{6}$ mol for urea).

$Sr(NO_3)_2$, $Al(NO_3)_3 \cdot 9H_2O$ and urea, all colourless powders, were weighted into a beaker. 3 ml distilled water were added by a pipette. The mixture turned into a colourless slurry. The beaker was put on a magnetic stirrer and was covered with a watch glass as lid to avoid excessive water loss. The slurry was stirred vigorously at approximately 75°C [18]. In the beginning the preparation showed a clear aqueous phase with a colourless precipitate. Later the aqueous phase turned murky and less precipitate was observed. Early experiments showed that the suspension will stay in this state even for long stirring times (3.5 hours). Therefore 1.5 hours of stirring were regarded as adequate. After the stirrer was removed the beaker together with the lid was put into a 600°C pre-heated *Nabertherm L3/S27* muffle furnace. The temperature was chosen in agreement with the literature [17]. The vent was left open to allow the formed gases to escape. The door was kept closed during the whole reaction. However, the process in the oven was filmed in a test phase to reveal the single steps of the reaction. Some selected stages are shown in Fig. 3.1. The suspension starts to boil followed by the formation of colourless gas (3.1a). After the majority of the liquid is gone (3.1b) the combustion reaction starts with a bright flash. The mixture is burning and the formation of gases is increasing tremendously (3.1c). It has a slightly brown

colour showing that also NO_x is generated. Then the product is formed and parts of it are thrown out of the beaker (3.1d). The whole process takes about five to ten minutes. After the reaction the beaker was left in the furnace to cool down under 300°C. This was done to avoid a too comprehensive contact with the comparatively cool surrounding.

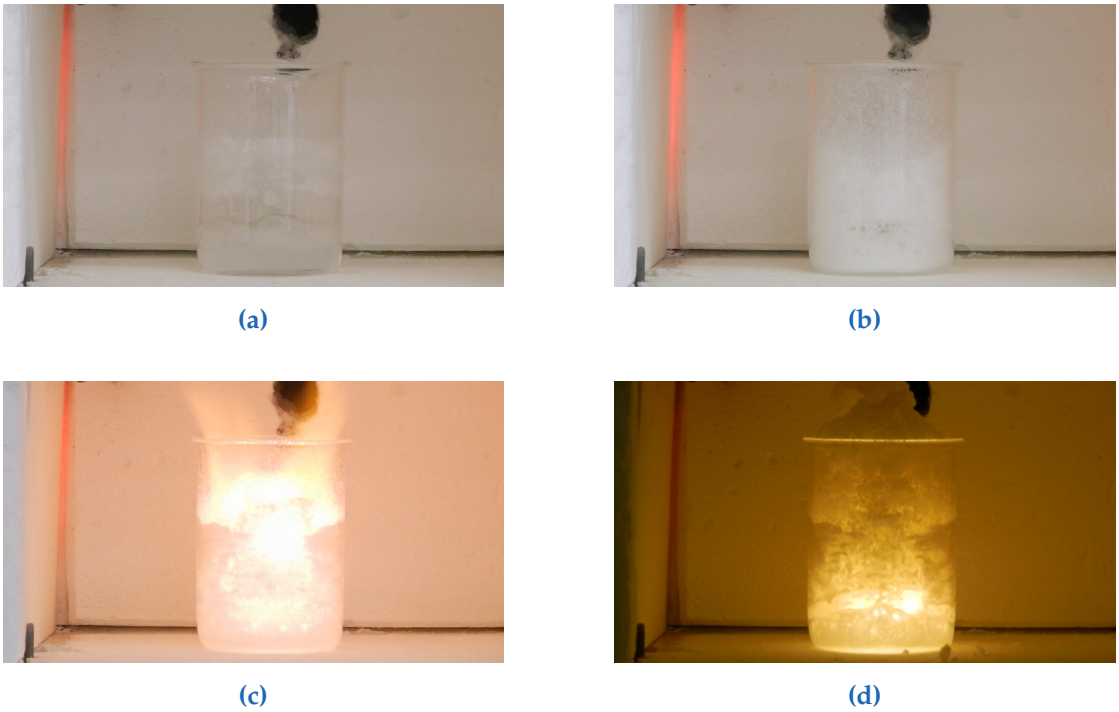

(a) **(b)**

(c) **(d)**

Figure 3.1.: The stages of solution combustion: The initially clear solution is boiling (a) and turns murky after about 5 minutes (b). Then it ignites and starts to burn (c). Eventually the product is formed (d).

The product itself is a colourless foam with high porosity. It shows many pores on the surface and hollow formations. It is extremely brittle and easy to squash. Figure 3.2 shows the product in the beaker. The foam was crushed and ground with a spatula. The obtained powder was filled into a sample vial (sample SA(untr.)).

Afterwards it was decided to sinter two parts of the sample once and twice, respectively (samples SA(1xsint); SA(2xsint)). For the sintering procedure the powders were pressed into cylindrical pills. The pressure was increased in 0.5 t steps followed by one to two minutes of relaxation until the end pressure of 2.5 t was reached. The pills were laid into Pt crucibles which were put into the 1100°C pre-heated muffle furnace. The dwell time was two hours. Before the samples were removed from the furnace they

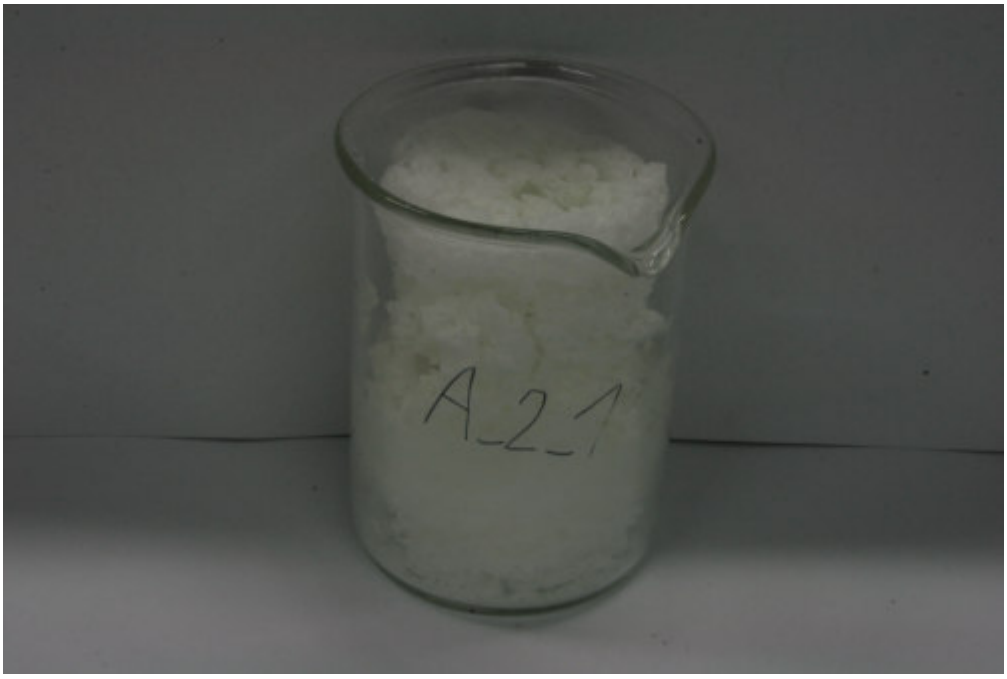

Figure 3.2.: A preparation synthesized by solution combustion.

were cooled down under 600°C. Afterwards the pills were thoroughly ground with an agate mortar. As was expected the samples did not show any fluorescence under an UV lamp.

For the (co-)doped samples it was also decided to synthesize about 2 g. The used chemicals were Eu_2O_3, Dy_2O_3, Nd_2O_3, Pr_6O_{11} and $Sm(NO_3)_3 \cdot 6H_2O$. The latter can be used directly. All other reactants need a pre-treatment to convert them into nitrates. For this purpose they were mixed with a certain amount of 53% HNO_3. The required quantity of nitric acid was determined by the reaction equation. For the RE in the oxidation state of 3+ it can be written as:

$$RE_2O_3 + 6HNO_3 \longrightarrow 2RE(NO_3)_3 + 3H_2O \tag{3.2}$$

With 63.01 g/mol as $M_r(HNO_3)$, 0.06 mol as n (consider: one hundredth of the stoichiometric coefficient) and 53% as mass fraction w the needed mass can be determined. For Pr it was first calculated an average oxidation state because of its two possible states 3+ and 4+ in the oxide. This pseudo oxidation state was set to $3.\overline{6}+$ (= 11/3). The

reaction equation can be written as

$$RE_6O_{11} + 22HNO_3 \longrightarrow 6RE(NO_3)_3 + 11H_2O \tag{3.3}$$

Again m(HNO_3) can be easily determined. For the determination of m(urea) for the trivalent REs equation 3.1 can be modified.

$$(1-\alpha)Sr(NO_3)_2 + 2Al(NO_3)_3 \cdot 9H_2O + \alpha RE(NO_3)_3 + xCH_4N_2O \longrightarrow$$

$$SrAl_2O_4 : RE(0.01\alpha\%) + (4+x)N_2 + 2xH_2 + 18H_2O \tag{3.4}$$

It can be easily seen that the sum of the coefficients for $Sr(NO_3)_2$ and $RE(NO_3)_3$ is equal to 1. Hence there is no excess needed and $SrAl_2O_4$: RE is formed without any other solid by-products. However, this is not exact because of the different oxidation states of Sr and RE. Therefore a product should actually be positively charged or have a large mole fraction of oxygen. This mathematical problem of writing an exact substance formula can be hurdled by an approximation. For small values of α, or more precisely for small doping quantities, the contribution of $RE(NO_3)_3$ can be neglected. Consequently the already determined mass for the undoped $SrAl_2O_4$ preparation can be taken. Everything is analogous for Pr and co-doping. After the determination of the masses the sample preparation can be started.

First the desired RE oxides was weighted into a beaker. The stoichiometric amount of 53% HNO_3 was added by a glass Pasteur pipette. The solids and acid were dispersed and mixed by a spatula. The mixture started foaming and a pungent odour was perceptible. Then the reactants for the host material, urea and water were added. For $Sm(NO_3)_3 \cdot 6H_2O$ of course, no nitric acid is needed and all reactants can be mixed directly. The remaining steps for the preparation of the unsintered product proceeded along the same line as the undoped $SrAl_2O_4$. The foam was ground with an gate mortar and filled into a sample vial. All samples were placed under an UV lamp operating with the two wave lengths 365 nm and 254 nm. All of them showed a luminescence

that is characteristic for their composition. Some co-doped samples already showed an afterglow. All details will be discussed in chapter 4.

After that the samples were sintered under reducing atmosphere. The modified set up of the *GERO SR 70-500/12* tube furnace and the external *Eurotherm* temperature control unit was used. The reducing agent was forming gas (10% H_2, 90% N_2). Of each sample about three to four spatula tips were given into an Al_2O_3 boat and were dispersed on the boat's bottom. Then they were charged into the quartz tube. The tube was sealed off and inserted into the furnace. The tube was evacuated and purged with the forming gas. This was repeated three times. The flow velocity was adjusted in a manner that in every second a gas bubble emerged in the bubbler. The temperature program started with a ramp (about 15 minutes) and a dwell time of two hours at a temperature of 1100°C. After the program finished the quartz tube was pulled out of the furnace and cooled down for one to two hours. Then the tube was opened and the powders were put back into the vials. Again the samples were investigated with an UV lamp. For detailed observations see chapter 4.

3.2. Optical Measurements

The optical characterization was performed with the *PerkinElmer(R) LS-55* Fluorescence Spectrometer. The sample holder was charged with three to four spatula tips of the powder. The instrument settings for recording the spectra was not uniform. The settings will be given in a small table after each spectrum. Four types of measurements were made: Excitation/emission spectra at ambient temperatures, excitation/emission spectra at deep/high temperatures, emission spectra for the decay curves at ambient temperatures and emission spectra for the decay curves at deep/high temperatures.

For the first type of measurement no additional modification of the instrument was needed.

For the second, however, the configuration of the spectrometer needed to be changed. The sample holder was connected with a Peltier element. Because the device was too big the cover of the sample compartment had to be left open during the measurements. To avoid artefacts caused by surrounding light and loses of the cooling/heating power the sample holder and sample house was wrapped and covered with black foam and

cloths. Test measurements showed that the obtained spectra were not affected by the environment. With the Peltier element the temperatures were set to $-10°C$ and $+60°C$.

The third type of measurements required the use of a stop watch because the instrument is not equipped for measuring long-time decay curves. The samples were put into the instrument and illuminated for about three minutes. Then the light source was turned off (t_0) and the start of the first measurement was stopped with the watch (t_1). After the first measurement was finished the next scan was started manually. This was done in 30 minutes intervals until a delay of five minutes was reached. Then two more measurements at the decay time of 10 and 15 minutes were done. A more precise way to monitor the long-time decay with this instrument was not possible because the delay setting in the phosphorescence mode is limited to a few ms. Therefore the measurements for long afterglows needs to be made manually. However, the even more unpleasant problem was that the measurement did not start immediately after the light source was switched off. When the start bottom was pressed the illumination stopped immediately but the measurement started only some seconds later. The smallest possible time for t_1 was approximately 6 s. Therefore there were recorded a decay curve for a short time range and for a long time range respectively. The short time range included measurements from 0 ms to about 10 ms. The long time range lasted from approximately 5 s to 15 minutes. Hence recording of decay curves that covers the whole time range of the fluorescence was not possible. In addition it was not possible to compare the intensities of both time ranges, because the measurement conditions were different. The settings for the short time range were a small slit size and a low voltage for the detector. Higher values would have led to a signal overflow. However, a wide slit and a high detector gain were necessary for the long time range. Otherwise the bands would have disappeared in the background. The difference in intensity was therefore a factor of about $10,000$. Nevertheless the afterglow could be well observed with the naked eye and analysis of the decay curves led to meaningful results. More details will be given in section 4. All measured emission spectra ranged from 400 to 700 nm. Hence only the $4f^6 5d^1 \rightarrow 4f^7$ transition was monitored.

The fourth type of measurement was a combination of the third and the second.

Some of the measurement conditions were the same for all measurements. They are given in table 3.2. All other parameters will be given in an additional table under the corresponding figure of the spectrum.

Table 3.2.: The measurement condition that stayed constant for all measurements.

Recording mode:	phos.	Gate time:	1 ms
Cycle time:	20 ms	Flash time:	1 ms
Scan speed:	1500 nm/min	Ex. slit:	10 nm

3.3. Scanning Electron Microscopy

The samples SA(untr.), SA(1xsint) and SA(2xsint) were mixed with a caldofix2 epoxy and embedded into a cast. The epoxy was hardened in a drying cabinet for two hours at a temperature of 50°C. This step was repeated after the cast had been replenished with epoxy. After that the samples were ground with SiC and polished with a diamond paste. Finally the samples were polished with a 40 nm silica gel. In the next step the samples were vaporized with carbon. During the measurements with the *Zeiss Ultra 55* it emerged that the sample preparation for SA(untr.) was unsatisfying. The powder was too much agglomerated which hampered an investigation with the electron microscope. Hence the sample was prepared again. It was diluted in water and then dispersed with ultrasonic. However, the powder still was too much agglomerated. Therefore the sample was prepared again in three different ways. One part of the sample was diluted in water and then dispersed with ultrasonic. Then it was pipetted onto a specimen holder of aluminium. Another part of the sample was prepared simultaneously with ethanol. The third preparation consisted of a direct coating of the powder onto the holder.

3.4. X-ray Diffraction

The samples SA(untr.), SA(1xsint) and SA(2xsint) were investigated with a *Bruker D8 Advance* XRD diffraction instrument. The samples did not need further treatment

because the powder was fine enough. All measurement conditions can be found in table 3.3.

Table 3.3.: Measurement conditions of the XRD.

Start position [2θ]	10
End position [2θ]	89
Step size [2θ]	0.02
Scan step time [s]	286.5
Offset [2θ]	0
Divergence slit type	fixed
Divergence slit size [°]	9999
Specimen length [mm]	10
Received slit size [mm]	0.1
Measurement temperature [°C]	25
Anode material	Cu
K-$\alpha 1$ [$\AA$]	1.54060
K-$\alpha 2$ [$\AA$]	1.54443
K-β [$\AA$]	1.39225
$K-\alpha 2/K-\alpha 1$ ratio	0.5
Generator settings	40 mA, 40 kV
Diffractometer type	θ/θ

4. Results and Discussion

4.1. The Host Material

4.1.1. Crystallographic Characterisation

The XRD spectra for the samples SA(untr), SA(1xsint) and SA(2xsint) are shown in figures 4.1, 4.2 and 4.3.

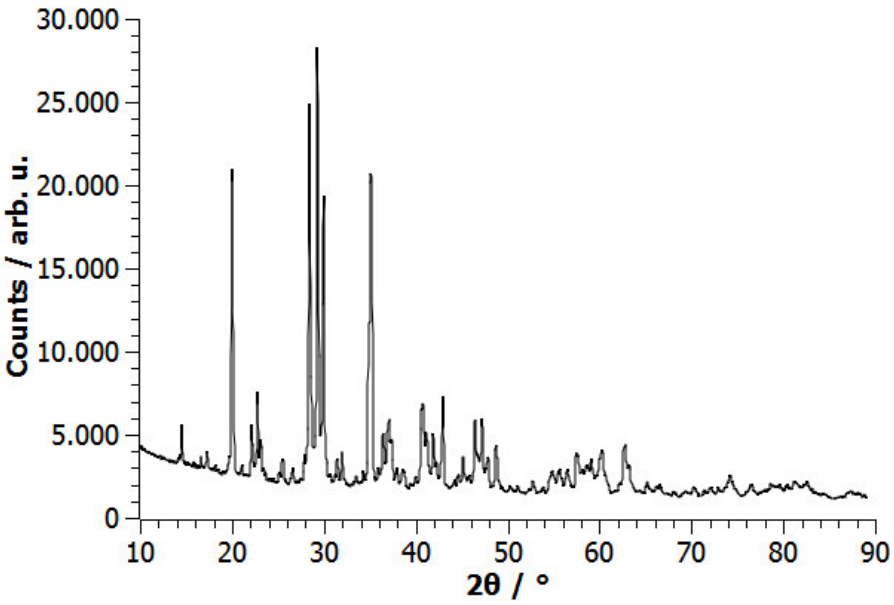

Figure 4.1.: XRD spectrum of sample SA(unt.).

Start	10°θ	End	89.00°θ	Step size	0.02°θ
Receiving slit	0.1 mm	Anode	Cu	K-α1	1.5406 $\AA$

The spectrum of SA(untr.) reveals different phases. The vast majority, about 92% corresponds to the desired $SrAl_2O_4$ α-phase that has a monoclinic crystal lattice. The

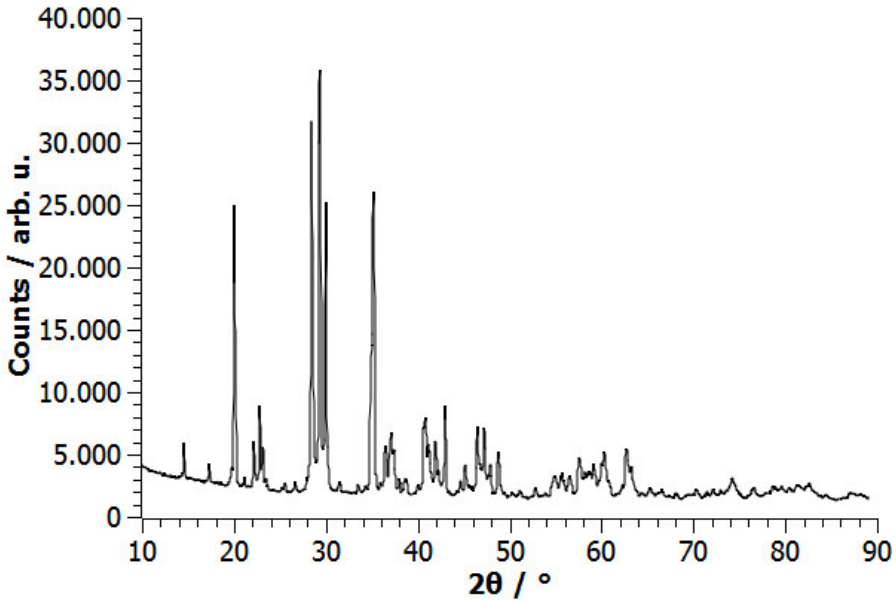

Figure 4.2.: XRD spectrum of sample SA(1xsint).

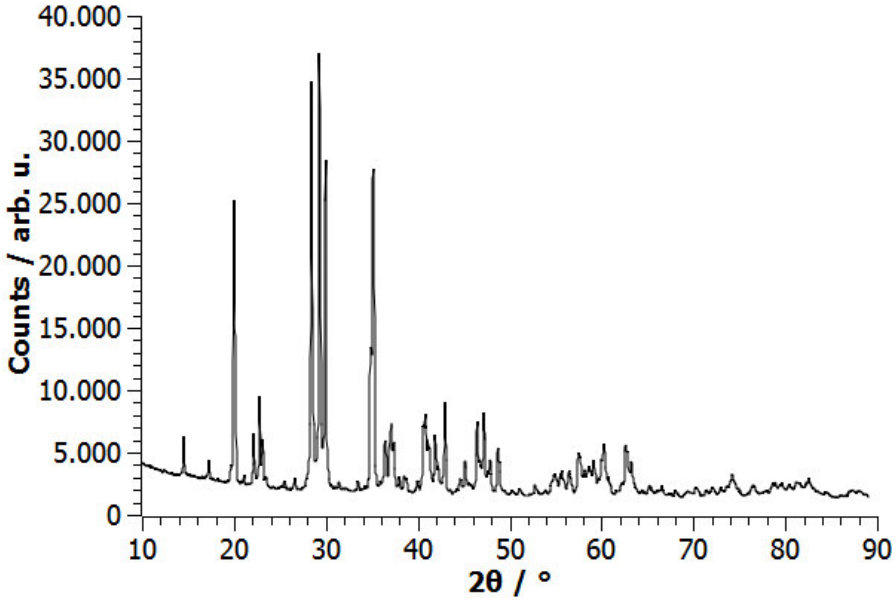

Figure 4.3.: XRD spectrum of sample SA(2xsint).

remaining phases belong to other $Sr_xAl_yO_z$ species (e.g. $Sr_3Al_2O_6$ or $Sr_4Al_{14}O_{25}$). However, the crystallinity is already high. All peaks have a small full width at half maximum (FWHM). It is approximately 0.193° for the (1 1 0) peak.

The purity increased after sintering (sample SA(1xsint)). The mass fraction of the monoclinic phase now amounts to nearly 100%. The sample is almost single phase. Moreover the crystallinity increased. The FWHM for the (1 1 0) peak is now about 0.183°. This is a decrease of 5%.

Another sintering step (sample SA(2xsint)) again increases the crystallinity for another 6%. The FWHM stands at 0.173°. However, the purity stays nearly the same because it has already been high in sample SA(1xsint). This is shown in figure 4.4.

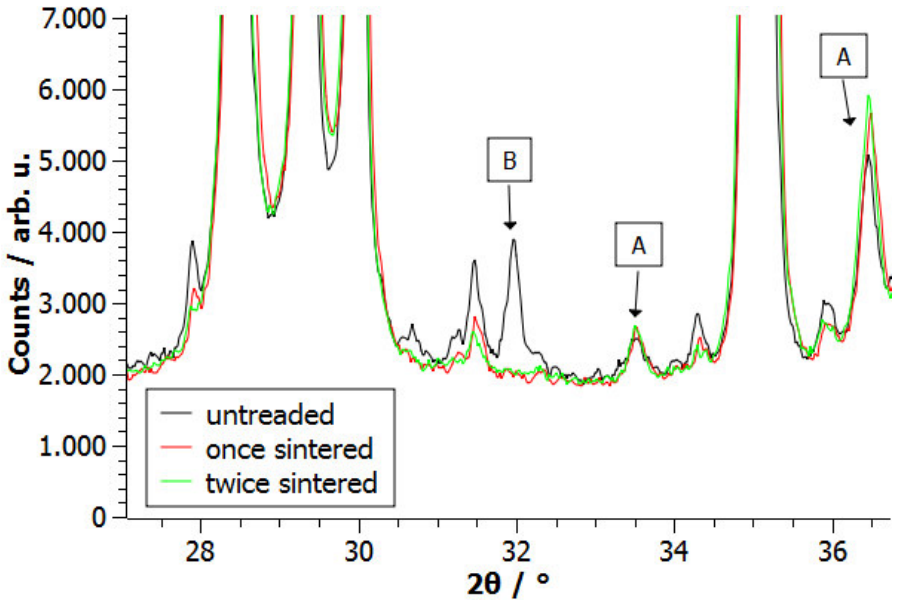

Figure 4.4.: The phase purity of the three SA samples are compared. The peaks labelled with *A* correspond to the $SrAl_2O_4$ phase.

The peaks labelled with *A* correspond to the $SrAl_2O_4$ phase that is desired. The peak labelled with *B* correspond to different phases. It already vanishes after the first sintering step.

Both the purity and the crystallinity determine the quality of the host material that is used for doping. Furthermore the procedural effort should be low. The crystallinity is high enough in all three samples. The purity increased from SA(untr) to SA(1xsint) but only scarcely changed from SA(1xsint) to SA(2xsint). On the other hand the

procedural effort increases. Therefore sample SA(1xsint) shows the best results in terms of crystalline properties versus effort. Thus it was decided to prepare all (co-)doped with only one sintering step.

The monoclinic α-$SrAl_2O_4$ transforms to a hexagonal phase at a temperature of 650°C. The combustion temperature was chosen to be below this temperature of phase transition. Nevertheless an overshoot would be possible because of the exothermic nature of the reaction. The thermoelement within the furnace showed temperatures of approximately 615°C. However, it only measures the atmosphere within the furnace and not the temperature in the beaker where the reaction takes place. Nevertheless the hexagonal phase was not formed. This makes sense because the samples were cooled down slowly enough to give them sufficient time to arrange in the monoclinic structure of the low temperature phase. The same applies for the sintering step that was far beyond the transition temperature.

Of both phases the monoclinic α-$SrAl_2O_4$ is this one that is responsible for the afterglow. The following paragraphs will give a detailed description of the structure of this phase. The $SrAl_2O_4$ phase is primitive monoclinic and has $P1211(4)$ symmetry. The empirical formula for the unit cell is $Sr_4Al_8O_{16}$. Hence the more common formula $SrAl_2O_4$ can be derived.

Al has a tetrahedral coordination sphere. There exist four different sites. All tetrahedra are corner-linked.

For O there exist two different coordination polyhedra. They are a distorted tetragonal planar and a tetrahedral coordination. The number of different O sites is six. The O^{2-} form the densest packing.

There are two different Sr sites. This is in agreement with literature. They are labelled as site A and B in figure 4.5. Both Sr ions have a CN of six. In both cases the polyhedra are distorted octahedra that do not differ very much. The differences can be best seen by the average Sr-O distances. For site A it is 2.621 $\AA$ whereas it is 2.613 $\AA$ for site B. Thus the deviation is only around 0.3% and the resulting CF is slightly different. Hence the corresponding emission spectra will only feature one band.

The figure also shows that the two sites with a different coordination sphere are closer than two sites with the same coordination sphere. The polyhedra of site A and B

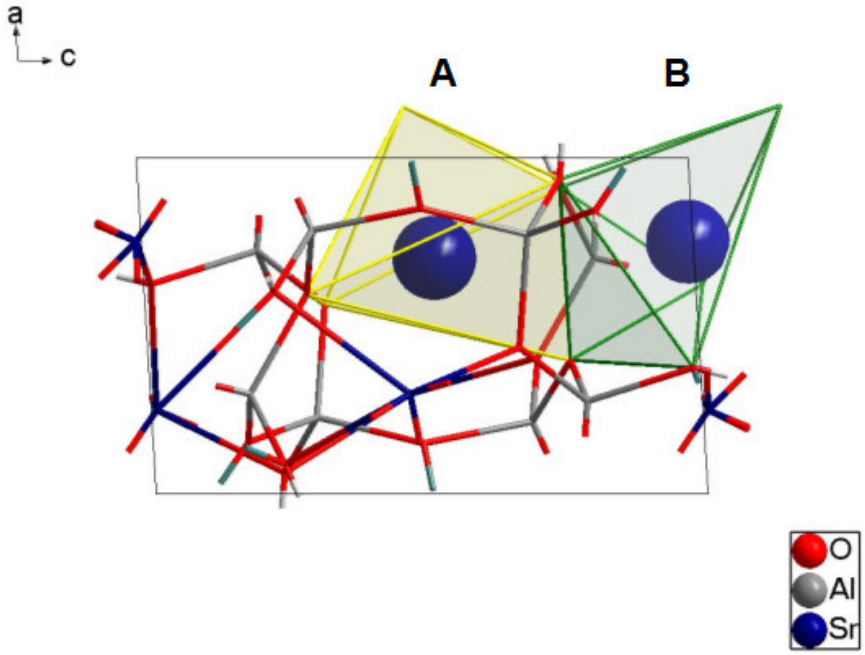

Figure 4.5.: The two Sr sites in α $SrAl_2O_4$: The *A* and the *B* in the picture sign the two different Sr sites.

share a face whereas each polyhedron is linked to one of the same type via two corners (see figure 4.6).

These two different Sr ions can be substituted by RE ions. The ion radii differ only slightly as can be seen from the Shannon radii [32]. For an octahedrally coordinated Sr^{2+} the ionic radius is 1.18 $\AA$. Table 4.1 gives all ionic radii of the RE used for doping in an octahedral coordination sphere. The average radius for O is about 1.37 $\AA$. For the Shannon radii ions are considered as hard spheres and crystals are regarded as purely ionic crystals. Therefore a sum of ionic radii must always be larger than the ion-ion distance in the crystal. This is also the case for $SrAl_2O_4$. Because the octahedron is distorted all Sr-O distances are different. The shortest is 2.51 $\AA$. This is only slightly shorter than the sum of the Sr and O radii which is approximately 2.54 $\AA$. If Sr, however, is substituted by an RE^{3+} ion the sum is even smaller. Regarding to Pauling compounds that include ions that are smaller than the voids of the densest packing are not stable. Perhaps this explains why the divalent Eu is even formed under non-reducing conditions as will be shown in chapter 3. With 1.17 $\AA$ the radius of Eu^{2+} is nearly the same as the Sr radius which gives a sum larger than the Sr-O distance. In

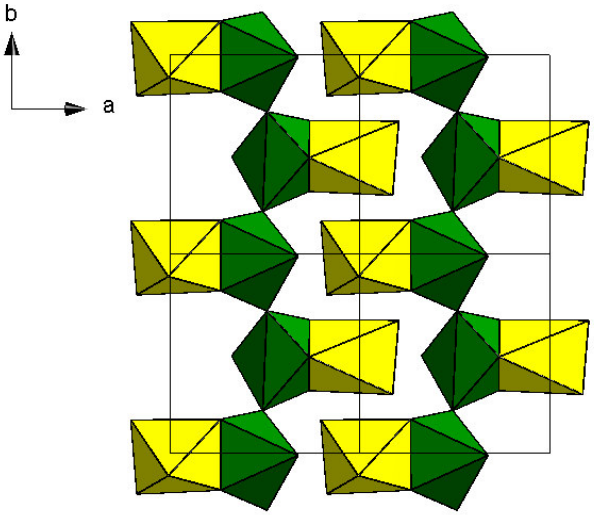

Figure 4.6.: Sr coordination polyhedra in α $SrAl_2O_4$: The two differently coloured polyhedra correspond to the two Sr sites. The pictures shows two layers of coordination polyhedra. The first, third and fifth row of polyhedra parallel to lattice parameter a correspond to the upper layer whereas the second and fourth row correspond to the lower layer.

contrast the trivalent Eu has a radius of 0.947 $\AA$ which gives a too small sum. Therefore the material needs to find a way to generate as much Eu^{2+} as possible. This can be done by forming V_O. Thus divalent Eu is generated without using a reducing agent. However, this concept is quite empirical. Its contribution to the reduction of Eu can be regarded as small.

It was tried to calculate the crystallite size by the Scherrer equation. However, all three samples show too narrow peaks which makes a size-determination impossible. Hence it can be derived that the powder is at most microcrystalline but not nanocrystalline. This is not in agreement with the literature where values between 12 and 62 nm for samples prepared by solution combustion are given [15, 33, 16, 34]. This seems to be contradictory. However, the solution combustion method contains parameters that are difficult to control. Some experiments that were done in the frame of a project laboratory show that the repeatability of this preparation is quite low. Therefore a single experiment is not meaningful. Further experiments would be necessary to determine a distribution of the crystallite sizes and out of it the average value for the size.

Table 4.1.: The Shannon radii of some octahedrally coordinated cations in the oxidation states 2+ and 3+. The entry 'none' means that the radius of the ion in this oxidation state was not determined. All values were taken from [32].

Element	R^{2+} / Å	R^{3+} / Å
Sr	1.18	none
Eu	1.17	0.947
Dy	1.07	0.912
Nd	1.29	0.983
Pr	none	0.99
Sm	none	0.958

To sum up the XRD experiments show that $SrAl_2O_4$ has a monoclinic phase with two different Sr sites. Moreover one sintering step is adequate to obtain a host material of suitable quality. Furthermore a calculation of the crystalline size by Scherrer equation was not possible because even of the unsintered samples the crystallites were too big.

4.1.2. Scanning Electron Microscopy

Figure 4.7 shows some ungrounded particles. It can be seen that they have a rough surface with some small pores. A magnification, however, shows that the particles still agglutinate (figure 4.8). The InLens detector - a kind of a secondary electron detector - shows that they form needle shaped and ball shaped agglomerates (figure 4.8a). Both entities, however, have the same shade of grey by using an energy selective backscattered electrons (ESB) detector (figure 4.8b). This means that the elemental composition is the same. Although this preparation did not allow further investigations it can be already seen that the particle size is beyond 1 μm. This implies that the samples are nanocrystalline. However, the particle size is not small enough to apply the Scherrer equation (see section 4.1.1).

The aqueous preparation disperses the agglutinated needle and ball shaped particles partly (figure 4.9a). The needles form bundles that are frayed on both ends. Hence they do not occur separated. The same applies for the ball shaped agglomerates. They

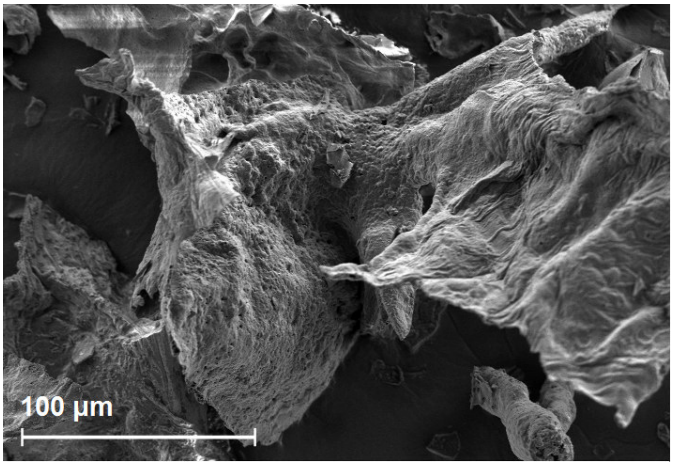

Figure 4.7.: SEM of the unsintered sample (direct coating): the overview shows that the particles agglutinate and form small pores. (detector = secondary electrons (SE))

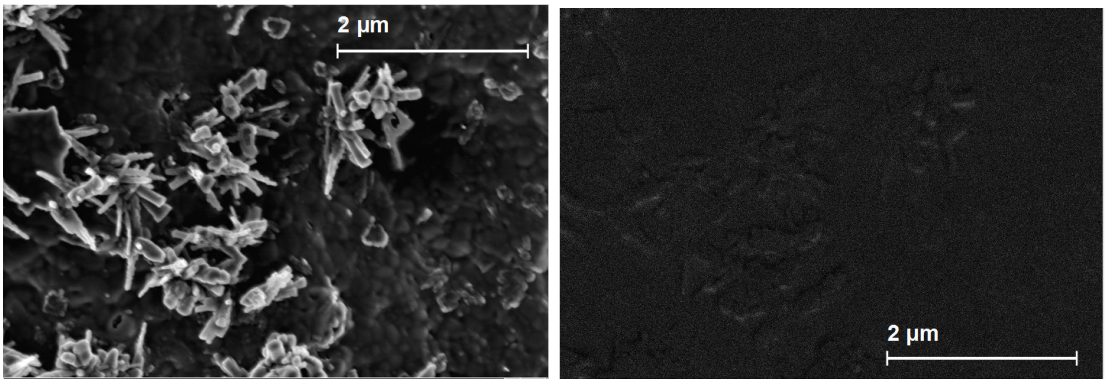

(a) **(b)**

Figure 4.8.: SEM of the unsintered sample (direct coating): InLens (a) shows that the sample consists of needle and ball shaped agglomerates. ESB (b) reveals that both structures have the same composition.

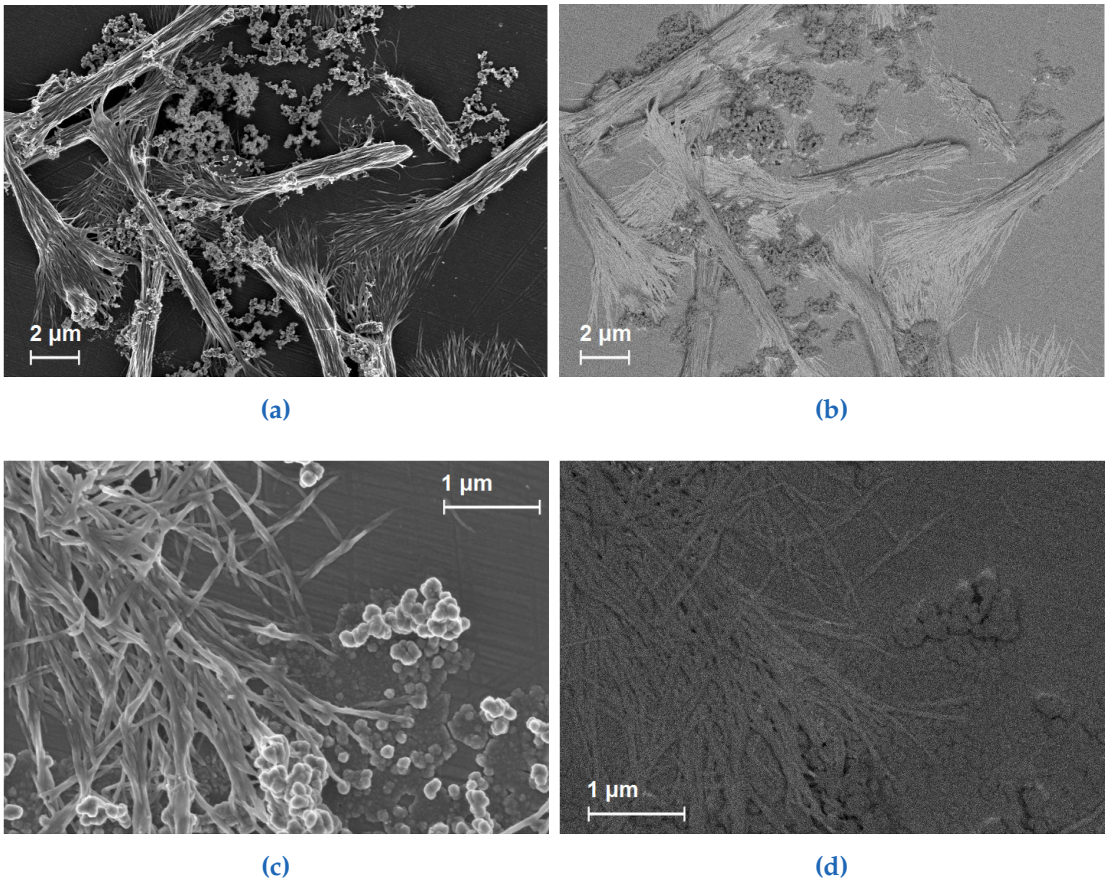

(a) (b)

(c) (d)

Figure 4.9.: SEM of the unsintered sample (water): overview InLens (a) and ESB (b); detail InLens (c) and ESB (d).

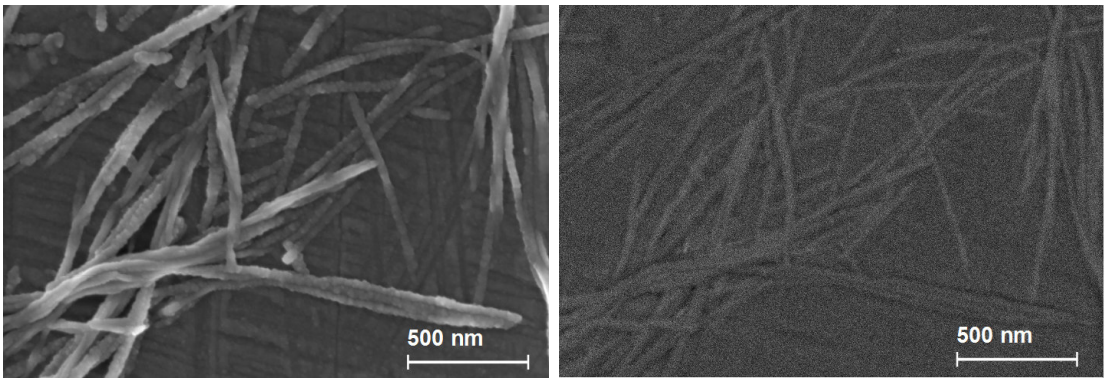

(a) (b)

Figure 4.10.: SEM of the unsintered sample (water): the needles seem to consist of balls. InLens (a), ESB (b).

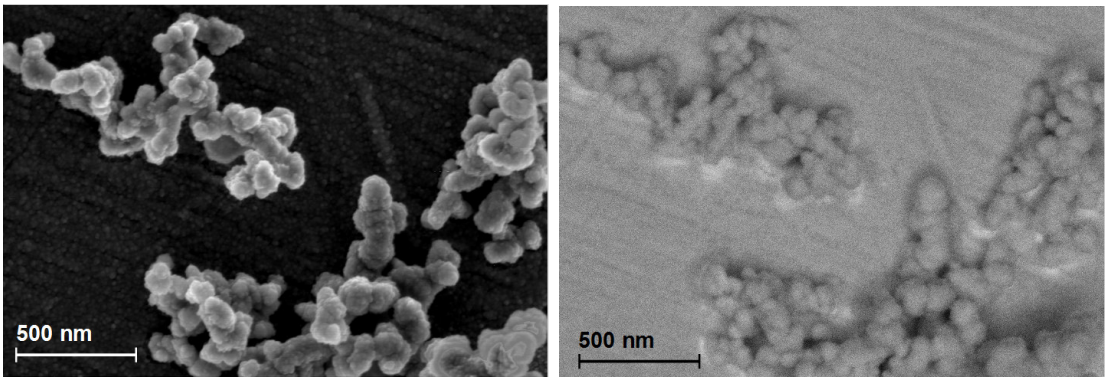

(a) (b)

Figure 4.11.: SEM of the unsintered sample (water): InLens (a) and ESB (b). The balls in the background have a smaller diameter and are lighter in their molecular weight.

agglutinate to heaps of balls. The ESB shows that the bundles are brighter than the heaps (figure 4.9b). This would imply that they consist of heavier elements. Hence both agglomerates are of different composition. However, it was not possible to figure out the empirical formula because the specimen was too thin for an energy-dispersive X-ray analysis (EDXA). Figure 4.9c and 4.9d show another comparison of the needle and ball shaped structures by using a higher magnification. Two special features of these both structures, however, can only be revealed under very high magnification. In some images the needle-like structures seem to consist of balls (figures 4.10). Another new feature can be discovered in figure 4.11a. Here it seems that the heaps are positioned onto balls that form the background. They have a much lower diameter than the heaps of balls. The ESB shows that they have the same composition.

Figure 4.12 compares the aqueous with the alcoholic preparation. The latter consist only of homogeneously distributed needles. They are much shorter than those of the aqueous preparation and they also do not occur as wads. Probably ethanol disconnects the needles better than water.

All these results of sample SA(untr.) can not be fully understood. Further investigations that were not done in the frame of the master thesis are necessary. For instance a thicker film on the sample holder or a measurement with TEM would have led to more results to explain the observations discussed above.

The two sintered samples SA(1xsint) and SA(2xsint) barely differ in their microscopi-

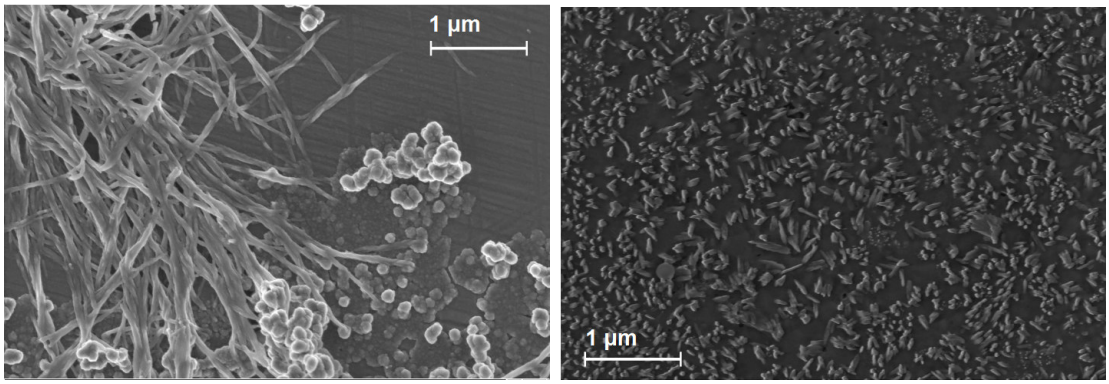

(a) (b)

Figure 4.12.: SEM of the unsintered sample: comparison of the unsintered samples after preparation with water (a) and ethanol (b). In the latter the needles seem to be much shorter and do not agglutinate (detector = InLens).

cal appearance. Therefore they will be discussed together. Figure 4.13 gives an overview of the preparation. The high definition angle selective backscatter (HDAsB) detector enables to distinguish between areas with different composition. The powder forms bright structures that are surrounded by black areas of the hardened epoxy. It can be already seen that the bright areas consist of grains with domains. This grains are surrounded by grey areas. The grains and the grey areas have different compositions. An EDXA analysis showed that the grains have the empirical formula of $SrAl_2O_4$ whereas the grey areas are richer in Al (figure 4.14 and appendix D). Because the EDXA analysis is afflicted with errors the exact empirical formula of the grey areas cannot be easily calculated. A strict determination would result in $Sr_2Al_5O_9$. This, however, would not be a charge neutral compound. The excess of Al probably arises from something different.

A high resolution of the grains shows that there are three possible arrangements of the α-structure as claimed in literature [8]. There are strip shaped structures (signed as *A* in figure 4.15) wedge shaped structures (*B* in figure 4.15) and patchwork shaped structures (*C* in figure 4.15). The strip shaped structures consist of two variants of the α-phase in twin relationship. The wedge shaped structure consist of four different variants of α-phase. The same applies for the patchwork structure. The twin relationships, however, are different to the wedge shaped structure.

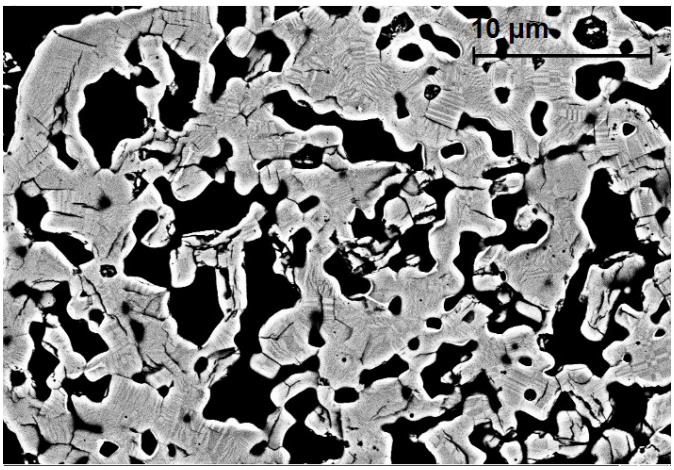

Figure 4.13.: SEM of the sintered sample: the white areas correspond to the sample. There can be already seen that it consist of grains with domains. They are surrounded by black areas that correspond the hardened epoxy (detector = HDAsB).

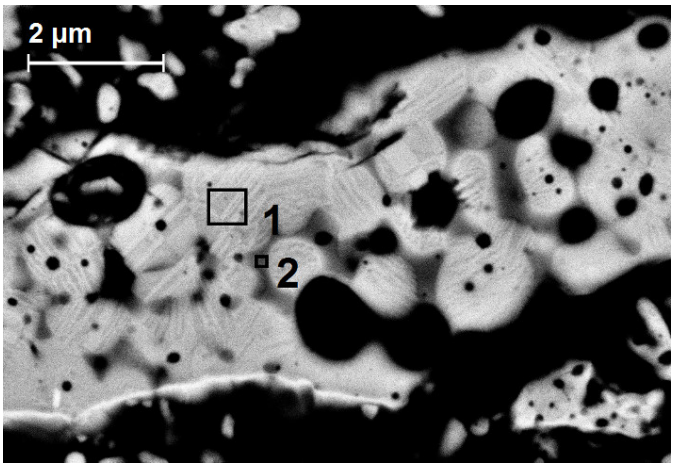

Figure 4.14.: SEM of the sintered sample: the two different shades of grey correspond to areas with different composition. The black framed squares mark the areas that were used for the EDXA (see appendix D) (detector = HDAsB).

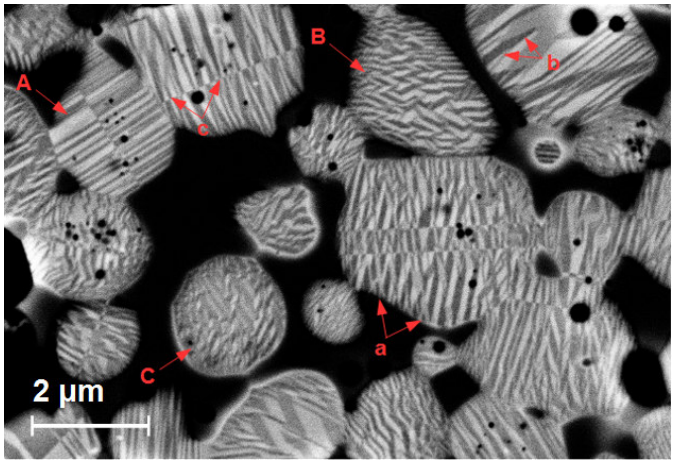

Figure 4.15.: SEM of the once sintered sample: the description for the labels *A*, *B*, *C*, *a*, *b* and *c* can be found in the text (detector = HDAsB).

All this variants of the α-phase arise due to stacks of unit cells that have different orientations to each other. A weak dipole moment can be the driving force for such an arrangement in domains.

Figure 4.15 also reveals that there exist three kinds of boundaries. The grain boundaries that border the grains (*a* in figure 4.15), the domain interfaces that border two domains from each other (*b* in figure 4.15) and the defect interfaces that border two stacks of domains (*c* in figure 4.15). In the latter two different variants of the α-phase meet each other.

The average size of the grains cannot be determined because of the two dimensional nature of the image. The picture only displays the cross sections of the grains. However, there cannot be derived any information of the cross section's position. In other words there is no guarantee that the centre of the grain lays in every cross section of every grain. Even if this were the case there would be a dependency of the diameter on the shape of the grains. A shapeless object can have an infinite number of different cross sections. The same applies for the comparatively highly symmetrically shape of an ellipsoid. A trustful determination of the average grain diameter is therefore not possible. Similar to the results of the unsintered sample further investigations are necessary to obtain more detailed information.

4.1.3. Optical Characterisation

As expected undoped $SrAl_2O_4$ neither absorbs nor emits visible light. However, it absorbs light of the UV and NIR range as it can be seen in figure 4.16.

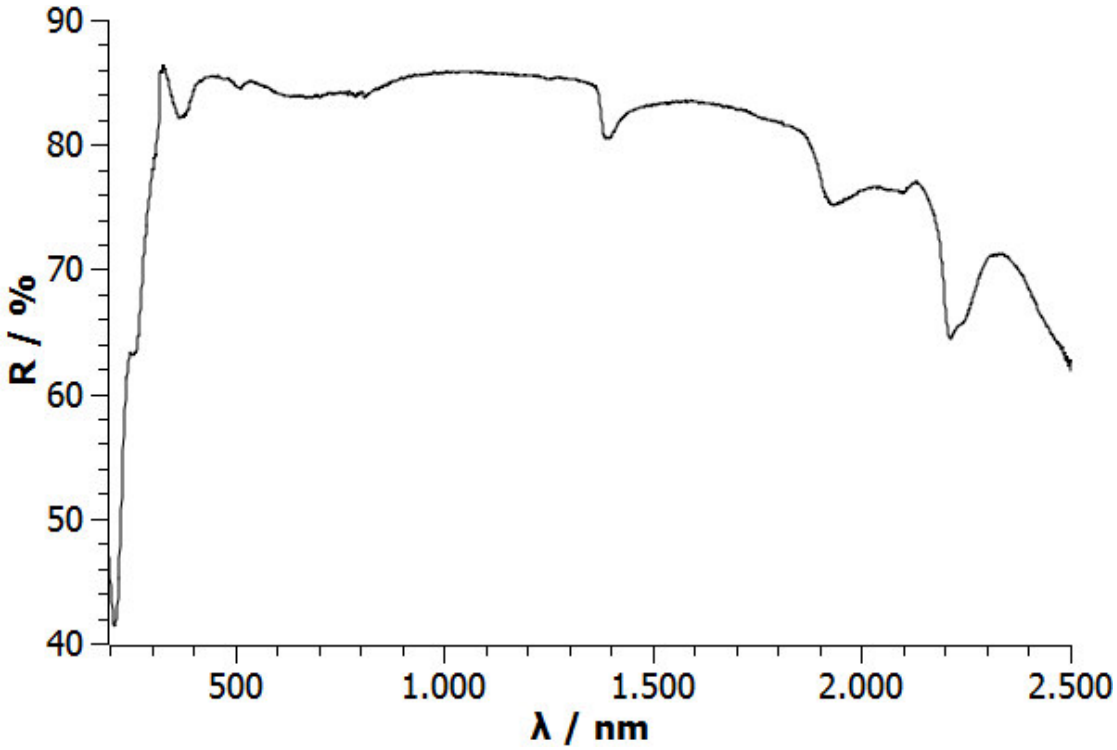

Figure 4.16.: Reflectance Spectrum of undoped $SrAl_2O_4$: The spectra covers the NIR, the VIS and the UV. The bands in the NIR correspond to vibrations and the band in the UV to the band gap. There are, however, no absorptions in the VIS.

Lamp: D / W	Detector: PMT / InGaAs	Start: 2500 nm
Finish: 200 nm	Step size: 1 nm	Slit size: 2 nm

In the NIR range all observed bands are vibrational overtones. The band at around 1390 nm is a O-H vibrational overtone. It emerged because of the moisture in the air that is absorbed on the sample surface. The other two bands at 1930 and 2210 nm are overtones or combinations of vibrations of the lattice (e.g. Al-O vibrations).

The UV range is dominated by the band gap absorption. It begins at 320 nm by forming an electron-hole pair. However, the band gap cannot be directly determined from this spectrum. One possibility to find out the optical band gap is by using the Tauc plot. In this modification of a reflectance spectrum energy is plotted against squared

energy. The unit of E is usually in eV. The x-axis of the reflectance spectrum which has the dimension of wavelength can be directly transformed into energy. For this purpose the values in nm are multiplied with the corresponding constants to obtain values in eV.

$$f\frac{hc}{\lambda} = E \tag{4.1}$$

With f as a factor to convert J into eV ($\approx 6.24 * 10^{18}$), h as the Planck constant, c as the speed of light in vacuum, λ as the wavelength and E as the energy in eV. The y-axis, however, needs more modification steps. First of all the Kubelka-Munk function is set up. It is a function of the reflectance.

$$F(R) = \frac{(1-R)^2}{2R} \tag{4.2}$$

In this equation the reflectance R is dimensionless. The same applies for the Kubelka-Munk function $F(R)$. In the next step the function is further modified.

$$[F(R)fh\nu]^2 = [F(R)fh\frac{c}{\lambda}]^2 = \tilde{F}(R,\lambda) \tag{4.3}$$

Here $\tilde{F}(R,\lambda)$ is an expression for the term on the left side of this equation. The latter, however, is not written down. The Tauc plot usually plots E in eV against $[F(R)fh\nu]^2$ in eV^2.

The Tauc plot for the sample is shown in figure 4.17. It shows a function that stays about constant till 5.3 eV, then increases steadily and finally levels off around 5.8 eV. The rising part can be fit with a linear function. The point where this line crosses the x-axis discloses the value for the optical band gap in eV. In this case at 5.29 eV. However, this value is afflicted with large uncertainties. Two important influences on the result can be due to temperature and excitonic effects [35]. Both can lead to a substantial reduction of the band gap. The former because of the band broadening and the latter because of the stabilisation energy due to the exciton formation. This explains why the

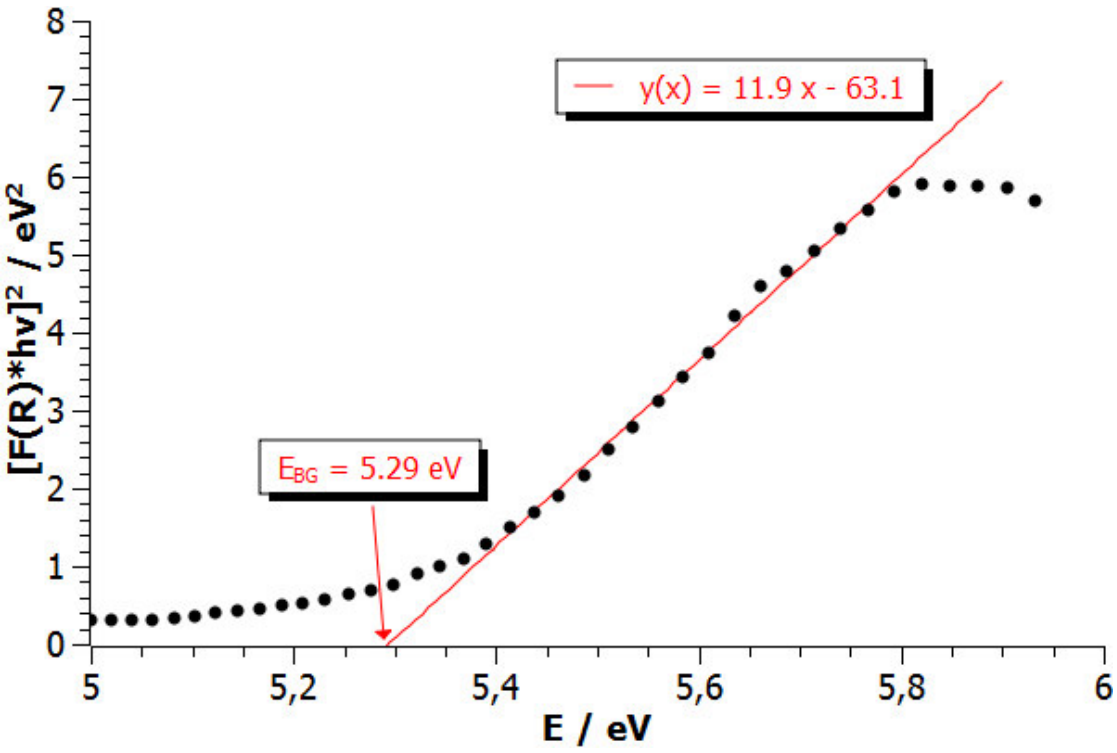

Figure 4.17.: The Tauc plot of $SrAl_2O_4$: The red line is the linear regression that reveals the band gap energy where it crosses the x-axis. With the help of the equation of the line the band gap was calculated to be 5.29 eV.

experimentally determined band gap is 6.5 eV [36]. This leaves a deviation of 19% with the optical band gap obtained from the Tauc plot.

4.2. $SrAl_2O_4$:RE - Singly Doped $SrAl_2O_4$

4.2.1. Optical Characterisation with the UV Lamp

Depending on their composition and preparation the samples show different behaviour under the UV lamp. Only the sintered sample SA,Eu^{2+}(1) showed an afterglow of about 0.5 s. Most of the as-prepared foams show an inhomogeneous glowing under the UV lamp. For instance some of the Eu containing samples show the green as well as the red luminescence that is characteristic for Eu^{2+} and Eu^{3+}, respectively (figure 4.18). There were some areas of the foam that show predominantly green and red fluorescence. The latter was especially observed on the surface which is more sensitive to the oxidizing

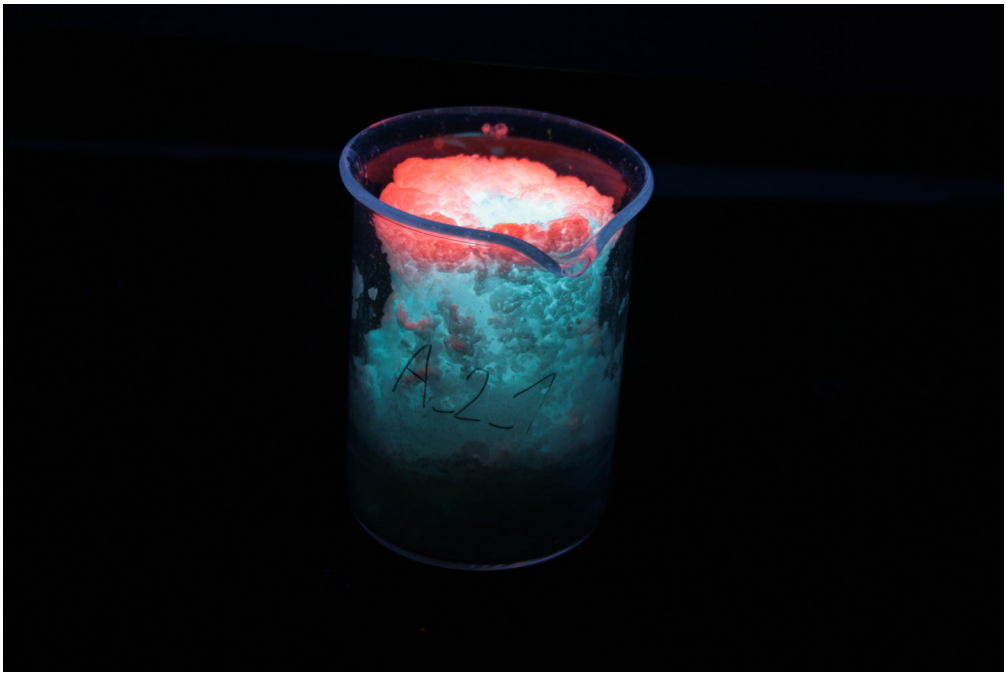

Figure 4.18.: Unsintered SA,Eu(1) under the UV lamp: the sample shows areas of green and red glowing, respectively. The chosen wavelength was 254 nm.

Table 4.2.: The singly doped samples under the UV lamp. The strength are values relative to the sintered sample SA,Eu^{2+}(1) under the wavelength of 365 nm. 0 means that no luminescence was observed. A (-) in the column *duration* means that the glow vanished instantaneously.

		365 nm			254 nm		
Sample		Colour	Strength	Duration	Colour	Strength	Duration
SA,Eu(1)	unsint.	green	1	-	-	0	-
	sint. (2+)	green	3	0.5 s	green	2	0.5 s
	sint. (3+)	green/red	1	-	red	2	-
SA,Dy(1)	unsint.	red	1	-	-	0	-
	sint.	red	1	-	-	-	-
SA,Nd(10)	unsint.	-	0	-	-	0	-
	sint.	-	0	-	-	0	-
SA,Pr(1)	unsint.	red	1	-	-	0	-
	sint.	red	1	-	-	0	-
SA,Sm(1)	unsint.	red	1	-	-	0	-
	sint.	red	1	-	-	0	-

atmosphere. All results of the samples in powder form are summed up in table 4.2.

4.2.2. Optical Characterisation with the Fluorescence Spectrometer

A detailed optical characterisation is only possible with a fluorescence spectrometer. All samples show their characteristic emission/excitation spectra depending on their composition. The spectra of the unsintered samples are only discussed when considerably differences to the sintered samples were found.

Most of the spectra, however, show bands that can be identified as artefacts. They emerge because the outer ring of the sample holder shows an unwanted luminescence. Therefore a spectrum of the empty sample holder was recorded (figure 4.19). The excitation for the emission spectrum was 200 nm. It shows a couple of broad and narrow bands. Bands that often show up in the spectra of the samples with weak emissions are located at 424, 447, 460, 485 and 530 nm. These will not be assigned in the sample spectra. Fortunately, the spectrum of the sample holder has a short life time. All bands completely vanish after 0.1 ms. The bands of the RE, however, usually have a much longer life time. This can be used to distinguish between bands of the sample and bands of the sample holder. Figure 4.20 gives an example for bands that arise because of the sample holder and the sample, respectively.

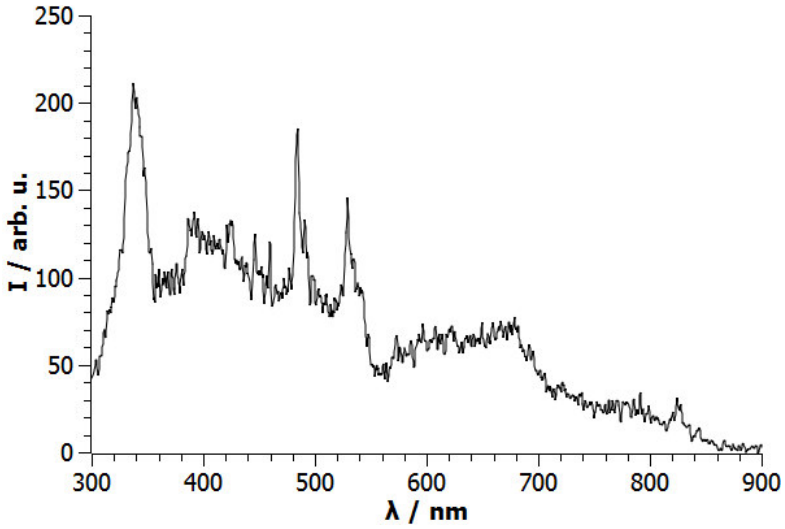

Figure 4.19.: The emission spectrum of the sample holder.

The unsintered sample SA,Eu(1) features three Eu emissions of presumably different origin. Two of them are represented by broad bands (Eu1 at 491 nm and Eu2 at 404 nm) and one by a narrow band (Eu3 at 610 nm). Their excitation/emission spectra are

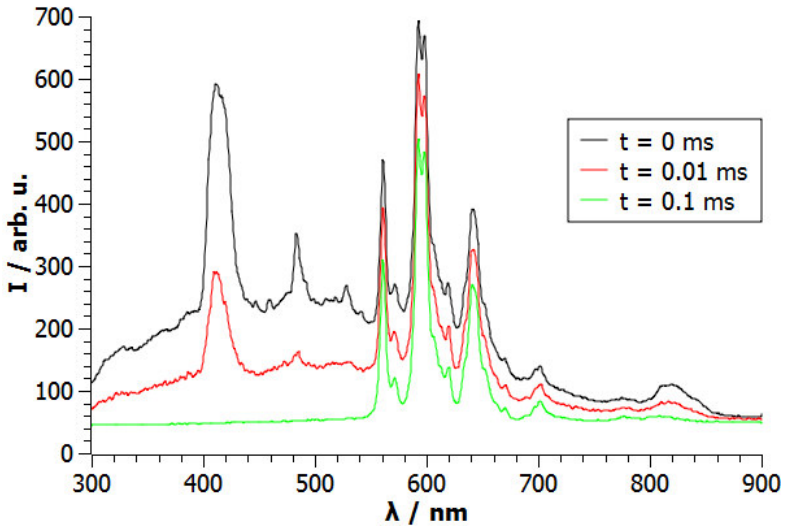

Figure 4.20.: Time dependance of the sample holder's emission: the spectra show the emission bands of Sm^{3+} and the sample holder. After 0.1 ms all emissions of the latter vanished.

shown in figure 4.21.

Eu1 is the characteristic luminescence of Eu^{2+}. The band is located at 492 nm and therefore corresponds to a green emission. The excitation spectrum of Eu1 shows the band gap and two broad bands at longer wavelengths. The former is the excitation of electrons from the VB into the CB thereby creating a hole in the VB. The onset should be at 191 nm [26]. Nevertheless the band gap transition can be seen because of the line broadening. The two broad bands at 270 and 350 nm contain a great deal of further bands that merge into each other. One of them is the CT band. According to literature it should emerge at approximately 254 nm [37]. It describes the transfer of an electron from Eu^{2+} to the host material. During this process Eu^{2+} is oxidized to Eu^{3+}. It is apparent that the CT needs to start at the Eu^{2+} state. The final state, however, can be different. The electrons can be taken up by the CB of the host but also V_O and perhaps also other defect levels can trap the electrons. Because there are eight different oxygen sites there can be up to eight CT bands. However, their energies might be similar and they cannot be resolved in the spectrum. The remaining two broad bands are IC transitions ($4f^7 \rightarrow 4f^6 5d^1$). This multiplicity of bands occur because of CF splitting and can be explained by the environment of Eu^{2+}. It is coordinated by a distorted octahedron of oxygen ions. This leads to the further splitting of the common e_g and t_{2g}

terms. Depending on the symmetry of the coordination polyhedron there can be up to five bands. However, they cannot be resolved within the two broad bands at 270 nm and 350 nm. Even in literature their positions in the excitation spectrum is not uniform. However, all of these excitation bands independent of their origin (CT or IC) lead to the emission at 492 nm shown in figure 4.21. It is the $4f^6 5d^1 \rightarrow 4f^7$ transition of Eu^{2+}. The emission from the d configuration is possible because the CF-split 5d orbitals of divalent Eu are lowered below the 4f configuration that is responsible for the emission of Eu^{3+}. The intensity, however, varies depending on the excitation band. In literature it was mentioned that the broad Eu1 emission contains the two bands that correspond to the two occupied Sr sites. This explains why the broad band is slightly asymmetric. However, this will be further discussed for the sintered sample.

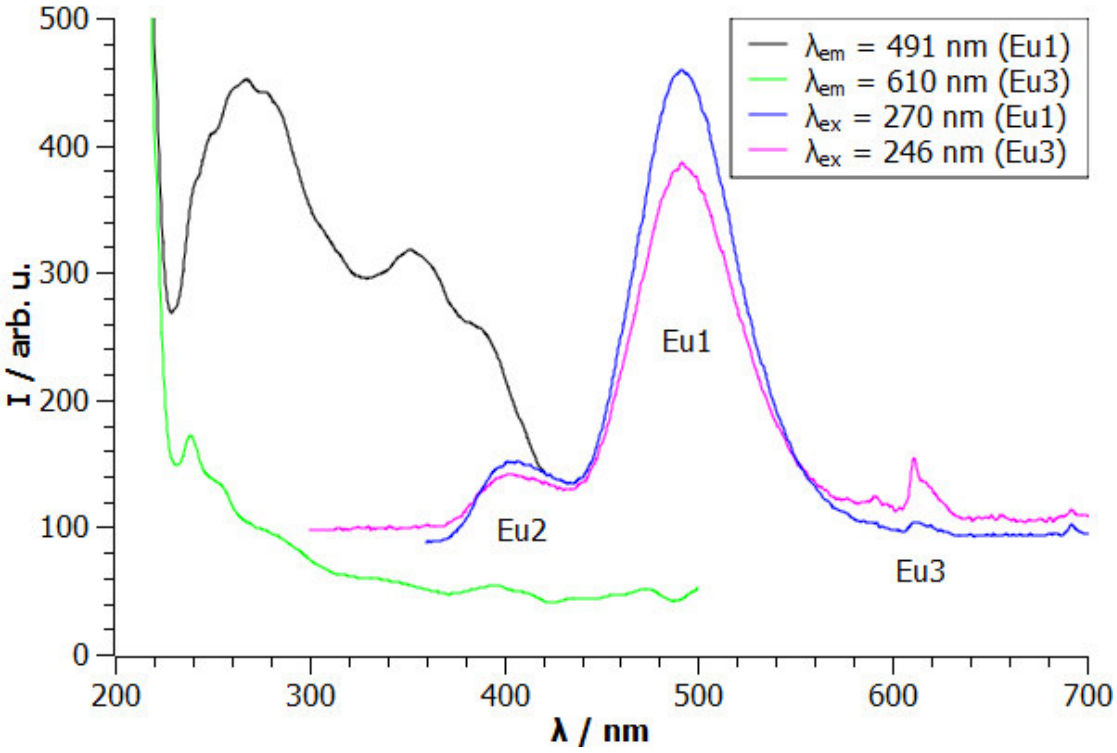

Figure 4.21.: Emission / excitation spectra of unsintered SA,Eu(1)

Em. slit: 3 nm	Voltage: 700 nm	Delay: 0 ms

The emission of Eu2 is much lower in intensity than that one of Eu1. The emission band is located at 404 nm. The band, however, does not produce a suitable excitation spectrum. Hence neither an excitation nor an emission spectrum was recorded.

Nevertheless the emission band can be seen in the spectrum of Eu1. The emission of Eu2 at 404 nm is broad and corresponds to blue light. As will be seen later this band only emerges in unsintered samples. Therefore, the band can originate from a second phase that was formed during solution combustion. The X-ray spectra of the undoped $SrAl_2O_4$, however, showed that the sample is nearly single phase even without sintering. As already mentioned solution combustion forms nano- or micro-crystalline foams. This means that the crystallisation starts at many different locations inside the reaction sphere. The compound that is formed will depend on the ratio of the elements in the vicinity of such a starting spot. Because of the stoichiometry of the reactants $SrAl_2O_4$ will be predominately formed. This explains the high purity of the unsintered products. The doped samples, however, were prepared by using trivalent Eu that occupy Sr sites. Thus the charge of the reacting atoms is not balanced (see equation 3.4). This will lead to Sr vacancies in the product and therefore to an excess of Sr that is available for alternative reactions. Moreover the trivalent ions can start a different reaction than the divalent Sr. This two facts will lead to a stronger formation of side products. Nevertheless the majority of the trivalent Eu will still form the doped $SrAl_2O_4$ phase. The remaining Eu^{3+}, however, will react to an other phase that can be also reduced to Eu^{2+}. Because of the different crystal structure the resulting CF will be different leading to the $4f^6 5d^1 \rightarrow 4f^7$ transition at 404 nm. The intensity, however, is quite low compared to the Eu1 emission because the formation of the second phase is limited.

The third band, Eu3, corresponds to the emission and excitation of Eu^{3+}. The excitation wavelength of 246 nm was forestalled from the sintered sample SA,Eu^{3+}(1). The emission is around 610 nm. This corresponds to red light. However, it is quite low in intensity showing that preferably Eu^{2+} is formed during solution combustion. Sample SA,Eu(3+) will give a better optical characterisation of the trivalent Eu species.

The emission spectra show that there are both Eu species inside the unsintered sample. The ratio of Eu2+ and Eu3+, however, can not be quantified because the intensity of the bands depends not only on the amount of a species but also on the transition dipole moment which is much higher for the IC transition. Further measurements of samples with known Eu^{2+}-Eu^{3+} ratio would be required for a quantitative determination of

the ratio. However, this was not the task of this master thesis. It is more interesting to answer why there are two different Eu species present at all. For this purpose the process of solution combustion needs to be considered from a theoretical point of view. The amounts of Sr and Eu for the reaction were adjusted in such a manner that the product was formed without any side products (see 3.4). In this equation

$$n(Sr(NO_3)_2) + n(Eu(NO_3)_3) = (1-\alpha) + \alpha = 1$$

Hence no excess was used and the reaction cannot be described as classical substitution. The formation of the product can be described using Kröger-Vink notation (only Sr, Eu and O are considered) as follows:

$$(1-\alpha)Sr^{2+} + \alpha Eu^{3+} + 4O^{2-} \longrightarrow (1-\alpha)\mathrm{Sr_{Sr}} + \alpha\mathrm{Eu_{Sr}^{\bullet}} + 4\mathrm{O_O} \tag{4.4}$$

In this equation the product is described to consist only of Sr and O sites. Hence Eu occupies a Sr site. This equation does not comply with charge neutrality in the product. The formed doped $SrAl_2O_4$ would be positively charged. Therefore it must find a possibility to get rid of the charge. One possibility is the indirect substitution of the Sr site

$$2\mathrm{Eu_{Sr}^{\bullet}} + 3\mathrm{Sr_{Sr}} + O^{2-} \rightleftharpoons 2\mathrm{Eu_{Sr}^{\bullet}} + 2\mathrm{Sr_{Sr}} + \mathrm{V_{Sr}''} + SrO \tag{4.5}$$

This reaction equation resembles equation 1.7. However, this is not a classical substitution because the Sr site was not initially occupied by Sr. Because even O^{2-} is stoichiometric this reaction needs an additional agent that supplies O^{2-} or promote the formation of O^{2-}. This anion can come from the urea that is used as a fuel or from not fully oxidized gases that are formed during the reaction. After this reaction the product is neutral but only consists of trivalent Eu. Therefore a second reaction is needed

$$2\mathrm{Eu_{Sr}^{\bullet}} + \mathrm{O_O} \rightleftharpoons 2\mathrm{Eu_{Sr}} + \mathrm{V_O^{\bullet\bullet}} + 1/2O_2 \tag{4.6}$$

In this reaction O escapes as molecular oxygen leaving behind two electrons. This electrons can be taken up by Eu^{3+} to reduce it to Eu^{2+}. The reaction strongly depends on the partial pressure of oxygen in the air. Hence the atmosphere can be used to shift

the equilibrium to the left or right side depending on what species is desired. This was utilized in the sintering procedures to prepare samples SA,Eu(1) and SA,Eu(3+), respectively. Both should only consist of one Eu species.

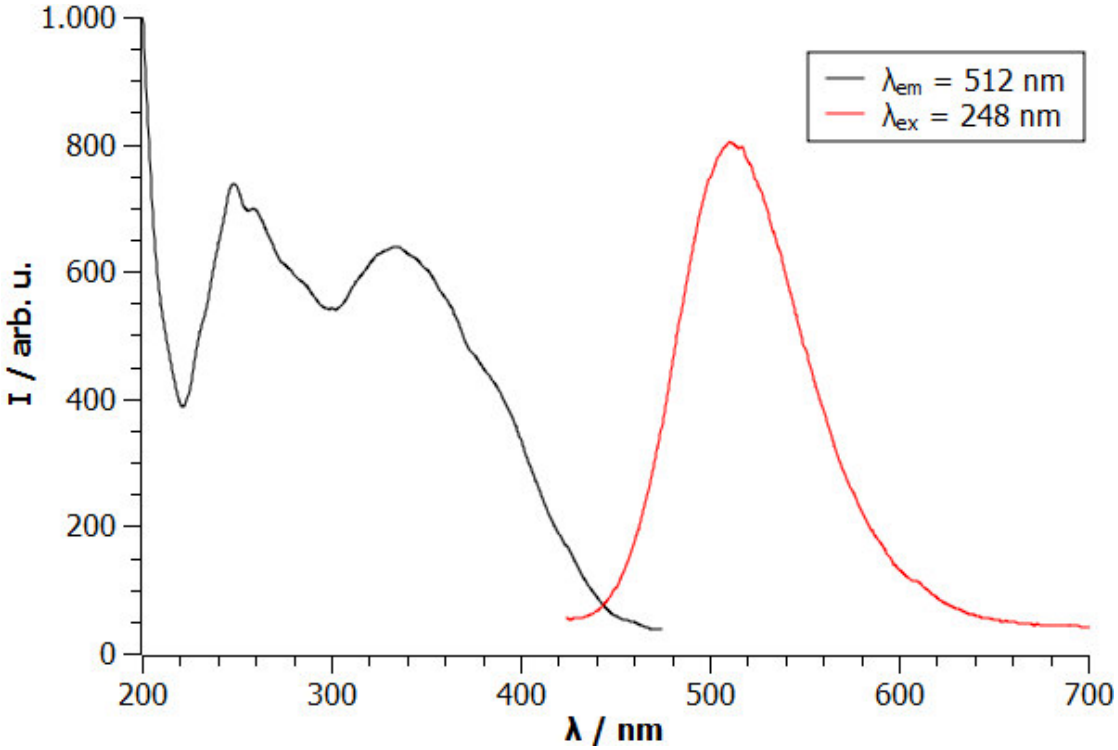

Figure 4.22.: Emission / excitation spectra of sintered SA,Eu^{2+}(1)

Em. slit: 3 nm	Voltage: 700 nm	Delay: 0 ms

The spectrum of the sintered sample SA,Eu^{2+}(1) shows that Eu was completely reduced during the sintering step (figure 4.22). Hence the equilibrium of equation 4.6 is almost completely on the right side. Oxygen is not only removed due to the gas flow but also because of the reaction with hydrogen.

$$O_2 + 2H_2 \rightarrow 2H_2O \tag{4.7}$$

Therefore no free oxygen is available and the back reaction (equation 4.6) is prevented.

The excitation spectrum shows again two broad bands similar to the unsintered sample. The emission spectrum is dominated by Eu1. Nevertheless the red Eu^{3+} emission can be assumed to be located at 610 nm (Eu3). This small shoulder shows that the reduction was not complete and that there is still a tiny amount of Eu^{3+} in the sample.

However, the amount of Eu^{3+} that remains can be neglected. Furthermore the emission spectrum does not feature the second band Eu2. This makes sense because sintering increases the phase purity noticeably.

Both the emission spectrum and the excitation spectrum resemble those of the unsintered sample. They are compared in figure 4.23. The intensities of the bands differ considerably. However, it should be mentioned again that the interpretation of absolute intensities is problematic because the powder samples were difficult to measure reproducibly with the available spectrometer. Moreover both excitation spectra feature two broad bands that consist of many further bands. However, they differ in shape and intensity. Another obvious difference is the position of the bands in the excitation and the emission spectra. The excitation bands of the sintered sample are shifted from 335 and 270 nm to 330 and 248 nm, respectively. The emission band is shifted to longer wavelengths from 492 to 512 nm. Hence the Stokes shift increases. This can be explained with a rearrangement of the ions and a thereby increasing crystallinity and phase purity that is achieved during sintering. Nevertheless it cannot be explained why the excitation bands move to shorter and the emission band to longer wavelengths.

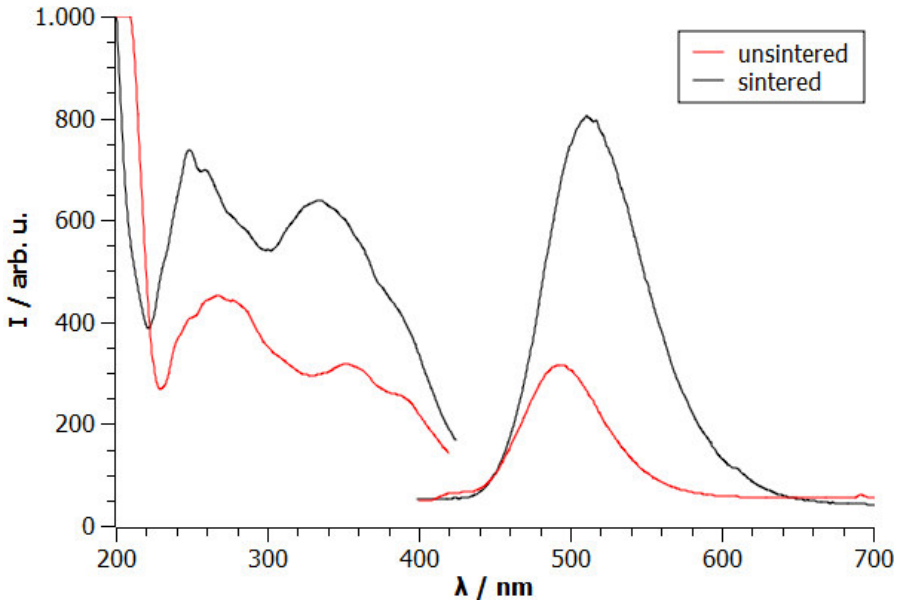

Figure 4.23.: Comparison of unsintered with sintered SA,Eu(1).

Em. slit: 3 nm	Voltage: 700 nm	Delay: 0 ms

Because of the fast decay only the measurement of the short time range was successful.

The emission band moved to shorter wavelengths during the decay (figure 4.24). This is perhaps due to the existence of the two occupied Sr sites which have probably a different decay behaviour.

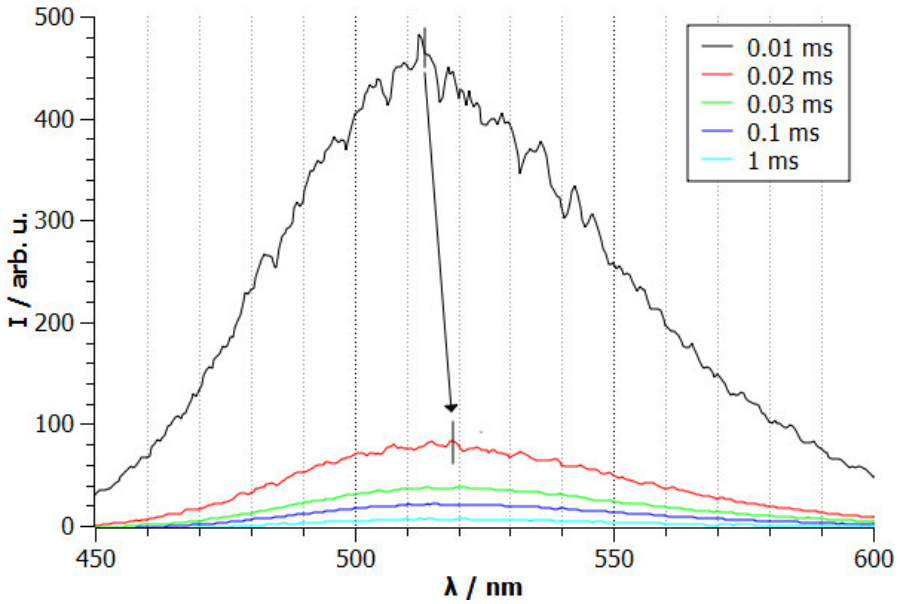

Figure 4.24.: Some emission spectra at different delay times: the band maximum shifts from 512 nm to 518 nm.

Em. slit: 3 nm	Voltage: 700 nm	Delay: see figure

Before the decay curves and decay constants can be determined from the experimental emission spectra the optical measurements need to be processed. Processing consisted of a baseline correction followed by an integration. For this purpose all emission spectra were first shifted by means of I_{700nm} to avoid an integration over the background. Actually, the background should be on the same level for all spectra because the measurement conditions were the same and 700 nm seems to be far away from the bands maximum and flanks. However I_{700nm} was different for all curves. Hence it was assumed that these values are a sum of the background and the flank of the outspread bands. It would lead to possibly grave errors if there were used an individual I_{700nm} for every curve. Therefore an average $\bar{I}_{700nm}$ needs to be determined. After the background correction the curves were integrated. The interpolation of the integration was linear. Finally, the time can be plotted against the areas. It was decided to fit the decay between 0 and 0.1 ms.

The measuring points show that the decay decreases tremendously within short time and then levels out (figure 4.25). Exponential but also reciprocal functions can describe this strictly monotonic decreasing decay. At the same time the fitting function should reveal a mechanism and the fitting parameters some physical quantities that are characteristic for the mechanism (e.g. trap depth or thermal energy). However, this is difficult because the mechanism is complex and obscure. Therefore, it was tried to fit the decay as well as possible. In addition the fitting parameters should be used to disclose trends within a sample series.

The fitting functions used in literature are mainly exponential functions [38, 39, 40]. Hence it was tried to fit the function with a single exponential decay. However, the fit was not good. Therefore the function was developed to a double exponential decay.

$$I(t) = A_1 e^{-t/\tau_1} + A_2 e^{-t/\tau_2} \tag{4.8}$$

The fit was much better but the decay constants yielded strange values. The first decay time gave a sensible value but the second was in the order of 10^{100}. Hence the second exponential term can be considered as constant and the resulting fitting function was

$$I(t) = y_0 + A e^{-t/\tau} \tag{4.9}$$

In this equation y_0 equals A_2, A equals A_1 and τ equals τ_1 of equation 4.8. This means that there is a second decay process that cannot be described by an double exponential function. The constants of equation 4.9 have either no physical meaning or do not directly reveal it. Therefore, they were modified in later discussions to enable comparisons of samples. The correlation coefficient was still not satisfying enough but a fit with an triple exponential function led to the same pre-factor and decay constant for each exponential term (e.g. for a function of second order was A_1 equal to A_2 and t_1 equal to t_2). An attempt to fit the decay with a reciprocal function (Becquerel function) lead also to a poor correlation. Hence it was decided to use the single exponential decay for all other short time measurements of the co-doped samples.

The fitted decay curve of sample SA,Eu^{2+}(1) is given in figure 4.25. The decay constants are given in table 4.3.

Table 4.3.: Decay constants of SA,Eu^{2+}(1)

y_0	−626	A	78526	τ	0.011 ms

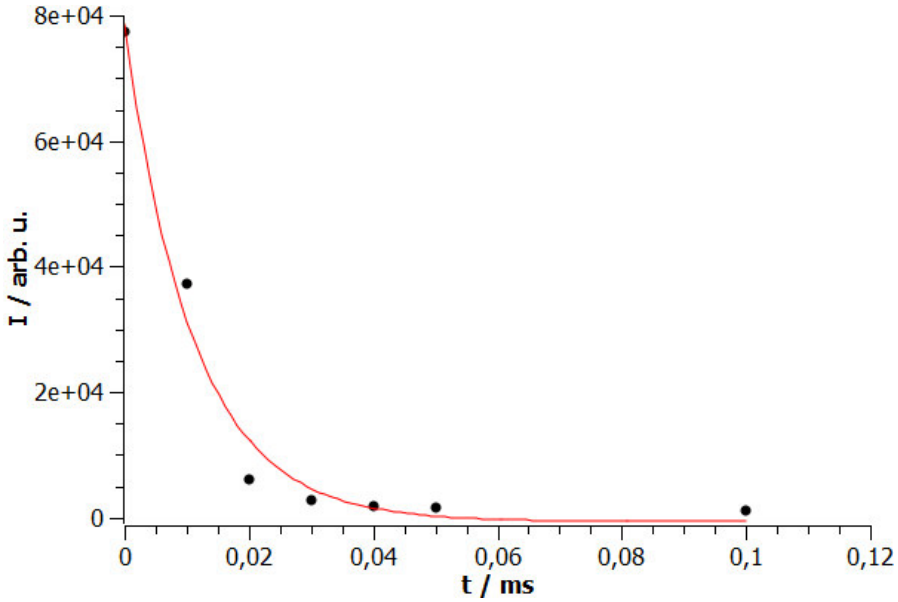

Figure 4.25.: Decay curve of SA,Eu^{2+}(1): the decay constants can be found in table 4.3.

Using the spectra recorded at different delays after the excitation pulse the slightly asymmetric $5f^6 4d^1 \rightarrow 5f^7$ transition was fitted with two Gaussian peaks. Although no shoulder or any other feature was visible the fitting was successful. The results are shown in figure 4.26. The initial band at 512 nm can be described with two Gaussian functions located at 506 and 540 nm. This would correspond to a difference in CF of 0.15 eV. The value found in the literature is 0.13 eV [24]. This is a quite good agreement. Furthermore the height of the two bands is also different. This means that the Eu ions are not uniformly distributed. There seems to be one favoured and one less favoured site. This can explain why the unresolved band can occur at slightly different positions in spectra of samples with different preparation conditions. It indicates that the distribution of the Eu ions also depends on some processing parameters.

The emission/excitation spectrum of sample SA,Eu^{3+}(1) is a proof that Eu stays in the trivalent state (figure 4.27). This is because of the oxidizing properties of the air. It

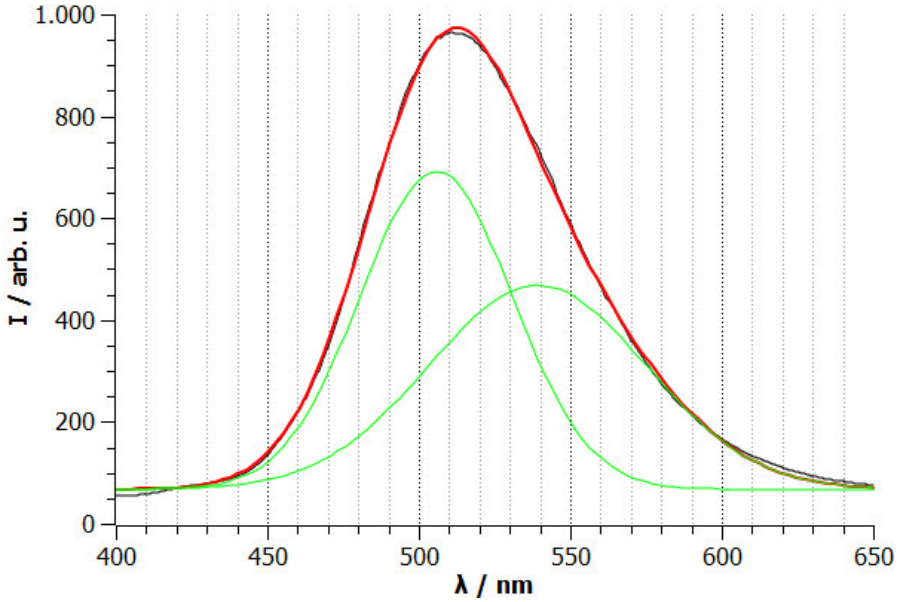

Figure 4.26.: Emission bands of the two Eu sites: the green bands show the emission bands of the Eu ions sitting on the two different Sr sites. The red band corresponds to the sum of both Eu emissions.

consist of about 20% oxygen which acts as oxidizing agent. Hence no further reactants are needed. Different from the synthesis under reducing conditions there is an excess of oxygen in the atmosphere. The partial pressure is high enough to shift equation 4.6 to the left side.

The excitation spectra shows the band gap edge, a broad band around 246 nm and a small band at 395 nm The latter is probably the $^7F_0 \rightarrow ^5 L_6$ transition. The band at 246 nm contains several peaks. One of them describes a CT from the host material, or more precisely from an $2p_{O^{2-}}$ orbital, to the 4f of the Eu^{3+} which is consequently reduced to Eu^{2+}. The Eu^{3+} energy state lays in the VB [26]. Therefore it can easily absorb an electron. It is the reverse process of the CT in the excitation spectra of the samples with Eu^{2+}. The remaining bands could be due to residual Eu^{2+} or due to artefacts.

The emission spectrum shows no Eu^{2+} band but the well known transitions of Eu^{3+}. The latter are $4f \rightarrow 4f$ transitions. Therefore they have much smaller transition dipole moments than the interconfiguration transition. Nevertheless they dominate the spectrum. It shows all transitions from the $^5D_0$ state to the ^7F_J states with their corresponding CF splitting. The only transitions that can not be seen are those to the

$^7F_5$ and $^7F_6$ ground states. They are too low in intensity and should occur at longer wavelengths. As expected, the emission spectra do not reveal the two different sites of Eu because $4f \rightarrow 4f$ transitions are not sensitive to the CF. Again no Eu2 related bands were observed because of the sintering step.

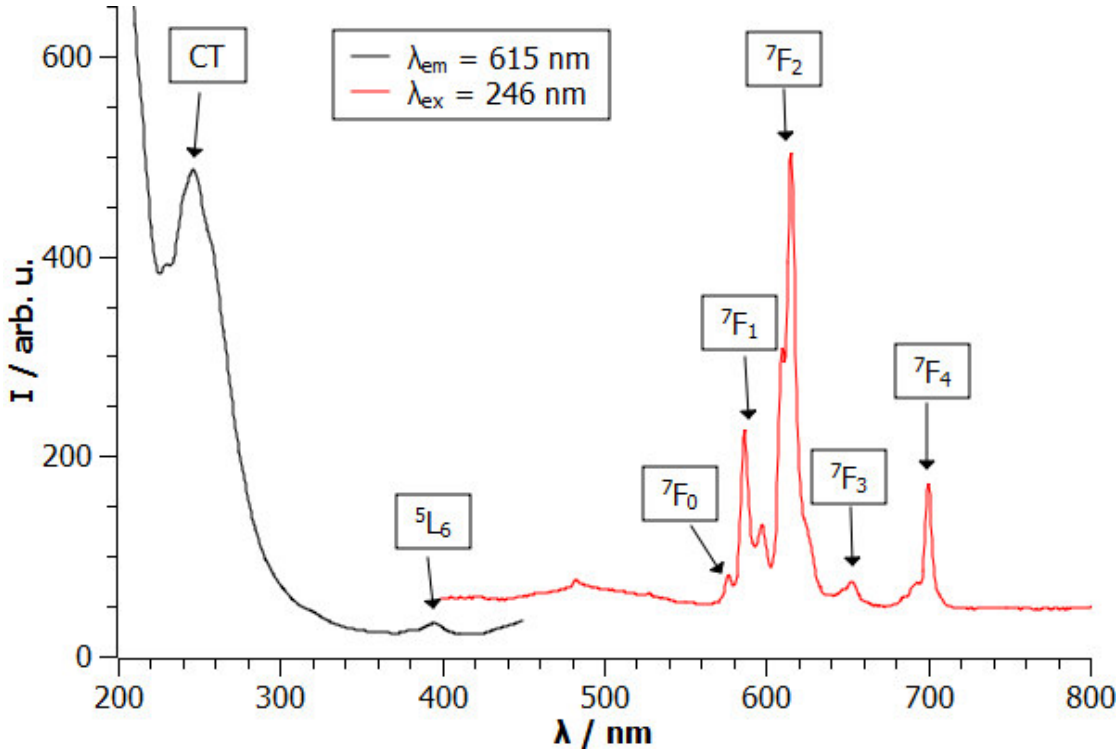

Figure 4.27.: Emission / excitation spectra of sintered SA,Eu^{3+}(1)

Em. slit: 3 nm	Voltage: 775 nm	Delay: 0 ms

Figure 4.28 shows the spectrum of sample SA,Dy(1). The excitation spectrum features the edge of the band gap. The shoulders in the band gap absorption edge can be attributed to the artefacts of the sample holder. An excitation spectrum with the emitting wavelength of 482 nm did not provide new knowledge and is therefore not shown.

The emission after excitation with a wavelength of 230 nm reveals only two bands that originate from the sample. They can be identified as the $^4F_{9/2} \rightarrow^6 H_{13/2}$ transition at 482 nm and the $^4F_{9/2} \rightarrow^6 H_{15/2}$ transition at 575 nm. The latter overlaps with an emission of the sample holder. However, there are two arguments that give evidence that there is hidden a band of Dy. First the shape of the band. It is asymmetric. This

is because the Dy and sample holder emissions have slightly different wavelengths - namely 482 and 484 nm. Second the life time that is much shorter for the emissions of the sample holder. Therefore the emission spectra at a delay time of 0.1 ms shows only the emissions of Dy with nearly the same intensities (figure 4.29). Both emission bands of Dy are broad because the target states are highly degenerate.

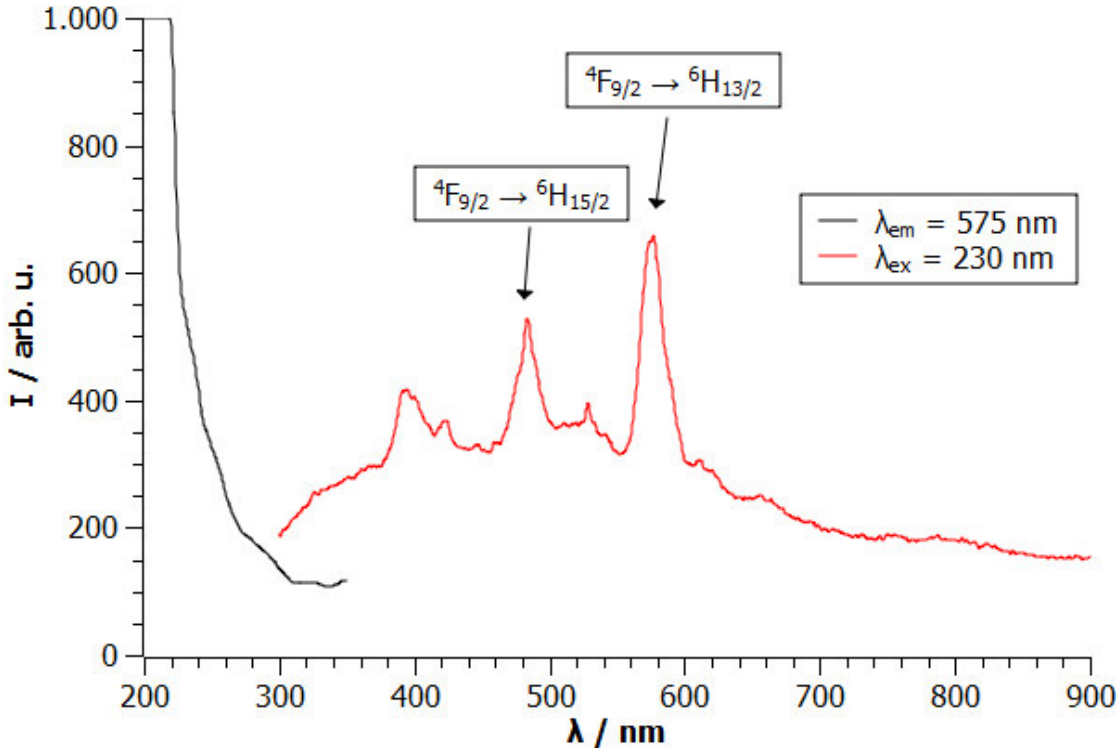

Figure 4.28.: Emission / excitation spectra sintered of SA,Dy(1)

Em. slit: 4 nm	Voltage: 900 nm	Delay: 0 ms

Nd3+ does not emit visible light - it emits in the NIR outside the range of the instrument used. Therefore no spectra were measured.

The Pr spectra can be seen in figure 4.30. Two different excitation spectra are shown because they feature different bands. Again the artefacts of the sample holder can be seen. The excitation spectra with the emitting wavelength of 303 nm shows one band at 233 nm. This transition cannot be assigned. The other excitation spectrum feature the $^3H_4 \rightarrow {}^3P_1$ transitions. It is quite low in intensity. The same applies for the corresponding emission spectra. Consequently, it was excited with a wavelength of 230 nm.

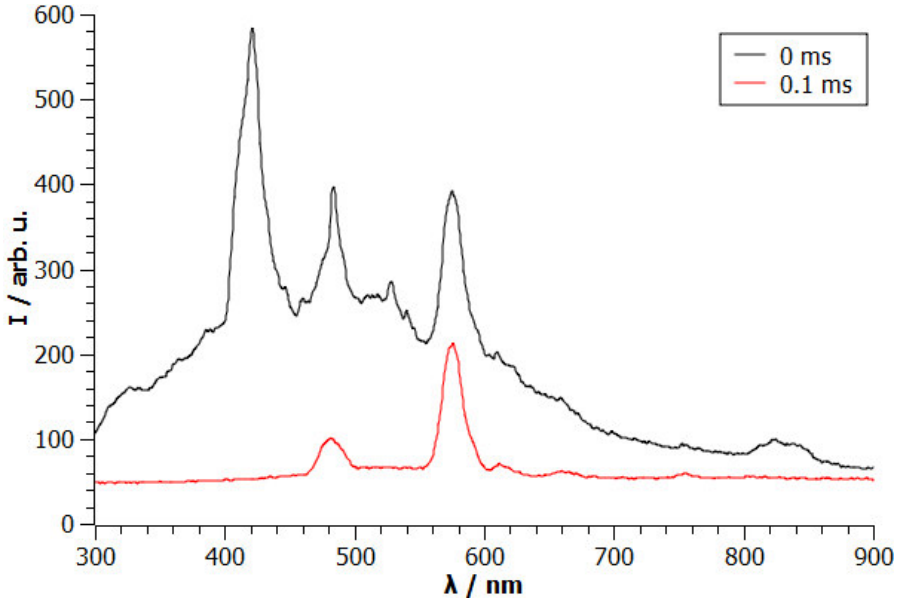

Figure 4.29.: Emission spectrum of SA,Dy(1): it is free of artifacts after 0.1 ms. The excitation wavelength was 230 nm.

Em. slit: 4 nm	Voltage: 900 nm	Delay: 0 / 0.1 ms

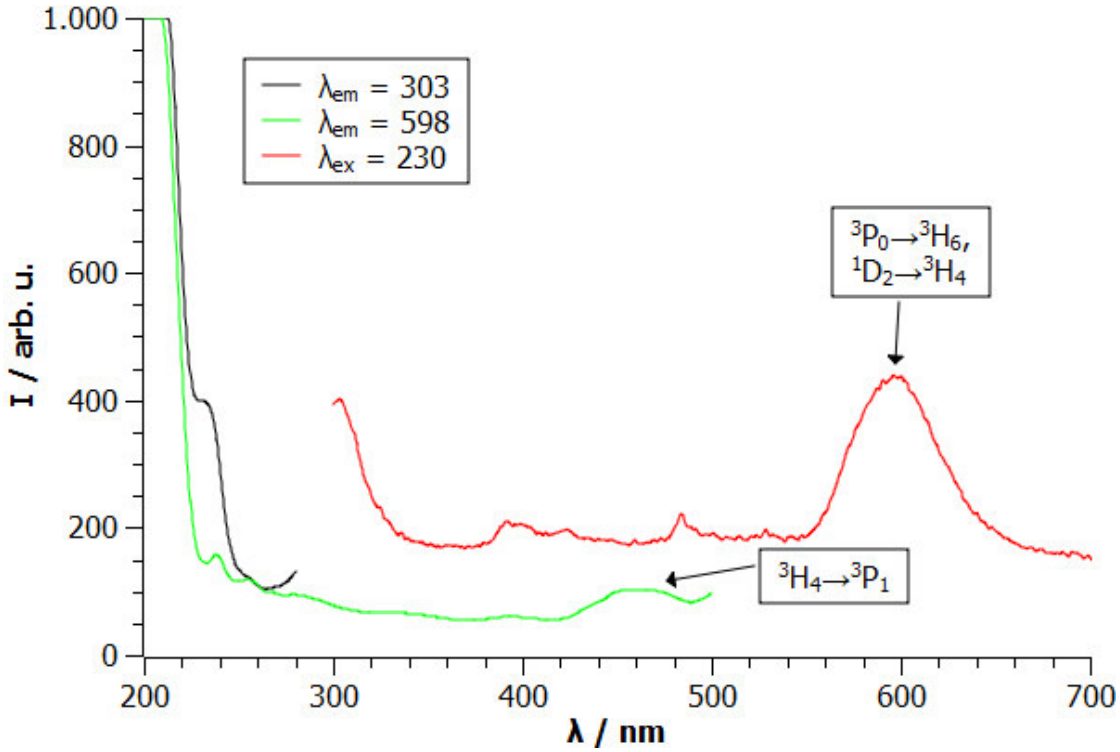

Figure 4.30.: Emission / excitation spectra of sintered SA,Pr(1)

Em. slit: 3 nm	Voltage: 900 nm	Delay: 0 ms

The emission spectrum shows two bands. One at 303 nm and one at 598 nm. The latter reveals the overlap of the $^3P_0 \rightarrow ^3 H_6$ and $^1D_2 \rightarrow ^3 H_4$ transition. This explains why there is only one broad band. In addition the splitting of the degenerate final states is not resolved. The band around 303 nm is not fully plotted because of the instrument's cut off filter. The corresponding excitation band is at a wavelength of 233 nm and cannot be allotted to a transition. The emission spectrum with this wavelength is not shown because it is almost identical with the spectrum of 230 nm. Moreover it even promotes the emissions of the sample holder because of the near 238 nm excitation band. Therefore figure 4.30 shows only the emission spectra of 230 nm. Similar to the excitation band the emission band of 303 nm can not be assigned to a transition. Probably it is a IC transition. However, such bands are usually very broad. Hence it is unlikely that the bands at 233 and 303 nm are IC transitions.

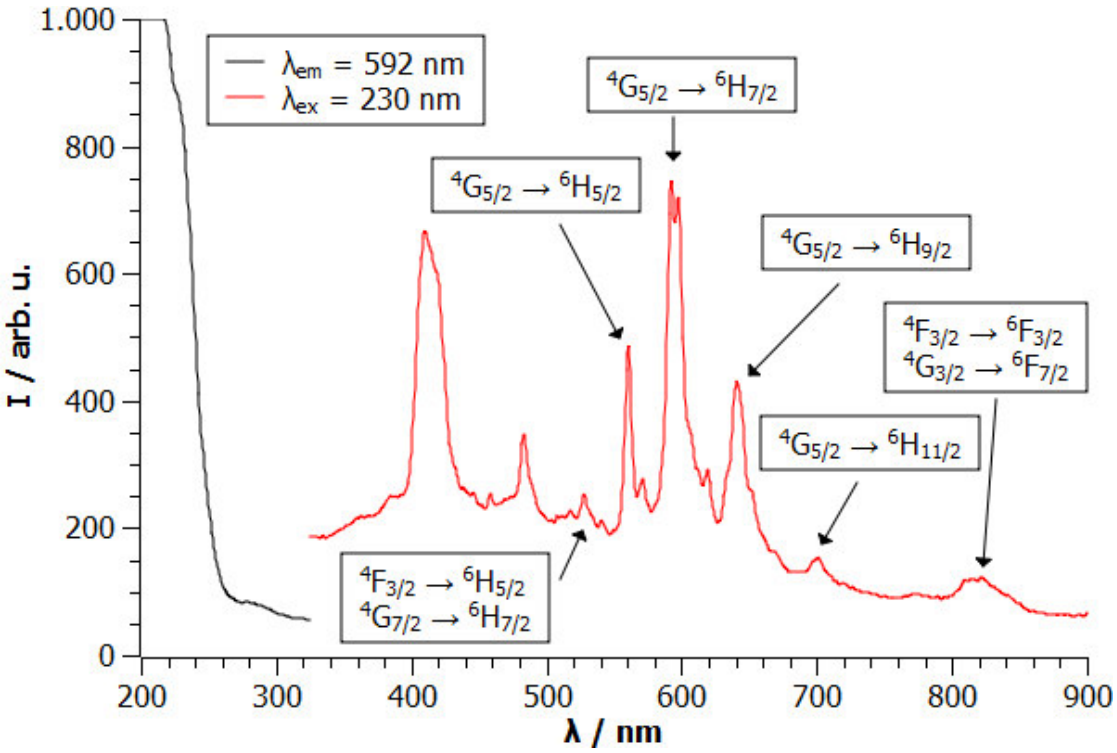

Figure 4.31.: Emission / excitation spectra of sintered SA,Sm(1)

Em. slit: 3 nm	Voltage: 900 nm	Delay: 0 ms

The emission/excitation spectra of sample SA,Sm(1) is shown in figure 4.31. The excitation spectra show the band gap edge with an shoulder that originates from the

sample holder. Moreover there is one flat band at 280 nm with low intensity. This band could be the CT from the VB to Sm^{3+}. The energy level of Sm^{2+} is said to be 2 eV under the CB and therefore 4.5 eV over the VB. In addition Sm^{2+} is a stable ion. However, the literature is not consistent in regard to the positions of the RE states within the band gap.

The emission spectrum was obtained by exciting with a wavelength of 230 nm. It is nearly free of artefacts and shows all $^4G_{5/2} \rightarrow ^6 H_J$ transitions with values of J from 5/2 to 13/2. Hence only one RS multiplet is not observed.

4.3. $SrAl_2O_4$:Eu,Dy – Eu and Dy doped $SrAl_2O_4$

4.3.1. Optical Characterisation with the UV Lamp

Table 4.4.: The singly doped samples under the UV lamp. The strength are values relative to the sintered sample SA,Eu^{2+}(1) under the wavelength of 365 nm. 0 means that no luminescence was observed. The values in brackets in the column of *365 nm* describe the strength of the afterglow after a half minute. A (-) in the column *duration* means that the glow vanished instantaneously. An (i) means that the afterglow did not completely disappear for the time it was observed (at least for 15 minutes).

		365 nm			254 nm		
Sample		Colour	Strength	Duration	Colour	Strength	Duration
SA,Eu,Dy(0.5;0.25)	unsint.	cyan	2	2 s	red	1	-
	sint.	green	3 (1)	(i)	green	3	(i)
SA,Eu,Dy(0.5;0.5)	unsint.	cyan	2	2 s	red	1	-
	sint.	green	3 (1)	(i)	green	3	(i)
SA,Eu,Dy(0.5;1)	unsint.	cyan	1	2 s	red	1	-
	sint.	green	3 (1)	(i)	green	3	(i)
SA,Eu,Dy(1;0.5)	unsint.	cyan	2	1 s	-	0	-
	sint.	green	4 (0)	15 s	green	3	15 s
SA,Eu,Dy(1;1)	unsint.	green	1	2 s	-	0	-
	sint.	green	3 (1)	(i)	green	3	(i)
SA,Eu,Dy(1;2)	unsint.	green	1	2 s	red	1	-
	sint.	green	3 (1)	(i)	green	3	(i)

The as-prepared foam of the solution combustion method showed again an inhomogeneous glow-behaviour. The duration of the afterglow depends on the composition and lasts at most only some seconds. However, the afterglow for the sintered samples was extended tremendously. The process was the same for all samples. They glowed greenish under the UV lamp. After the lamp was turned off the luminescence faded slowly. For instance SA,Eu,Dy(1,1) showed a persisting luminescence that lasted as long as it was observed. These two samples seems to glow more intense than all other samples. All results can be found in Tabel 4.4.

4.3.2. Optical Characterisation with the Fluorescence Spectrometer

The excitation/emission spectra of the unsintered samples showed the same three luminescence centres Eu1, Eu2 and Eu3 that were observed in the unsintered sample SA,Eu(1) too.

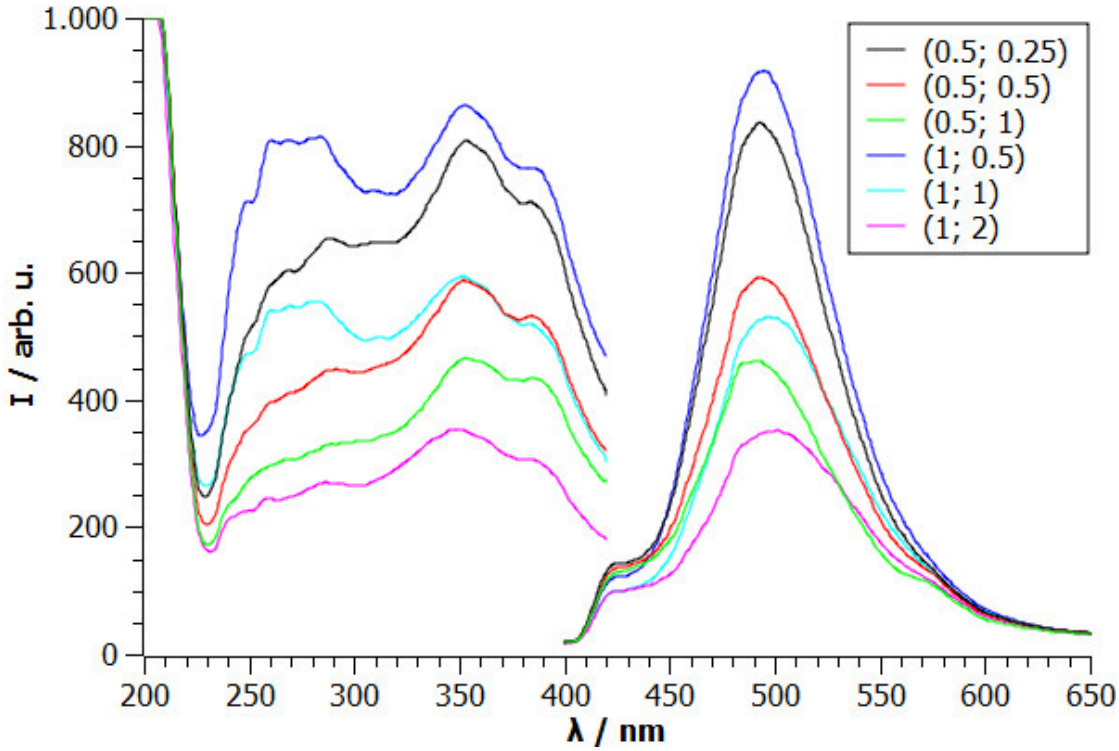

Figure 4.32.: Emission / excitation spectra of unsintered SA,Eu,Dy(x,y) with λ_{em} equals 493 nm and λ_{ex} equals 354 nm (= Eu1).

Em. slit: 5 nm	Voltage: 750 nm	Delay: 0

The spectra of Eu1 show barely differences from the unsintered sample of SA,Eu(1) (figure 4.32). The band position and shape is almost the same. Again there is no significant difference between an excitation at 250 nm and 330 nm except for the intensity of the resulting emission spectrum. The spectra reveal two trends. First, samples with an Eu concentration of 1% are generally more intense than samples with Eu concentrations of 0.5% and the same Eu-Dy ratio. Second, the higher the Dy concentration the lower the intensity. Both trends merge into each other.

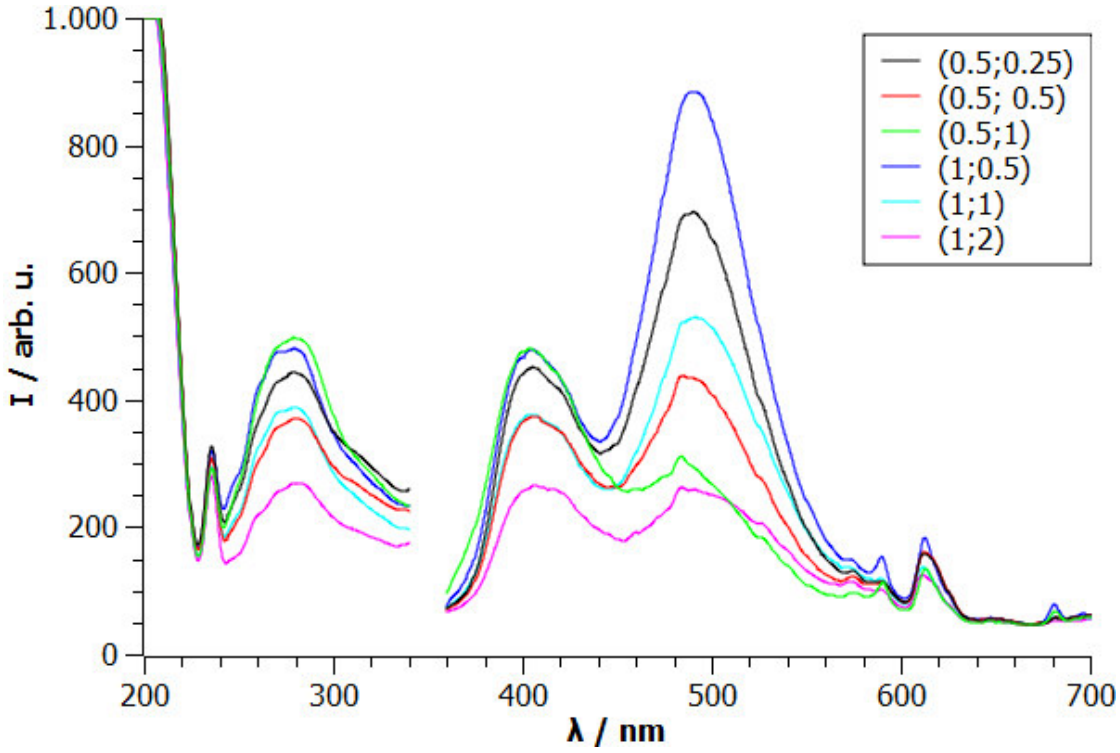

Figure 4.33.: Emission / excitation spectra of unsintered SA,Eu,Dy(x,y) with λ_{em} equals 404 nm and λ_{ex} equals 281 nm (= Eu2).

Em. slit: 5 nm	Voltage: 750 nm	Delay: 0 ms

The spectra of Eu2 show an interesting result (figure 4.33). A band at 281 nm emerges. Furthermore the intensity of the two bands 404 nm and 492 nm strongly depend on the Dy concentration. Both follow the trend mentioned above but the Eu1 band is stronger affected than the Eu2 band. In some samples it is even lower in intensity than the Eu2 band. This can be explained by the additional trivalent Dy that enhances the formation of Sr vacancies and therefore the concentration of Sr that can start an

alternative reaction. However, this conclusion is speculative. No further experiments were carried out and no source of reference was found explaining this phenomenon.

The same applies for the spectra of Eu3 (figure 4.34). Its band is not as strongly affected than the band of Eu1. Moreover, the excitation band is more intense compared with the singly doped sample.

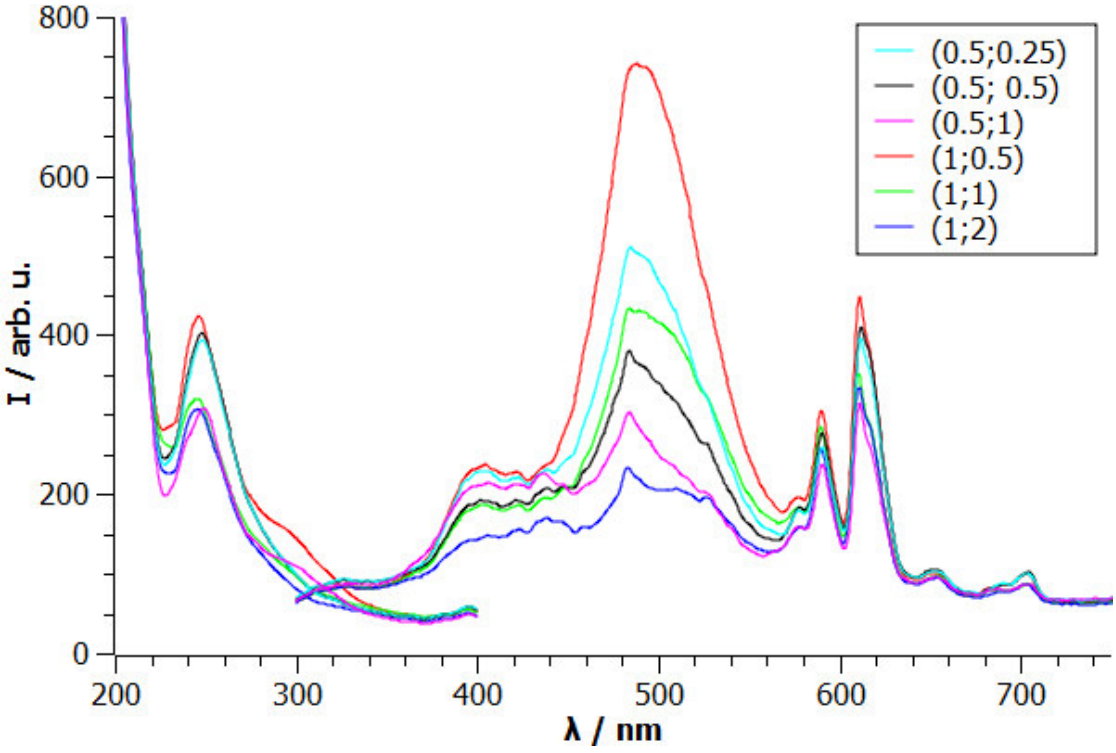

Figure 4.34.: Emission / excitation spectra of unsintered SA,Eu,Dy(x,y) with λ_{em} equals 612 nm and λ_{ex} equals 243 nm (= Eu3).

Em. slit: 5 nm	Voltage: 750 nm	Delay: 0 ms

All in all the addition of Dy barely influences the shape and position but remarkably influences the intensity of the bands of the singly doped sample SA,Eu(1). However, as already mentioned earlier solution combustion is a preparation method that is difficult to control. The crystallinity and purity of the unsintered preparations are still limited. This can lead to differences in the shape, position and also intensity. Hence the samples were sintered to confirm all observations mentioned before.

Figure 4.35 compares the excitation/emission spectrum of the sintered samples SA,Eu(1) with the spectra of SA,Eu,Dy(1;0.5). The latter was chosen because it has

about the same intensity. Some of the differences mentioned above can be still observed. Both excitation spectra show the two broad CT and IC transitions. However, different from sample SA,Eu(1), where the band at 255 nm is more intense than the band at 330 nm, they have approximately the same intensity in sample SA,Eu,Dy(1;0.5). In addition the former band is narrower. Nevertheless the positions are the same for both samples. This implies that Dy does not influence the CF or the symmetry of the host material.

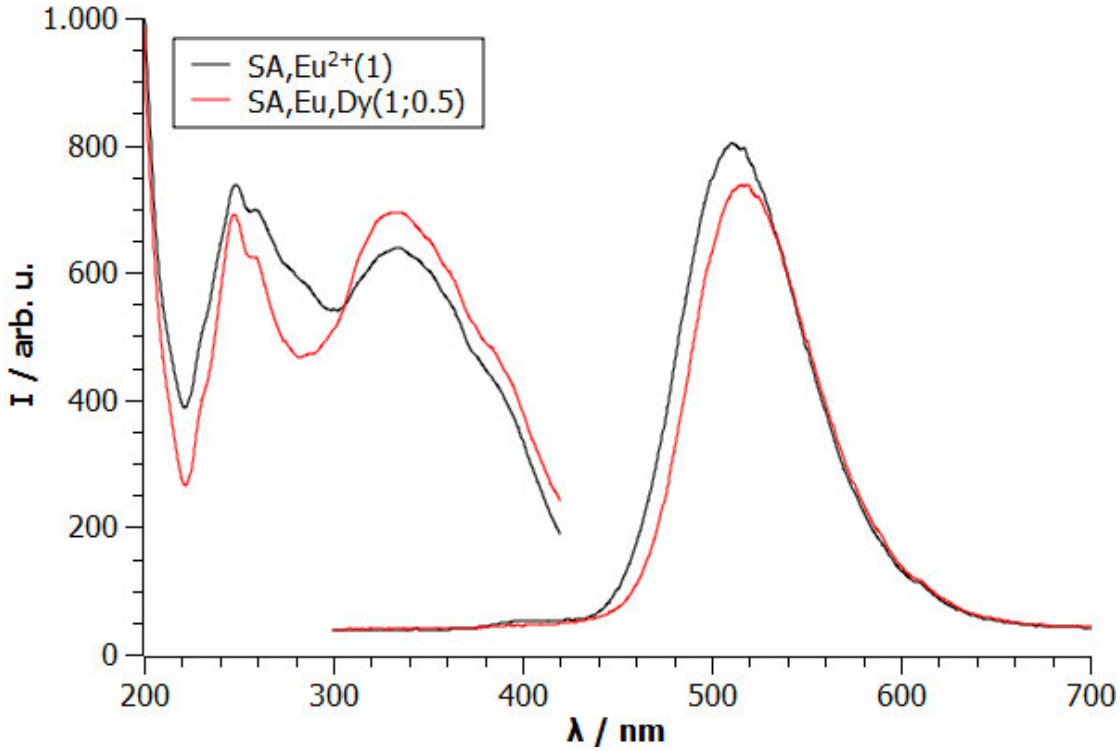

Figure 4.35.: Comparison of SA,Eu^{2+}(1) with SA,Eu,Dy(1;0.5) with λ_{em} equals 512 / 517 nm and λ_{ex} equals 248 nm (= Eu1).

Em. slit: 3 nm	Voltage: 700 nm	Delay: 0 ms

However, this does not apply for the emission spectra. Both spectra show the same $4f^6 5d^1 \rightarrow 4f^7$ transition but the position is different. The band moves from 512 nm for SA,Eu(1) to 517 nm for the co-doped sample. There are two different possible explanations. Perhaps the shift occurs because of the two different occupied Sr sites by Eu. Dy could influence the distribution of the Eu on these two sites and the whole band therefore moves to higher wavelengths. However, there is no sensible explanation why Dy should have an effect on the formation of the crystal. Another possible explanation

is that Dy changes the CF. It has a higher charge than Sr and is therefore able to stabilize the negatively charged oxygen ligands better. Therefore the d-orbitals that are highly sensitive to the CF are lowered in energy. As a result the transition band emerges at longer wavelengths. On the other hand, the excitation spectrum is not affected by this stabilisation. Perhaps there is only a stabilisation of the d orbitals during the trapping mechanism of the persistent luminescence. This will be further discussed in section 4.4.4.

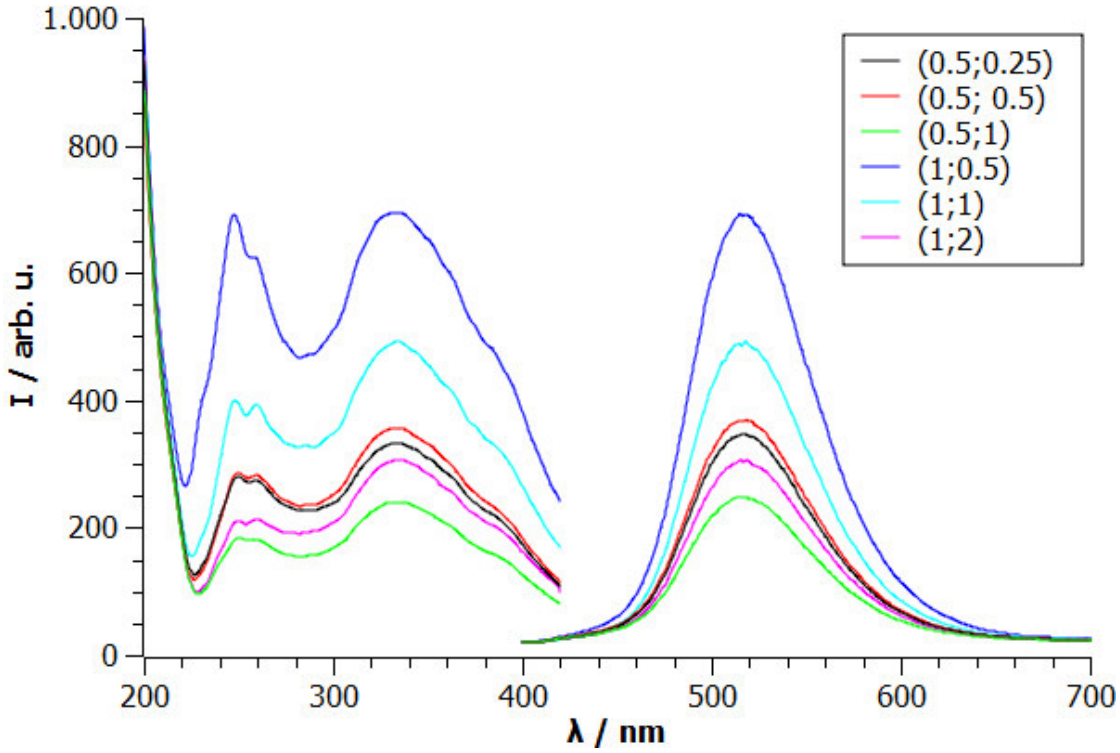

Figure 4.36.: Emission / excitation spectra of SA,Eu,Dy(x;y) with λ_{em} equals 517 nm and λ_{ex} 335 nm.

Em. slit: 3 nm	Voltage: 700 nm	Delay: 0 ms

Figure 4.36 shows the excitation and emission spectra for all sintered SA,Eu,Dy(x;y) samples. All spectra resemble that of sample SA,Eu(1). No Dy bands are observed because they are too low in intensity. The sintered samples confirm the trend discussed before. However, there is one exception of these rules. Sample SA,Eu,Dy(0.5;0.5) shows a higher intensity than sample SA,Eu,Dy(0.5;0.25). Actually, one would expect an inverted behaviour. However, the experimental result is based on just a single sample. So no

further samples of the same composition were prepared. Hence this missing agreement based on only one single sample can be ignored.

The decay curves with the excitation of wavelengths 335 nm and 248 nm lead to the same results referring to the duration of the afterglow. It was decided to choose the excitation wavelength of 335 nm because the corresponding curves have higher intensities than those of the excitation with a wavelength of 248 nm.

The short time range decay curves were compared with the singly doped SA,Eu(1) sample. For this purpose the decay parameters were modified as mentioned in the section before. The constants y_0 and A of equation 4.9 were combined to

$$\frac{y_0 + A}{1000} = \alpha_{STR} \tag{4.10}$$

Here α_{STR} is a measure for the initial intensity. The factor 1000 was used to get constants of convenient numerical value. The decay time τ was modified to

$$\frac{A}{\tau} = k_{STR} \tag{4.11}$$

Here k_{STR} yields the initial slope (t equals 0). The higher k_{STR} the faster is the decay. It can be used to discuss the decay behaviour.

The short time range decay curves and their coefficients are shown in figure 4.37 and table 4.5. All curves decrease strongly within the first half hundredth of a second. Then they flatten out and stay constant at a level of approximately one third of the initial signal. It becomes obvious that the curves again coincide with the trend mentioned before. Samples with high Eu and low Dy concentrations show generally higher intensities. However, this trend applies only for initial delay-time values. Some cross overs occur at higher delay times. For instance the curves of sample SA,Eu,Dy(1;0.5) and SA,Eu,Dy(0.5;0.25) decrease faster than the curves of samples SA,Eu,Dy(1;1) and SA,Eu,Dy(1;2) respectively. The singly doped sample even drops under all co-doped samples. Therefore, it is not the individual Eu and Dy concentration that determines the decay behaviour.

It is more the Eu-Dy ratio as can be seen from the normalized decay curves (fig-

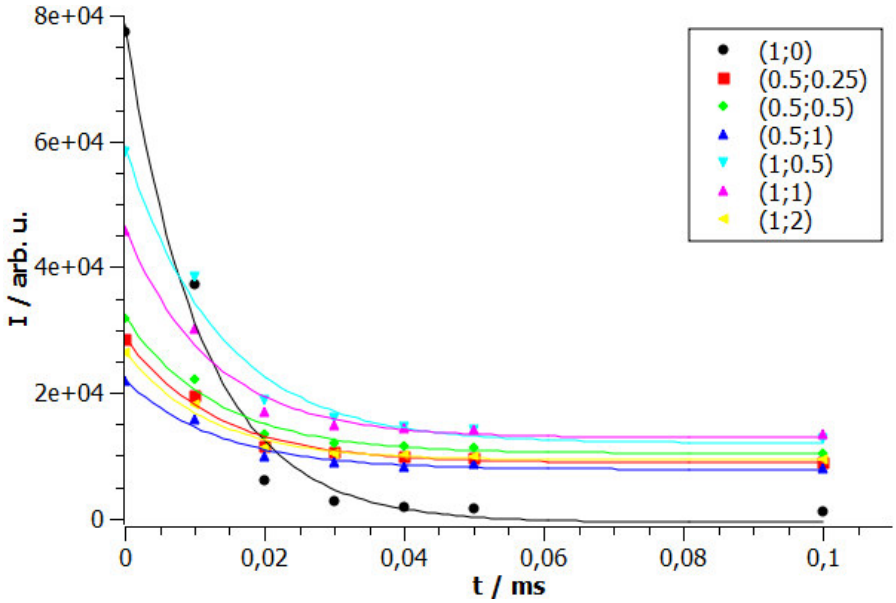

Figure 4.37.: Decay curves of the short time range of SA,Eu,Dy(x;y). The corresponding decay constants are given in table 4.5

Table 4.5.: The decay constants of the short time range of SA,Eu,Dy(x;y).

Sample	y_0	A	τ [μs]	α_{STR}	k_{STR} [ns^{-1}]
SA,Eu^{2+}(1)	−626	79,152	11.1	78.5	7.15
SA,Eu,Dy(0.5;0.25)	8,845	20.079	12.9	28.9	1.56
SA,Eu,Dy(0.5;0.5)	10,343	21,878	13.1	32.2	1.68
SA,Eu,Dy(0.5;1)	7,785	14,330	13.3	22.1	1.08
SA,Eu,Dy(1;0.5)	11,980	47,332	13.4	59.3	3.53
SA,Eu,Dy(1;1)	12,842	33,515	12.2	46.4	2.74
SA,Eu,Dy(1;2)	9,277	17,403	12.0	26.7	1.45

ure 4.38). This plot is free of information about the initial intensity. Hence it perfectly reveals the decay behaviour. The trend is explicit. The higher the Eu-Dy ratio the faster the decay. Sample SA,Eu(1) has by far the fastest decline.

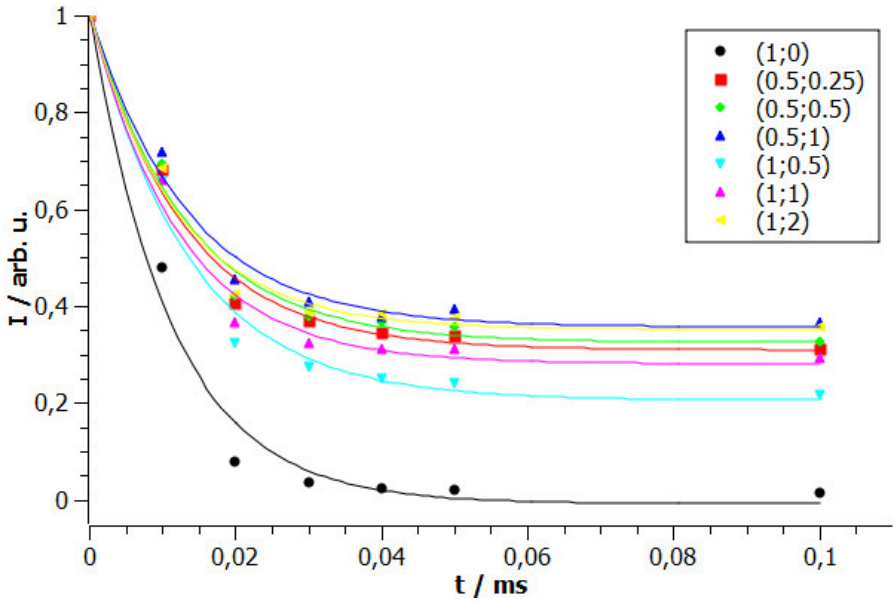

Figure 4.38.: Normalised decay curves of the short time range of SA,Eu,Dy(x;y).

Both trends are well confirmed by the parameters α_{STR} and k_{STR} of the exponential fitting curves (figure 4.39). It can be seen that the samples with high Eu and low Dy concentration have the highest α_{STR}. Sample SA,Eu,Dy(0.5;1) has the lowest whereas sample SA,Eu,Dy(1;0.5) has the highest value. The difference between the highest and the lowest value is 70%. The trend is that those curves with high Eu and low Dy concentration are high in intensity. This makes sense because α_{STR} only determines the intensity and not the slope of the function. The decay times, however, do not show an obvious trend. For α_{STR} applies the higher the Eu and the lower the Dy concentration the larger the parameter. k_{STR}, however, depends mainly on the Eu-Dy ratio. In addition all samples with an Eu concentration of 1 have larger k_{STR} and therefore decay faster. This, however, is perhaps a side effect that originates in A that was used to calculate k_{STR}.

More information will be obtained from the long-time observation that covers a much longer time range of 15 minutes.

The decay curves of the long time range can be seen in figure 4.40. They were all

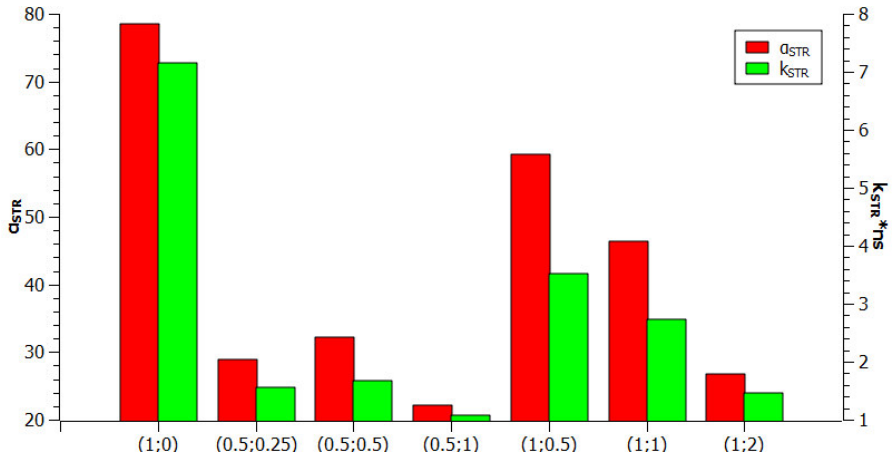

Figure 4.39.: Decay constants of the short time range of SA,Eu,Dy(x;y).

fitted with a double exponential decay with an time range from the first measurable decay of approximately 8 s to 300 s. The reasons for choosing a double exponential decay are different from the short time range. Neither the pre-factors nor the decay times were the same for the higher order curves. The correlation coefficient R^2, however, considerably changed from first to second order but stayed constant for the next higher order. Therefore, the used fit for the decay curves was of second order. This leads to a further modification of α_{STR} and k_{STR}

$$y_0 + A_1 + A_2 = \alpha_{LTR} \tag{4.12}$$

$$\frac{A_1}{\tau_1} + \frac{A_2}{\tau_2} = k_{LTR} \tag{4.13}$$

The decay constants can be found in table 4.6.

All curves lose about 70% of their initial intensity within the first half minute. In the next half minute they decrease for about further 40%. Then the curves flatten out. Considerable differences can only be found within the first minutes. Then the curves merge into each other. The shape of the curves resembles that one of the short time range. However, this does not mean that there are two fast decaying steps and two plateaus. The time scale of the short time range are stretched by a factor of about 10,000 compared to the scale of the long time range.

However, the order of the curves in the long time range according to the intensity is

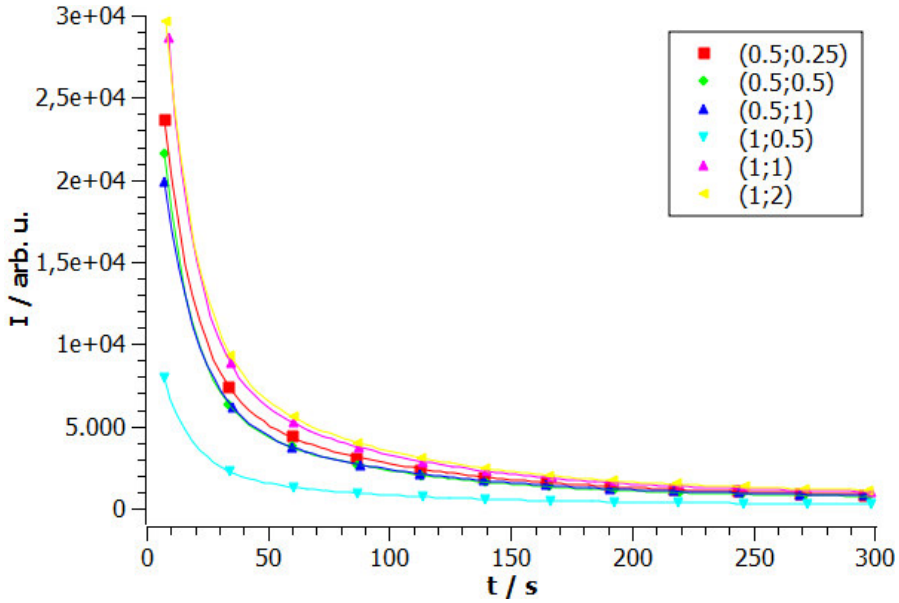

Figure 4.40.: Decay curves of the long time range of SA,Eu,Dy(x;y). The corresponding decay constants are given in table 4.6

Table 4.6.: The decay constants of the long time range of SA,Eu,Dy(x;y).

Sample	y_0	A_1	A_2	τ_1 [s]	τ_2 [s]	α_{LTR}	k_{LTR} [ms^{-1}]
SA,Eu,Dy(0.5;0.25)	728	7,442	29,198	75.6	12.5	37.4	2.44
SA,Eu,Dy(0.5;0.5)	636	6,675	27,997	72.3	11.7	35.3	2.48
SA,Eu,Dy(0.5;1)	670	6,089	24,207	77.6	13.2	31.0	1.91
SA,Eu,Dy(1;0.5)	229	2,287	10,309	72.3	11.8	12.8	0.90
SA,Eu,Dy(1;1)	855	9,270	42,207	74.1	11.7	52.3	3.75
SA,Eu,Dy(1;2)	926	9,610	38,616	75.5	12.3	49.2	3.26

different from the order at the end of the short time range. This reveals that the cross over of the curves must have continued in the time gap that is not accessible for the measurements. Sample SA,Eu,Dy(1;0.5) is now the lowest and sample SA,Eu,Dy(1;2) is together with sample SA,Eu,Dy(1;1) the highest in intensity. This could even be realized with the naked eye. Both samples were not the most intense in the decay curves of the short time range. Within the long time range, however, no crossing can be observed. This means that the decay behaviour will be similar or even equal.

The relative curves confirm this (figure 4.41). All curves are nearly congruent. This means that the luminescence for long delays does not depend on the decay time. It is more the intensity assigned from the time gap that will decide if an afterglow is intense or not. In other words if the luminescence is intense at the beginning of the long time range it will also stay intense at longer delays until it fades. Therefore a sample that shows an more intense afterglow at the beginning than an other sample will also glow more intense at longer delay. This effect will start from the very beginning because a human observer can not perceive the microscopic time scale of the short time range.

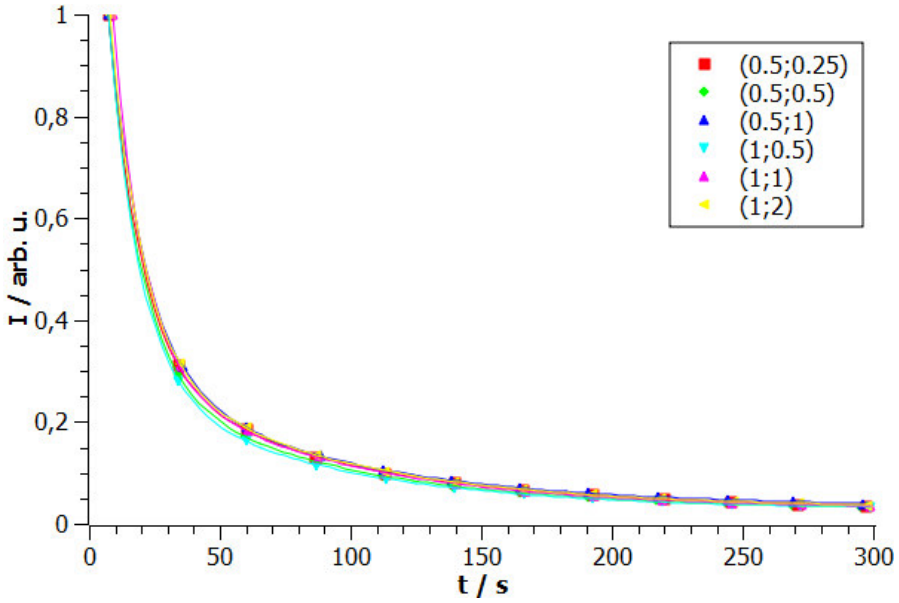

Figure 4.41.: Relative decay curves of the long time range of SA,Eu,Dy(x;y). The corresponding decay constants are given in table 4.6

The fitting constant α_{LTR} confirms this. The higher the Eu and the Dy the more intense the afterglow. However, the effects of Eu and Dy to the intensity of the afterglow

are different. Eu arranges for high intensities from the beginning. It is like a storage of intensity that will be consumed during the decay. The higher the concentration of Eu the larger the storage. Dy, however, does not directly contribute to the size of the storage. It decreases the decay and therefore cares for a slow consumption of the storage. This explains why SA,Eu,Dy(1;0.5) has by far the lowest initial intensity α_{LTR} in the long time range. Although it has a high concentration of Eu it decreases fastest. There is a lack of Dy and the storage is consumed fast. The opposite applies for samples SA,Eu,Dy(1;1) and SA,Eu,Dy(1;2). However, it can be seen that an excess of Dy does not lead to a more intense afterglow. This does not necessarily mean that sample SA,Eu,Dy(1;2) does not promote the afterglow better than SA,Eu,Dy(1;1) does. Compared to the initial time (t equals 0) the latter lost much more intensity than sample SA,Eu,Dy(1;2). This also coincides with the observations with the naked eye.

The k_{LTR} values, however, show no clear trend. The order for the samples with 0.5% is in agreement with the trend mentioned above. The other three samples with an Eu concentration of 1%, however, contradict the trend. Nevertheless, this contradiction can be neglected because of the following reason. As it can be seen from figure 4.41 there are hardly any differences between the decay behaviour. The values of k_{LTR}, however, depends on the constants A_1 , A_2, t_1 and t_2. The first two parameters yield information about the initial intensity that is higher for the samples with low Eu-Dy ratios and high concentrations of Eu. They vary considerably from sample to sample. The decay times, however, deviate comparatively little. Hence those samples with high A will lead to high k_{LTR} as it is shown in figure 4.42.

A comparison of k_{STR} with k_{LTR} show that the decrease of the short time range is about one million times faster than for the long time range. However, this is not observable on a microscopic time level.

As a conclusion of this chapter it was decided which doping concentrations of Eu and Dy yield the best luminescence properties. The focus was on two features: intense luminescence and long afterglow. Samples with intense luminescence are SA,Eu,Dy(1;0.5) and SA,Eu,Dy(1;1). The long afterglow is obtained with samples SA,Eu,Dy(1;1) and SA,Eu,Dy(1;2). As a result sample SA,Eu,Dy(1;1) performed best. Assuming that a similar result applies for RE other than Dy, the other co-doped samples were prepared

with 1% Eu and 1% RE.

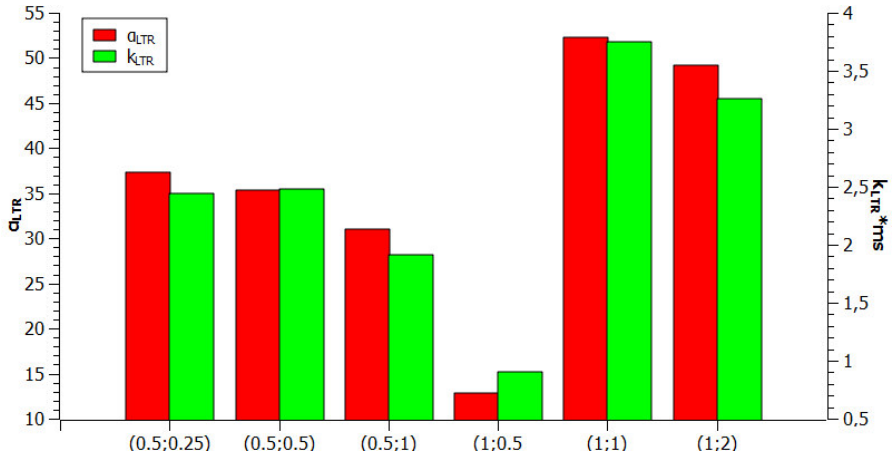

Figure 4.42.: Decay constants of the long time range of SA,Eu,Dy(x;y).

4.4. $SrAl_2O_4$:Eu,RE – Co-doped $SrAl_2O_4$

Although sample SA,Eu,Dy(1;1) was comprehensively discussed in the last chapter it will be included in the following discussion too. Thus the term "all samples" refers to samples SA,Eu,Nd(1;1), SA,Eu,Pr(1;1) and SA,Eu,Sm(1;1) but also SA,Eu,Dy(1;1).

4.4.1. Optical Characterisation with the UV Lamp

The results of the unsintered samples resemble those of the last sections. There was no long afterglow observed. All samples except SA,Eu,Sm(1;1) showed an afterglow that lasted only some seconds. The afterglow for the sintered samples, however, was extremely extended. The two samples SA,Eu,Dy(1;1) and SA,Eu,Nd(1;1) glowed as long as they were observed. Sample SA,Eu,Pr(1;1) faded within the first seconds after the lamp was turned off. Nevertheless it still seemed to glow, however, on scarcely perceivable level. The luminescence of sample SA,Eu,Sm(1;1) ceased immediately. These results are in agreement with the literature [13]. They are summed up in table 4.7.

Table 4.7.: The singly doped samples under the UV lamp. The strength are values relative to the sintered sample SA,Eu^{2+}(1) under the wavelength of 365 nm. 0 means that no luminescence was observed. The values in brackets in the column of *365 nm* describe the strength of the afterglow after a half minute. A (-) in the column *duration* means that the glow vanished instantaneously. An (i) means that the afterglow did not completely disappear for the time it was observed (at least for 15 minutes).

		365 nm			254 nm		
Sample		Colour	Strength	Duration	Colour	Strength	Duration
SA,Eu,Dy(1;1)	unsint.	green	1	2 s	-	0	-
	sint.	green	3 (1)	(i)	green	3	(i)
SA,Eu,Nd(1;1)	unsint.	cyan	1	1 s	-	0	-
	sint.	green	3 (1)	(i)	green	2	(i)
SA,Eu,Pr(1;1)	unsint.	cyan	1	1 s	-	0	-
	sint.	green	3 (0)	3 s	green	1	1 s
SA,Eu,Sm(1;1)	unsint.	green	1	-	red	1	-
	sint.	green	2 (0)	-	green	1	-

4.4.2. Optical Characterisation with the Fluorescence Spectrometer

The emission/excitation spectra of the co-doped samples can be seen in figure 4.43. The intensity considerably depends on the co-dopant. The order decreasing in intensity is Dy, Sm, Nd and Pr, where Dy has by far the highest intensity. No detailed description for this trend was found in the literature. There was, however, suggested that the co-dopants have different impact onto the quantum yield [41]. Some of the RE promote non-radiative transitions more than others. However, there was no explanation given why the RE, that have quite similar properties, have such tremendously different effects on the quantum yield.

A better comparison regard to band position and shape can be obtained by plotting the relative intensities. In figure 4.44 the spectra are normalised in respect to the $4f^6 5d^1 \rightarrow 4f^7$ emission band.

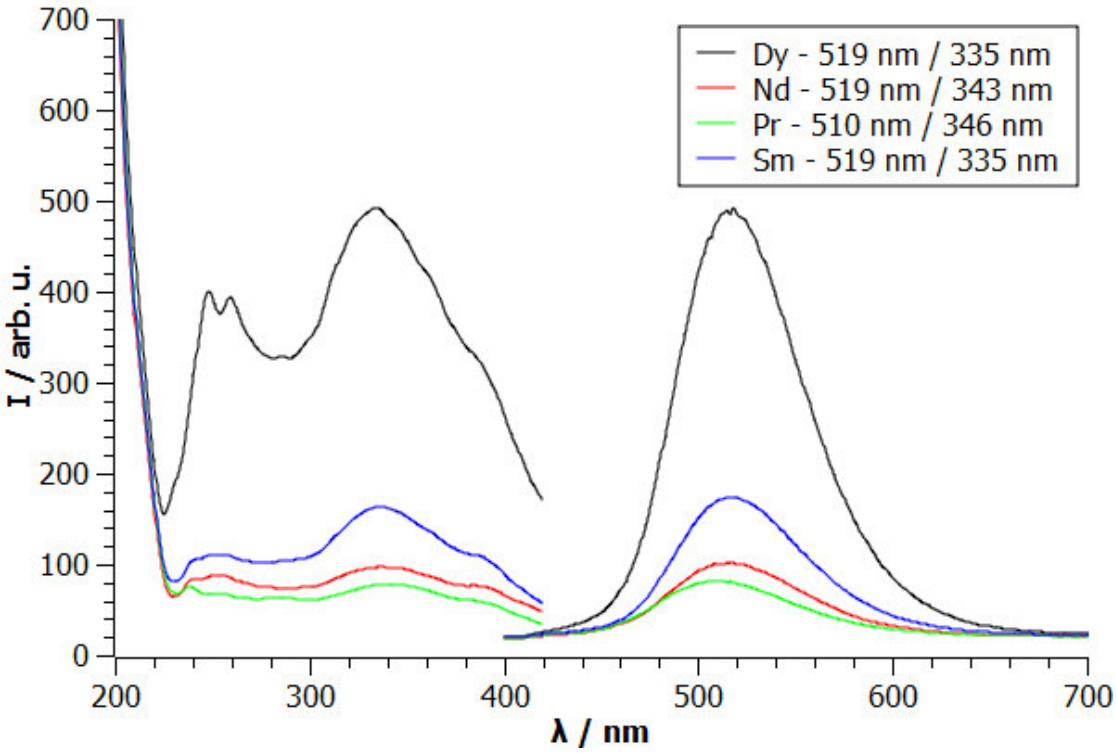

Figure 4.43.: Emission / excitation spectra of SA,Eu,RE(1;1).

Em. slit: 3 nm	Voltage: 700 nm	Delay: 0 ms

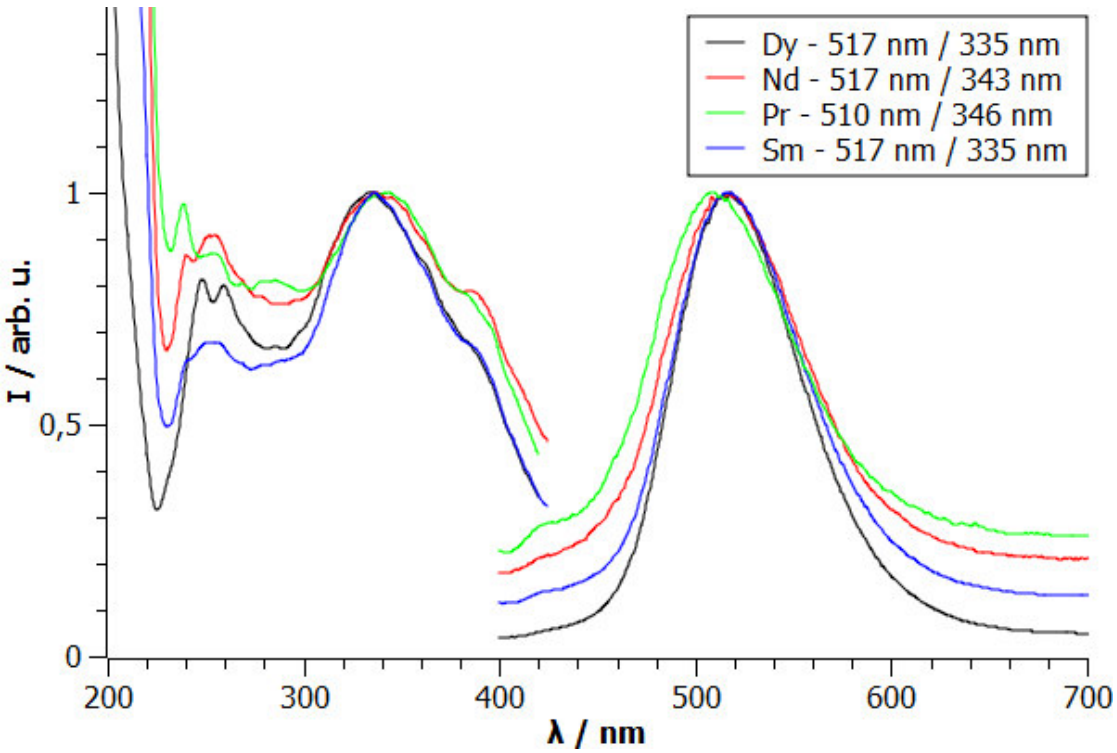

Figure 4.44.: Normalised emission / excitation spectra of SA,Eu,RE(1;1).

Em. slit: 3 nm	Voltage: 700 nm	Delay: 0 ms

All excitation spectra feature the broad bands of the CF splitting. The band at longer wavelengths around 340 nm is similar in shape for all samples. However, the position is slightly different. The samples SA,Eu,Dy(1;1) and SA,Eu,Sm(1;1) have their maximum at 335 nm. For sample SA,Eu,Nd(1;1) it is at 343 nm and for sample SA,Eu,Pr at 346 nm. The broad band features the $4f^7 \rightarrow 4f^6 5d^1$ transition that are CF split. Therefore its position highly depends on the CF. Thus the position can be influenced by the RE. They differ in their electron configuration, electron density and distribution and in their size. However, this concept can be questioned for two reasons. First the resulting effect should be only minimal because the differences between the RE are very small and second the RE needs to be close to Eu. This, however, is unlikely because of the small doping concentrations. The average Eu-RE distance would be too large to cause a significant impact to the CF. The band around 250 nm is different in shape but also in position for all sample. There are hardly any similarities. Only the samples SA,Eu,Nd(1;1) and SA,Eu,Sm(1;1) have a similar band. Both consist of two high peaks and some smaller ones at lower energy. The highest peak for both samples is at 253 nm and has a flat top. The band of sample SA,Eu,Dy(1;1) features also two high peaks but their position is different. They are located on both sides of the 253 nm peak mentioned above. Perhaps the latter revels also two peaks that cannot be resolved. The band of SA,Eu,Pr(1;1), however, has a completely different appearance. It highest band is at 239 nm. However, the band around 340 nm is the highest in the excitation spectrum for all samples.

Therefore all decay curves of the short time as well of the long time range were recorded with an excitation wavelength of 335, 343 and 346 nm respectively. As by the SA,Eu,Dy(x;y) samples before the measurement conditions for the long time range were again different from the short time range because of the much lower intensity of the afterglow.

The curves for the short time range are plotted in figure 4.45. They are compared with sample SA,Eu(1). All decay curves start from their initial intensity. However, the order changes with proceeding decay time. Because they all start from different levels of intensity it is difficult to draw a conclusion referring to the manner of decay. All curves plummet within the first hundredth ms and then stay constant at a low level. This low

level of afterglow can be used to classify the five curves. The samples SA,Eu,Dy(1;1) and SA,Eu,Nd(1;1) are both more intensive than the other three samples that are about the same in intensity. However, SA,Eu,Dy(1;1) started from a much higher intensity and therefore drops much faster than SA,Eu,Nd(1;1). The same applies for sample SA,Eu(1). It had the highest intensity initially but falls behind the Dy and Nd co-doped samples. It eventually stabilises at the same level as samples SA,Eu,Pr(1;1) and SA,Eu,Sm(1;1). However, the latter began from a much lower level and their lost of intensity is therefore small.

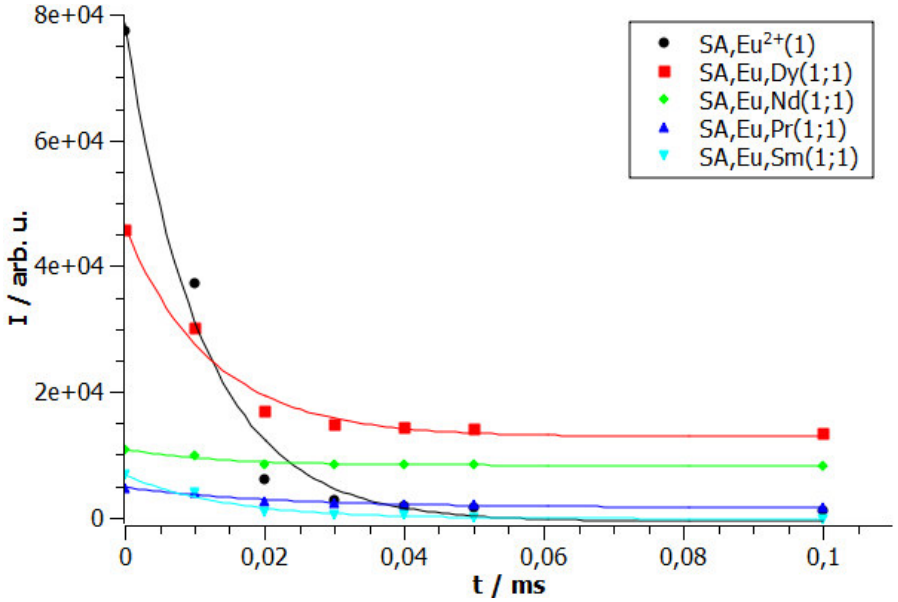

Figure 4.45.: Decay curves of the short time range of SA,Eu,RE(1;1). The corresponding decay constants are given in table 4.8

All these different decay behaviour can be well seen in the plot of the normalised decay curves (figure 4.46). Here it becomes obvious that SA,Eu,Nd(1;1) loses the least of the initial intensity. In numbers it is only about 35%. This causes the comparatively high intensity even after longer decay times of the short time range. The low initial intensity and the low loss of it compensate each other. The inverse applies for sample SA,Eu,Dy(1;1). It loses about 80% of the initial intensity. However, the high initial level and its high loss cancel each other in a way that it eventually ends up in the same order as sample SA,Eu,Nd(1;1). If their decay curves cross eventually or not will be figured out by the observation of the long time range. Nevertheless both promote the

afterglow of Eu in the short time range. Sample SA,Eu,Pr(1;1) shows an interesting decay behaviour. It had the lowest value for the absolute intensity but with a loss of 87% it ends up as the third highest curve at a decay time of 1 ms (see figure 4.47). However, it even lost less intensity for the first hundredth ms than sample SA,Eu,Dy(1;1). All in all it seems to promote the afterglow of Eu, at least in the short time range. Samples SA,Eu(1) and SA,Eu,Sm(1) lost all their intensity. Their emission spectra for the long decay times was very noisy and their integration sometimes even negative especially for sample SA,Eu,Sm(1;1). This means that Sm even downgrades the decay behaviour of Eu, assuming the results are trustable.

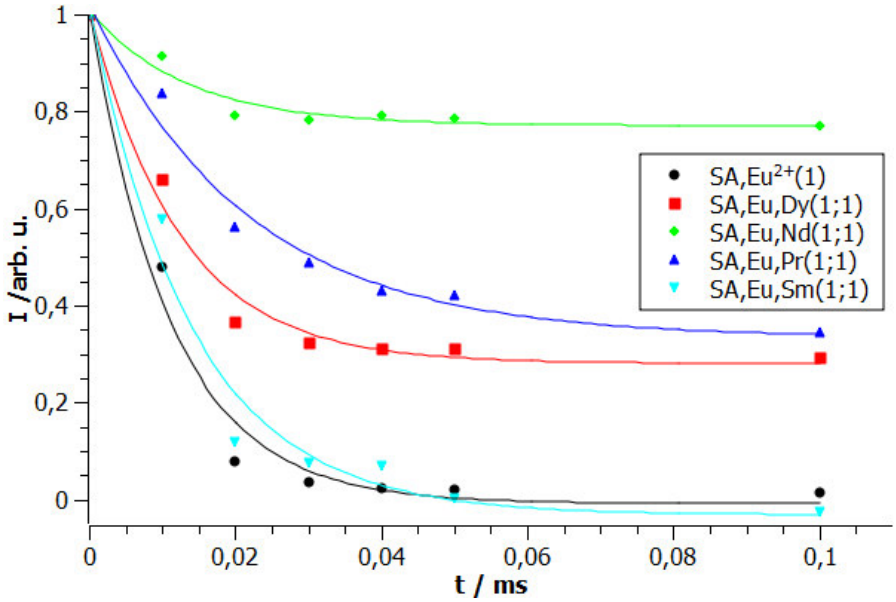

Figure 4.46.: Relative decay curves of the short time range of SA,Eu,RE(1;1).

The fitting constants as well as α_{STR} and k_{STR} are given in table 4.8 and a vivid comparison in figure 4.48. They confirm the results obtained from the decay curves.

The constant α_{STR} just reflects the emission intensities of the samples under illumination. It has the same order as the corresponding emission spectra (see figure 4.43).

The k_{STR} values vary considerably. Sample SA,Eu(1) has by far the fastest decay followed by sample SA,Eu,Dy(1;1). Consider, however, that k_{STR} is only a measure for the initial slope. The slope will stabilize for sample SA,Eu,Dy(1;1) but not for sample SA,Eu(1). Therefore the former will still have the most intense afterglow at the end of the short time range. The constants for SA,Eu,Nd(1;1), SA,Eu,Pr(1;1) and SA,Eu,Sm(1;1)

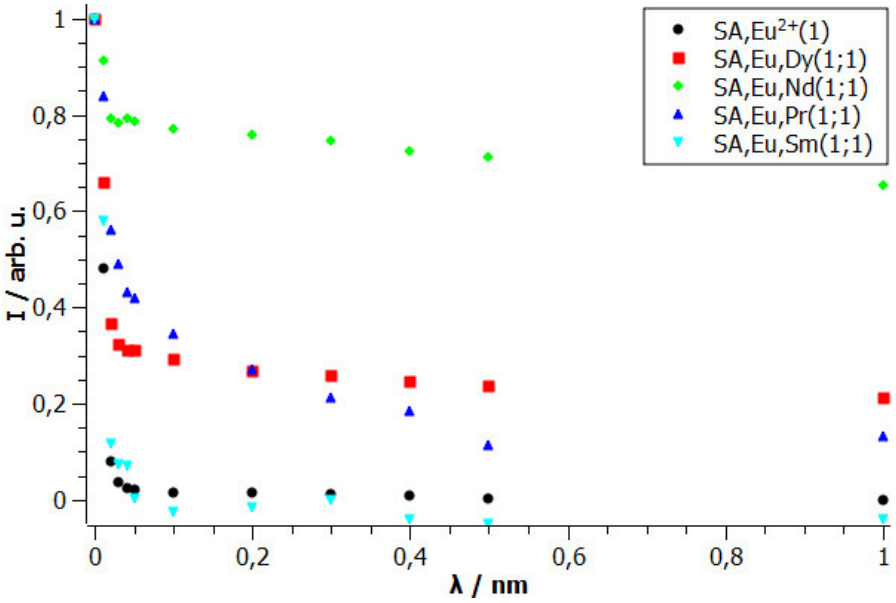

Figure 4.47.: Relative decay curves of the short time range of SA,Eu,RE(1;1) till 1 ms. The decay curves are not shown.

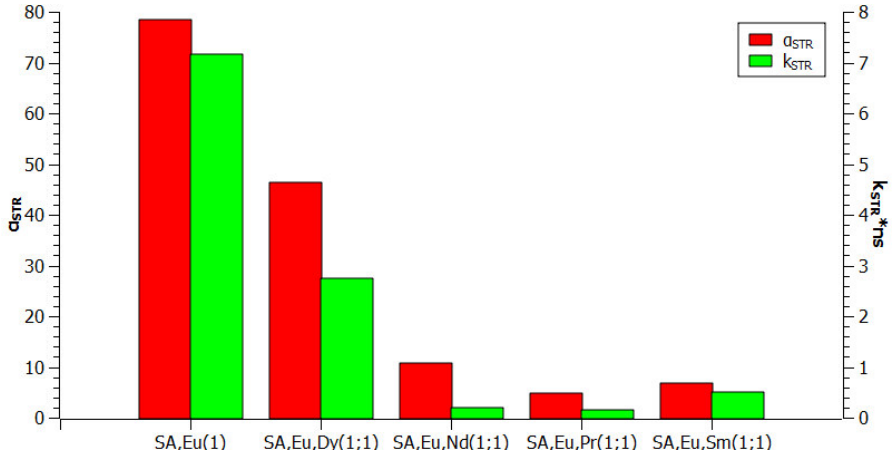

Figure 4.48.: Decay constants of the short time range of SA,Eu,RE(1;1).

Table 4.8.: The decay constants of the short time range of SA,Eu,RE(1;1).

Sample	y_0	A	τ [μs]	α_{STR}	k_{STR} [ns^{-1}]
SA,Eu^{2+}(1)	-626	79,152	11.1	78.5	7.15
SA,Eu,Dy(1;1)	12,842	33,515	12.2	46.4	2.74
SA,Eu,Nd(1;1)	8,275	2,536	13.4	10.8	0.19
SA,Eu,Pr(1;1)	1,577	3,256	21.6	4.8	0.15
SA,Eu,Sm(1;1)	-212	7,080	14.0	6.9	0.51

are low. This is because they already have a low intensity and therefore they can not lose a high amount of intensity right from the beginning. However, the decay is for all five samples tremendously fast as it can be seen from the constants.

Figure 4.49 shows the decay curves for the long time range of samples SA,Eu,Dy(1;1), SA,Eu,Nd(1;1) and SA,Eu,Pr(1;1). The recording of the curve for sample SA,Eu,Sm(1;1) was not possible because it did not show an afterglow in this time range.

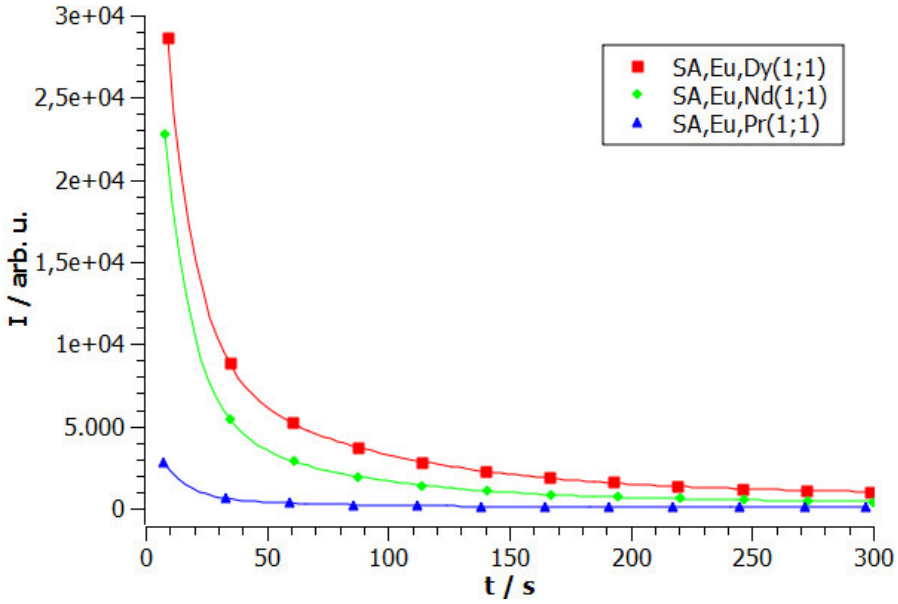

Figure 4.49.: Decay curves of the long time range of SA,Eu,RE(1;1). The corresponding decay constants are given in table 4.9

Samples SA,Eu,Dy(1;1) and SA,Eu,Nd(1;1) show still the most intense afterglow at the beginning of the long range decay. However, they fall faster within the first minute

than sample SA,Eu,Pr(1;1). Hence they all stay about constant and approach each other at decay times over 5 minutes. Furthermore the plot shows also that no crossing of these decay curves occurred in the time interval that was not accessible for the measurements. However, it seems that sample SA,Eu,Pr(1;1) lost less relative intensity than the Dy and Nd co-doped samples. Figure 4.50 shows that this is not true. It can be seen that the relative loss is nearly the same for all samples.

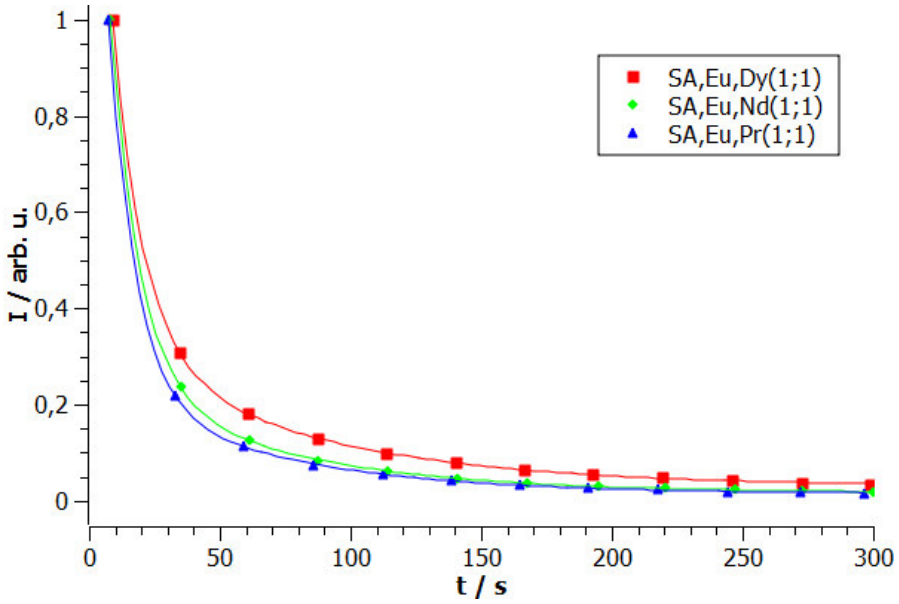

Figure 4.50.: Relative decay curves of the long time range of SA,Eu,RE(1;1).

This is in agreement with the initial intensity α_{LTR} and the initial slope k_{LTR} of the long time range (table 4.9 and figure 4.51).

Table 4.9.: The decay constants of the long time range of SA,Eu,RE(1;1).

Sample	y_0	A_1	A_2	τ_1 [s]	τ_2 [s]	α_{LTR}	k_{LTR} [ms^{-1}]
SA,Eu,Dy(1;1)	855	9,270	42,207	74.1	11.7	52.3	3.75
SA,Eu,Nd(1;1)	374	5,948	35,832	65.0	11.1	42.2	3.32
SA,Eu,Pr(1;1)	39	661	4,622	64.8	10.1	5,3	0.47

The initial intensity showed that no crossing occurred within the time gap.

The parameters k_{LTR}, however, are the highest for sample SA,Eu,Dy(1;1) and SA,Eu,Nd(1;1)

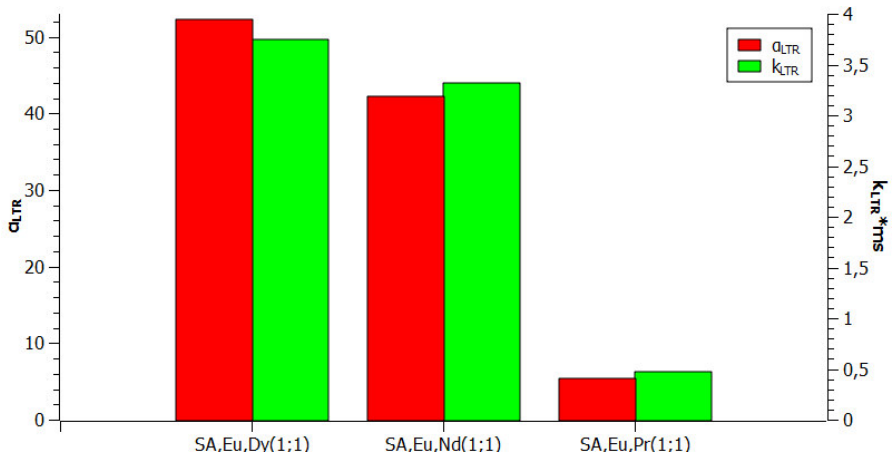

Figure 4.51.: Decay constants of the short time range of SA,Eu,RE(1;1).

although they are the most intense at all delay times. This is due to the dependency on constant A_1 and A_2. Similar to the curves of the short time range the intensity of SA,Eu,Pr(1;1) is already low at the beginning of the long time range and hence can not further decrease remarkably.

The constants also confirm the knowledge that was received from the sample series SA,Eu,Dy(x;y) (see section 4.3). Namely, that k_{LTR} does not influence the decay behaviour at high decay times a great deal. They only influence the short time range and the time gap but not the long time range. It is the initial intensity α_{LTR} that decides if an afterglow in this time range is bright or not. In other words if the intensities that were adopted from the short time range were high the resulting afterglow of the long time range will also be high. Hence Dy and Nd promote the afterglow considerably and Pr only moderate. This is in agreement with literature and with the observations of the naked eye. This differences will exist at even very high delay times. However, they will approach each other more and more until the persistent luminescence fades.

4.4.3. Temperature Dependence of Co-doped $SrAl_2O_4$

The long time decay behaviour of the three samples SA,Eu,Dy(1;1), SA,Eu,Nd (1;1) and SA,Eu,Pr(1;1) were also investigated at high (+60°C) and low (−10°C) temperatures. The decay curves were compared with the decay at ambient temperatures (approximately +22°C). However, it was not always possible to hold these temperatures because of the extremely sensitive voltage source for the Peltier element. In addition the

temperature was not always stable during the whole measurements. Consequentially, there was a maximum deviation of ±4°C over all samples. However, the absolute temperature will not be important for the discussion anyway. The aim was to compare decay curves at high, ambient and low temperatures and not at a certain definite value of temperature. Moreover water from the atmosphere condensed on the surface of the sample holder window. Hence the absolute intensity was not comparable with those of the other two measurements. The relative intensities, however, lead to sensible results because the measurement was started after the sample was in equilibrium with the atmosphere and the Peltier element.

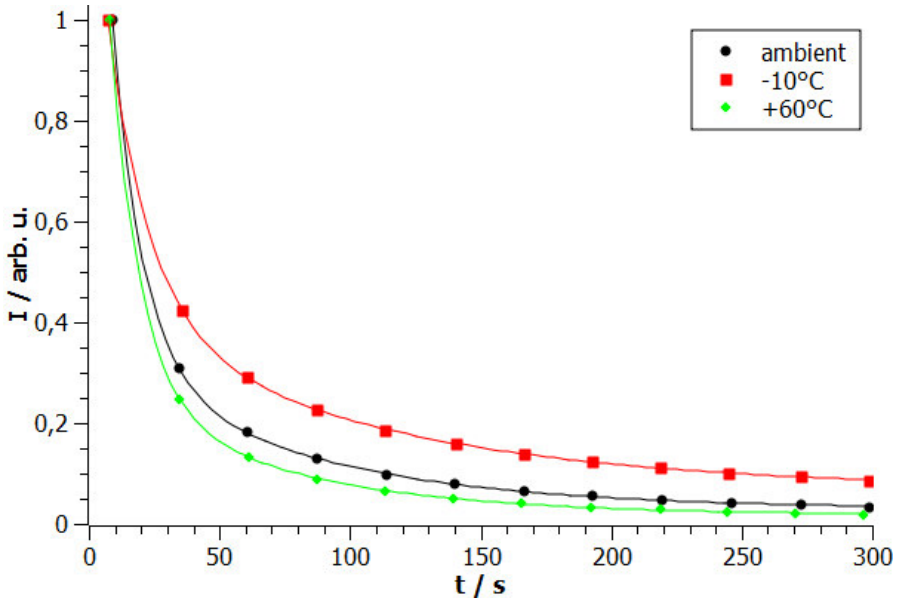

Figure 4.52.: Decay curves of SA,Eu,Dy(1;1) at ambient temperatures, −10°C and 60°C. The corresponding decay constants are given in table 4.10

Figure 4.52 shows the decay curves of SA,Eu,Dy(1;1) at different temperatures. Only the first 300 s are shown to allow a better comparison. It can be easily seen that the deeper the temperature the more intense the afterglow. Therefore the decay curve at −10°C is considerably higher than the other two decay curves. However, this is not because of the initial intensity, which is of course the same in normalised curves. This is because the curves at ambient temperature and 60°C has a faster decay than the decay curve at −10°C. This can be easily proven by the initial slope k which are getting smaller by decreasing the temperature (see table 4.10). However, the correlation between

temperature and the constant is not linear. The change from one temperature to the next higher one is not constant. The higher the temperature the smaller is the difference. A more detailed analysis of the correlation between decay constant and temperature would require more measurement points. This was not attempted in the frame of this master thesis.

Table 4.10.: The decay constants of SA,Eu,Dy(1;1) at ambient temperatures (ca. 22°C), −10°C and 60°C.

T [°C]	y_0	A_1	A_2	τ_1 [s]	τ_2 [s]	k_{LTR} [s^{-1}]
−10°C	0.07	0.37	0.94	99.2	15.7	0.064
22°C	0.03	0.32	1.47	74.1	11.7	0.131
60°C	0.02	0.28	1.51	65.5	11.2	0.139

The temperature dependence of the decay curves of samples SA,Eu,Nd(1;1) and SA,Eu,Pr(1;1) are similar.

As it was disused above all samples independent if they are co-doped with a strong or weak promoting RE show more intense afterglow at low temperatures. The details of the mechanism of persistent luminescence will be discussed in section 4.4.4. However, it can be assumed that it acts via a trapping and de-trapping mechanism. In this mechanisms a hole or electron is trapped in a vacancy or in an occupied site of the material. They stay there until they are de-trapped again. The trap has a certain depth and shape (potential energy) and the particle a certain kinetic energy. This can be treated as a particle in a 3D box with potential walls of a certain height. However, because the system is macroscopic the quantum number n is not a good quantum number anymore. Therefore the system can be described with an ensemble. Thus the kinetic energy depends on the temperature. If it is high the particle can leave the trap easily. This would shorten the time the particle is trapped and therefore confine the afterglow. If the temperature, however, is deep the particle will hardly be able to leave the trap. Hence the time the particle is trapped is enhanced and consequentially the afterglow is extended. This concept is well in agreement with the results given above.

All results are in good agreement with literature.

4.4.4. Mechanism of the Afterglow of Co-doped $SrAl_2O_4$

In order to propose a new mechanism explaining the afterglow not enough experiments could be made in the frame of this master thesis. This chapter will start with a discussion of the already existing explanations and will show why some of them can be easily rebutted. Then the individual agents of the afterglow (Eu_{Sr}, $RE^{\bullet}_{Sr}$, V''_{Sr} and $V^{\bullet\bullet}_{O}$) and their contribution to it will be discussed in detail. Finally, it will be attempted to give an explanations for the experimental results with the help of the theoretical concepts presented before.

It was already mentioned before (section 1.2.3) that the mechanism suggested by Matsuzawa et al. is based on unlikely assumptions. The oxidation states of Eu^{+} and Dy^{4+} are not stable and their definition of a hole state is also wrong.

The old mechanism proposed by Aitasalo et al. and Beauger are not supported by experimental results. It was shown that the concentration of Eu^{2+} decreases while the concentration of Eu^{3+} increases. Hence, the suggested CT is more than unlikely.

Dorenbos et al. mechanism was also questioned. It can not explain the very weak but existing afterglow without co-doping. Moreover, it was found that the de-trapping has always the same depth. Furthermore RE is not reduced during the luminescence.

Hence only the concept of Clabau et al. and the new concept of Aitasalo et al. are left which are in a way speculative but coincide with literature. However, Aitasalos mechanism includes one contradiction to literature. He claimed that Sm and Yb can form stable divalent ions. This was rebutted by XANES measurements.

Clabau as well as Aitasalo claim that electrons are the crucial charge carriers and that the trapping mechanism works via the CB. Therefore, an electron must be excited to this initially unoccupied band. This electron can come from the VB but also from an Eu^{2+} via CT. Hence Eu is oxidised to Eu^{3+}. The corresponding band of the CT is somewhere hidden in the broad band around 250 nm. However, an excitation with a wavelength located in the broad band around 340 nm, as it was done in this master thesis, will also lead to the afterglow. Here the electrons are excited from the ground state into the d orbitals of Eu^{2+}. Afterwards they can be released into the CB. This is possible because of the overlap of the d orbitals of Eu with the CB and even the V_O that are located beyond the CB. Hence the electron can be passed on from the excited

Eu^{2+} to the CB leaving behind an Eu^{3+}. This first step can be described as

$$Eu^{2+} + h\nu \rightarrow (Eu^{2+})^* \rightarrow Eu^{3+} + e^-_{CB} \tag{4.14}$$

Afterwards the electron may be trapped. Before a possible mechanism will be discussed further it might be helpful to analyse the role of all actors in the process. There are ions (Eu_{Sr}, Sr_{Sr} and $RE^{\bullet}_{Sr}$), vacancies (V''_{Sr} and $V^{\bullet\bullet}_{O}$) but also the CB that will contribute to the mechanism.

The Eu_{Sr} ion causes the luminescence and is therefore the most important actor. It will interact with light of an appropriate wavelength by exciting an electron to the d configurations. Concerning the quantum yield of the emission there are three main contributions. A non-radiative transition, an instantaneous emission of green light and a CT to the CB. The first and the second are different processes but both are fast and they result in a divalent Eu^{2+} in its ground state. These ions do not directly take part in the persistent luminescence. Neither do they change their oxidation state nor do they migrate through the material. They do have an indirect influence to the CF if they are in the vicinity of another Eu. The last process (CT), however, will end up with the formation of trivalent Eu in the ground state and an electron in the CB. This electron is free and can be trapped. After it is released it can be taken up by the trivalent Eu again. However, it is not Eu^{2+} in the ground state that is formed because the 4f orbitals do not overlap with the orbitals that transfer the electron. The generated Eu^{2+} is in the excited state. This will lead to the green $4f^6 5d^1 \rightarrow 4f^7$ transition.

Similar to the Eu_{Sr} the Sr_{Sr} units will also have no direct influence to the mechanism. They only contribute to the CF, however, do not promote the afterglow if they are near an Eu ion.

The $RE^{\bullet}_{Sr}$ symbolises the trivalent RE in $SrAl_2O_4$. Their importance to the afterglow is uncontested. How they do contribute to the afterglow, however, is still not clear. According to literature all REs except Eu^{3+} will not change their oxidation state during the persistent luminescence. The Eu^{3+} was not added purposefully and occurs either after the CT or due to residual Eu^{3+} that was not reduced during the preparation. Together with the other REs it occupies Sr sites that have one additional positive charge. This will destabilise the surrounding lattice because it normally embeds divalent Sr

ions. Consequently, the region will have an electrophile character. An electron will be therefore stabilised well and not easily released again. This effect will promote the afterglow. The question why the REs, that have similar chemical and physical properties, are behaving in such a different manner is not easy to answer. The key, however, will be the different capability of the REs to stabilise a close by electron. Whether it is the ionisation potential, the reduction potential or the ion radius that causes differences in the duration of the afterglow cannot be answered with the experiments that were done in this master thesis.

The next important actors are oxygen vacancies. They can be either empty ($V_O^{\bullet\bullet}$) or occupied by one or two electrons ($V_O^{\bullet}$ and V_O). The latter is, however, unlikely because two electrons will repeal each other. Because there exist eight different oxygen sites each of this vacancies will have eight different energy levels that are located just beyond the CB. Each of the eight $V_O^{\bullet\bullet}$ can trap the electrons that were released to the CB. This electrons can either be de-trapped again or transferred to other vacancies in the vicinity of the trap. The time an electron will stay in such a trap depends on its thermal energy and on the depth of the trap. Therefore, if an oxygen vacancy is stabilised its trap depth will increase and the afterglow will be enhanced. A $V_O^{\bullet\bullet}$ is a defect with a depletion of negative charge. Therefore, it will be energetically favourable for the material to trap electrons in these vacancies. This will especially occur if the $V_O^{\bullet\bullet}$ are near the trivalent RE that also lead to an electron depletion of the surrounding. The whole arrangement of $V_O^{\bullet\bullet}$, $RE_{Sr}^{\bullet}$ and electron will be stabilised. Hence the trap depth of such an arrangement will be more increased than that one of an arrangement without a RE in the vicinity. Nevertheless, the afterglow occurs also without the presence of the REs. However, this simple concept does not explain why Sm even reduces the afterglow. There must be a crucial property that is considerably different for all RE and that influences the duration of the afterglow much more than the stabilisation described above.

Another possibility to stabilise the $V_O^{\bullet\bullet}$ is given by V_{Sr}''. Their contribution to the afterglow is indirect. Contrary to what is suggested by literature they cannot trap a hole because they are empty and hence they have no electron to remove. However, they have a lack of positive charge and can therefore stabilise the formally positively charged $V_O^{\bullet\bullet}$ and $RE_{Sr}^{\bullet}$. Hence they will decrease the trap depth because of the depletion

of positive charge. The formation of V''_{Sr} can be either intrinsic or extrinsic. Although no corresponding measurements were made it can be assumed that the latter effect is predominant because intrinsic effects are usually far beyond 1%. Therefore co-doping can also reduce the afterglow. The effects, however, will be small and the promotion of the $RE^{\bullet}_{Sr}$ will be predominant.

The CB is formed by unoccupied orbitals. The only function of the CB in the mechanism is to pass on the electrons to the vacancies or back to the Eu to prompt luminescence.

The mechanism can be summed up with following equations. The first step will be equation 4.14. In the next step the electron is trapped by an oxygen vacancy

$$e^{-}_{CB} + V^{\bullet\bullet}_{O(A)} \rightarrow V^{\bullet}_{O(A)} \rightleftharpoons V^{\bullet}_{O(B)} \rightleftharpoons V^{\bullet}_{O(C)} \tag{4.15}$$

Here the indices A, B and C imply three of the six different oxygen sites. This vacancies can be stabilised by the RE ions.

$$[V^{\bullet}_{O}][RE^{\bullet}_{Sr}] \tag{4.16}$$

This stabilisation, however, is superimposed by a much stronger intrinsic effect of the RE. Otherwise there would be no explanation why some RE promote the afterglow better than others and why some RE even reduce the afterglow. The de-trapping will be controlled thermally. If the thermal energy of the electron is high enough it will escape the trap and initiate the afterglow described by the back reactions of equations 4.15 and 4.14.

All in all there are two mechanisms that lead to luminescence [42, 15]. Only one of them, however, will lead to a delayed emission. Both start with an excitation of Eu^{2+}. Now the electron can be either be released to the CB or de-excite to the ground state by emitting a photon. The latter describes a direct excitation by light followed by instant emission. The former process, however, will end up in an Eu^{3+} in the ground state. When the electron returns back to Eu an excited Eu^{2+} will be formed again that initiates the emission. Hence the second process describes an indirect excitation via the CB. The delay of this emission, however, depends on the surrounding of the Eu. Because the electrons do not move a long distance via the CB there must be a trap level ($V^{\bullet\bullet}$

$_O$ stabilised by a RE ion) in the vicinity of the Eu to yield a strong promotion of the afterglow. Hence the probability that a RE ion will be found close to an Eu at doping concentrations of 1% is of interest. It can be assumed that the embedding of the RE into the host material during solution combustion is a random process. The probability that the Eu and the RE occupy the two octahedra that share a face is about 0.01%. The remaining arrangements correspond predominantly to Eu near Sr ions. Hence the radiative deexcitation without afterglow should be about $10,000$ times stronger. This is about the order of magnitude in the difference between the intensities of the emission spectrum recorded without delay and the emission spectra of the long time range. This provides evidence that the RE do not only influence the afterglow but also need to be near an Eu.

5. Summary

In the frame of this master thesis four series of samples were prepared by the solution combustion method at a temperature of 600°C followed by a sintering step of two hours at a temperature of 1100°C. The sintering conditions were reducing (90% N_2, 10% H_2) except for the Eu^{3+} containing sample (air). The samples were:

- undoped $SrAl_2O_4$ (unsintered, sintered once and twice)
- doped $SrAl_2O_4$: RE (1%) (with RE equals Eu^{2+}, Eu^{3+}, Dy^{3+}, Nd^{3+}, Pr^{3+} and Sm^{3+})
- co-doped $SrAl_2O_4$: Eu, Dy (x%;y%) (with (x;y) equals (0.5;0.25), (0.5;0.5), (0.5;1), (1;0.5), (1;1) and (1;2))
- co-doped $SrAl_2O_4$: Eu, RE (1%;1%) (with RE equals Dy, Nd, Pr and Sm)

The first series was analysed with XRD, SEM and reflectance spectroscopy. The XRD showed that the samples sintered once had the best crystallographic properties in terms of crystallinity and phase purity. Therefore, all following samples were prepared with one sintering step only. The crystal lattice has two different Sr sites that can be substituted by REs. The SEM showed that the $SrAl_2O_4$ crystallizes in needle and ball shaped aggregates. These structures consist of different variants of the monoclinic α-phase with twin relationships. The unsintered sample considerably differs from the sintered one. The former consists of smaller crystallites. The reflectance spectrum showed that undoped $SrAl_2O_4$ does not absorb visible light. The optical band gap was determined via a Tauc plot. The result was a band gap of 4.29 eV which is in bad agreement with the 6.5 eV reported in the literature.

In the emission spectra of unsintered $SrAl_2O_4$: Eu (1%) three emission centres were established. One corresponds to Eu^{2+}, one to Eu^{3+} and the last one presumably to a second Eu^{2+} containing phase. The sintered spectra, however, showed only one

emission centre (Eu^{2+} or Eu^{3+}) depending on the sample's preparation. The afterglow for sintered $SrAl_2O_4$: Eu^{2+} (1%) lasted only some hundredths of a microsecond. All other singly doped samples showed the characteristic spectrum of the respective RE. Their intensity, however, is much weaker than for the Eu doped sample.

Within the third series of samples the intensity depended on the concentrations. The higher the concentration of Eu and the lower the concentration of Dy the more intense was the signal. The afterglow was analysed in two different time ranges. The short time range started from 0 ms and ended with 10 ms. The long time range ranged from approximately 6 s to 15 minutes. The decay curves showed that the higher the Eu concentration and the higher the Dy concentration the more intense was the afterglow. Samples with high Eu/Dy ratio started at a higher level of intensity but ended at a lower level of intensity than samples of low Eu/Dy ratios. This crossing of the decay curves started in the short time range and ended in the time gap that was not accessible for measurements. In the long time range, however, all samples independent of their composition showed a similar decay behaviour. This means that co-doping does not enhance the duration of the afterglow but its intensity. The sample $SrAl_2O_4$: Eu, Dy (1%;1%) showed the best afterglow properties in terms of duration and intensity. Hence, all co-doped samples were prepared with this concentrations.

The forth series of samples was analysed with fluorescence spectroscopy at low ($-10°C$), ambient (22°C) and at high (60°C) temperatures. The decay curves showed that the intensity of the afterglow increases with decreasing the temperature. This result was the same for all co-dopants. The intensity of the emission spectrum, however, varied from sample to sample.This indicates that the quantum yield of Eu^{2+} is influenced by the co-dopant. The co-dopants Dy and Nd promote the afterglow considerably. Co-dopant Pr enhances the afterglow intensity only slightly and Sm even reduces the afterglow intensity.

Appendix

Appendix A.

Eu Containing Compounds

The commercially available RE compounds are mainly oxides. For the solution combustion, however, they need to be converted into nitrates. Because Eu played the central role in this thesis it was decided to synthesise $Eu(NO_3)_3$ from the oxide. The product can then be used for the preparation with solution combustion method without any further addition of nitric acid.

Of both materials $Eu(NO_3)_3 \cdot nH_2O$ as well as Eu_2O_3 reflectance spectra were recorded with the reflectance spectrometer. This was done to demonstrate two characteristic properties of RE in solids: the nearly independence of the CF splitting of the host material and the origin of hot bands.

The corresponding reaction equation for the synthesis of $Eu(NO_3)_3$ is

$$Eu_2O_3 + 6HNO_3 \longrightarrow 2Eu(NO_3)_3 + 3H_2O$$

Consequential the needed masses can be calculated.

Eu_2O_3 was weighted into a beaker and the stoichiometric amount of 53% nitric acid was added. However, Eu_2O_3 barely dissolved in the small volume of HNO_3. In order to avoid undissolved Eu_2O_3 in the final product, one additional Pasteur pipette of acid was added. The solution was murky and colourless. The beaker was put onto a magnetic stirrer at 80°C. No lid was used to enable the water and excess of the acid to evaporate. After 1.5 hours of stirring the solution turned into a colourless, translucent gel. The glassy substance covered the whole surface of the beaker. It was flexible and could be easily scratched by a spatula. The beaker was put into a drying cabinet at a temperature of 60°C. After three hours the first crystals formed in the edge of the

beaker. The surface of the gel was thoroughly scratched with a spatula to enhance the surface. This was repeated every one to two hour. After one week the majority of nitric acid and water was evaporated. The product was a mainly colourless powder with yellowish areas. The colourless parts seemed to form a pure phase whereas the yellowish part was still a soft gel that could be easily squashed by a spatula. Then the powder was transferred into a large crystallising dish and dispersed on the bottom to provide a large surface. After five days the sample was ground in an agate mortar and dried for another day. Finally the now completely colourless powder was filled into a sample vial.

However, before the sample can be used immediately the chemical formula, or more precisely the chemically bounded water needed to be determined. This was done by thermo gravimetric analysis (TGA) and differential scanning calorimetry (DSC). The results of the measurement can be seen in figure A.1. The measurement equipment was a *STA 449C Jupiter* with a *Protheus Analysis* software of *Netzsch*.

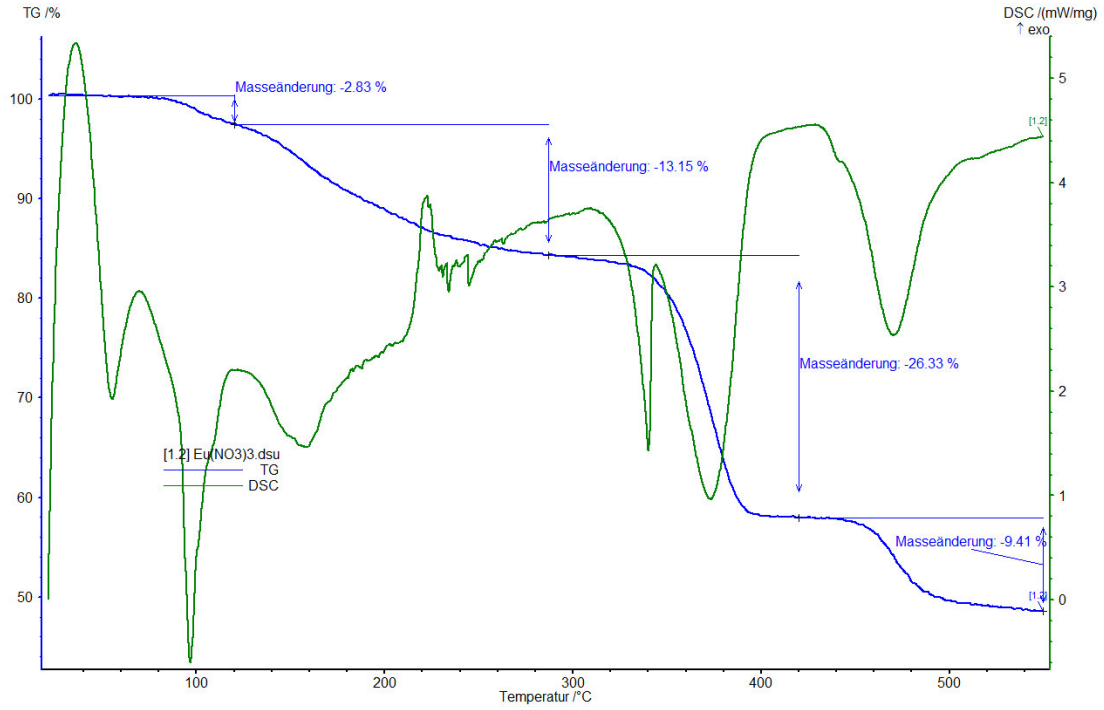

Figure A.1.: TGA and DSC of $Eu(NO_3)_3 \cdot 3H_2O$: the blue line show the TGA. The losses are relative values. The green line show the DSC. The positive values correspond to an exothermic reaction.

The blue line shows the TGA with sample losses in percent. There are four different mass losses. The first loss is 2.83% and is around a temperature of 100°C. It was assumed that this is the evaporation of physically bound water. The second loss is 13.15% and ranges from approximately 120 to 280°C. This was considered as the loss of chemically bound water. The next two losses describe the further decomposition of the substance. Thus it is not important for the determination of the chemical formula.

Therefore it can be assumed that the first two steps only describe a mass loss of chemically or physically bound water. Consequently, the chemical formula at 300°C is $Eu(NO_3)_3$. The following three correlation can be set up

$$(1 - \frac{x_{ml}}{100})M_r' = M_r(Eu(NO_3)_3) \tag{A.1}$$

$$M_r'\text{–}M_r(Eu(NO_3)_3) = m_{H_2O} \tag{A.2}$$

$$m_{H_2O} = nM_r(H_2O) \tag{A.3}$$

With x_{ml} as the mass loss in %, $M_r(Eu(NO_3)_3)$ as the molecular mass of $Eu(NO_3)_3$, M_r' as the molecular mass of the substrate or intermediate, m_{H_2O} as the mass of water, n as the stoichiometric coefficient of water and $M_r(H_2O)$ as the molecular mass of water. After rearranging and combining equations A.1, A.2 and A.3 following correlation is obtained

$$n = \frac{x_{ml}M_r(Eu(NO_3)_3)}{M_r(H_2O)(100 - x_{ml})} \tag{A.4}$$

Here x_{ml} equals either 2.83%, 13.15% or 15,98%, $M_r(Eu(NO_3)_3)$ equals 337.985 g/mol and $M_r(H_2O)$ equals 18.016 g/mol. The calculated value of n for the first loss is 0.55. It is the stoichiometric constant for the physically absorbed water. For the second mass loss n yields 2.84. The stoichiometric constant must be an integer or at least a rational number. The closest integer is 3. This gives a deviation of approximately 5%. Nevertheless the result lies within the confidence interval because of several

uncertainties that influenced the calculation (instrumental and operator bias, rounding of numbers, ...). Hence the chemical formula of the sample is $Eu(NO_3)_3 \cdot 3H_2O$.

The determination of the other two mass losses, however, is not so simple. It was tried to find agreement with multiples of gases like O_2, NO_2, NO, N_2O or N_2. None of them led to sensible results.

The green line shows the DSC. It indicates the direction and magnitude of the heat flows. All process except the evaporation of the physically bound water around 100°C are exothermic. The magnitude of the heat flow varies considerably.

As already mentioned both compounds $Eu(NO_3)_3 \cdot 3H_2O$ as well as Eu_2O_3 can be used for the preparation of doped $SrAl_2O_4$, the first directly the second after a pretreatment with nitric acid. The reflectance spectra of both substances at ambient temperatures are shown in figure A.2. Both spectra were baseline corrected. Nevertheless the spectrum of $Eu(NO_3)_3 \cdot 3H_2O$ has a much lower reflectance at all wavelengths. This is because of the different absorption habits of the host material. The position and the relative intensity of the absorption bands in both spectra are about the same although the host materials generate completely different CF. Moreover not all bands that arise because of the CF splitting are resolved in the spectra. For instance the ${}^7F_0 \rightarrow {}^5D_3$ should show four to seven bands depending on the symmetry of the crystal. However, only one band can be observed. The same applies for most other bands. This is due to the limited resolution of the spectrometer.

There are two transitions that are of certain interest to investigate. First the hypersensitive transition ${}^7F_0 \rightarrow {}^5D_2$. It is highly sensitive to the symmetry of the REs site. In particular, it is known that the intensity of hypersensitive transitions goes to zero when the RE ion is located at a centre of inversion in the crystal structure. However, it has about the same intensity in both materials. Consequentially, the Eu site of both materials is not an inversion centre.

The second band is the the ${}^7F_0 \rightarrow {}^5D_0$ transition that is not degenerate. Hence only one band is expected. Nevertheless there can be clearly seen at least two bands. This is because of the hot bands that already occur at ambient temperatures. Figure A.3 gives a better resolution of the transition. In the case of $Eu(NO_3)_3 \cdot 3H_2O$ there can be seen a narrow band at about 571.5 nm, a broad band at 582.5 nm and two or three bands

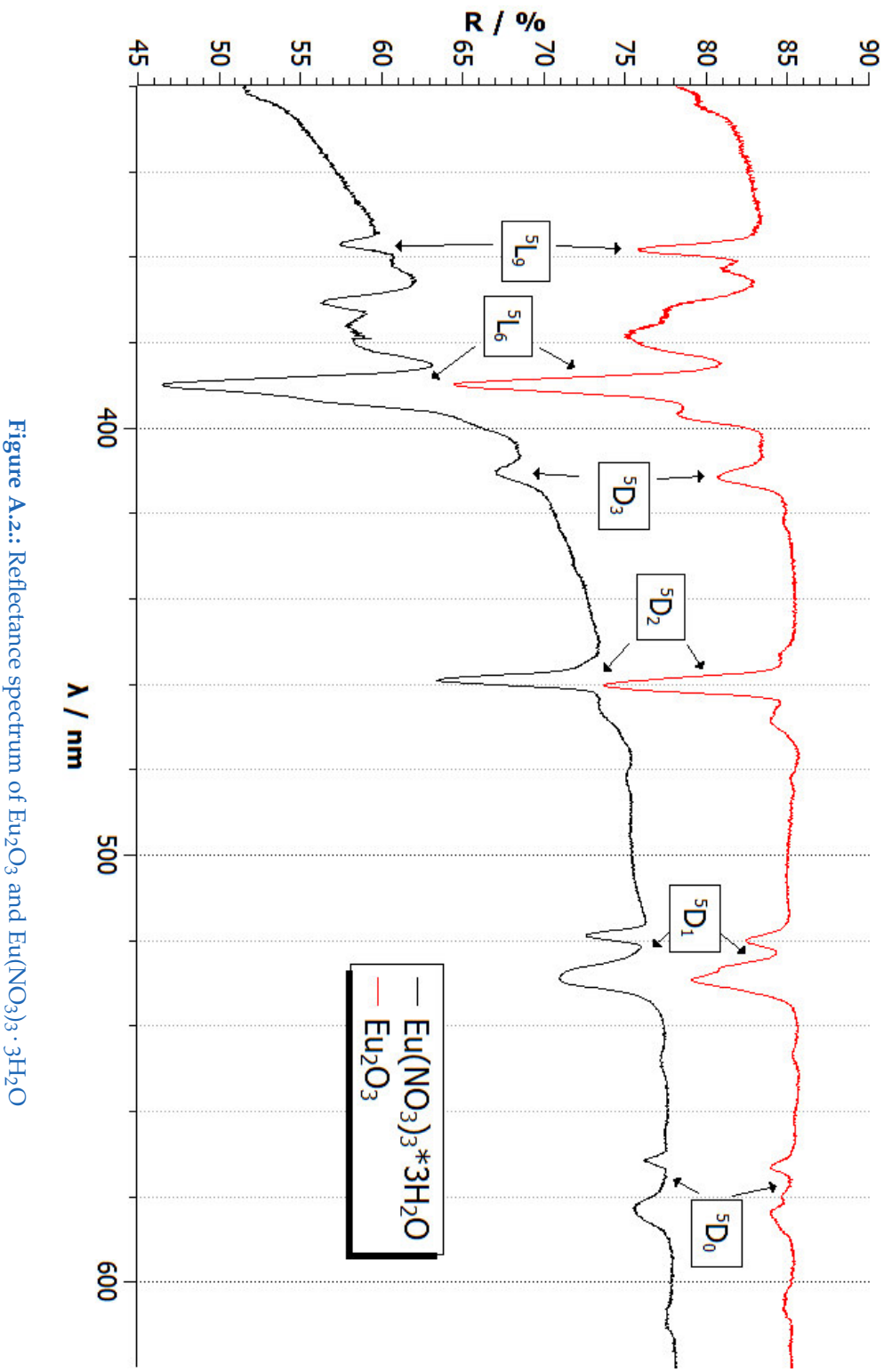

Figure A.2.: Reflectance spectrum of Eu_2O_3 and $Eu(NO_3)_3 \cdot 3H_2O$

around 610 nm. The first is the $^7F_0 \rightarrow^5 D_0$ transition. It is narrow because both energy levels are non-degenerate. The broad band corresponds to the $^7F_1 \rightarrow^5 D_0$. Here the ground state is degenerate. All three lines are close together and cannot be resolved - a broad band emerges. The bands around 610 nm are the $^7F_2 \rightarrow^5 D_0$ transitions. Theoretically, they should consist of five bands. However, the $^7F_2$ is barely populated. Therefore the transition is low in intensity.

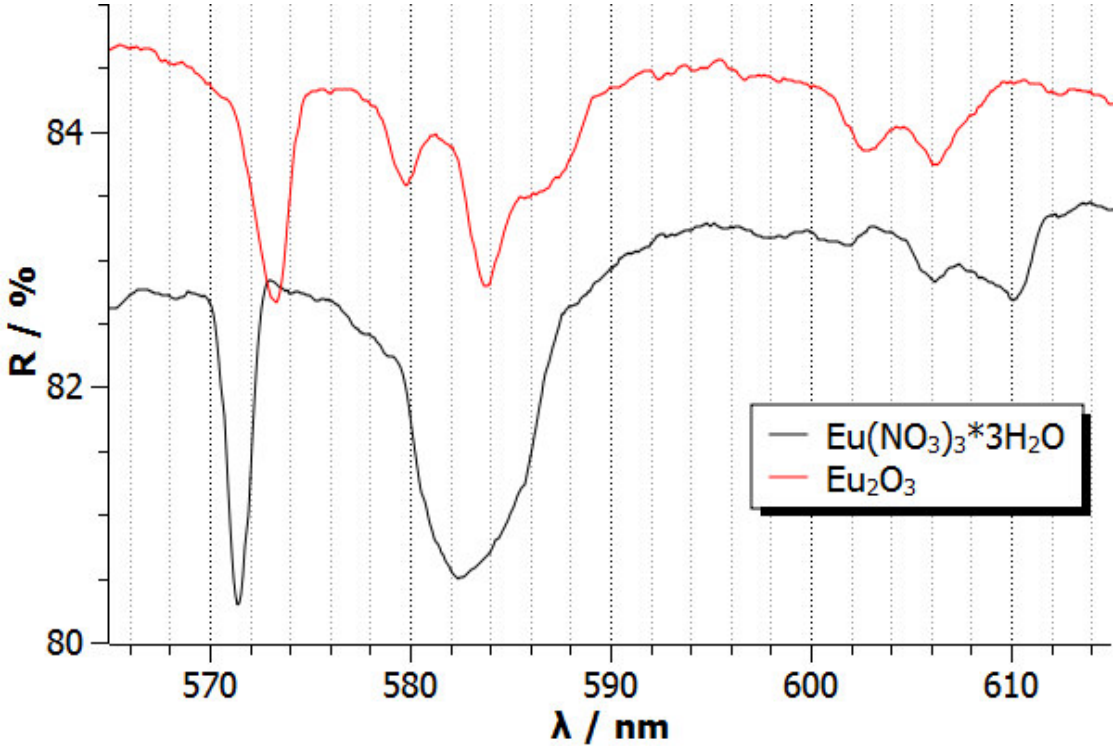

Figure A.3.: $^7F_{0-2} \rightarrow^5 D_0$ transition of Eu_2O_3 and $Eu(NO_3)_3 \cdot 3H_2O$: $Eu(NO_3)_3 \cdot 3H_2O$ has only one Eu site. Therefore the bands in the spectrum are hot bands. However, Eu_2O_3 has two Eu sites. Hence the bands in the spectrum emerge due to the populated higher ^7F_J terms and due to the two Eu sites in the material.

Lamp:	W	Detector:	PMT	Start:	620 nm
End:	560 nm	Step size:	0.1 nm	Slit size:	1 nm

The interpretation for Eu_2O_3 is not so simple. It is a sesquioxide that has two different Eu sites. Both sites have a different CF. Although the effect is small it is large enough to superpose with the hot bands. The left band can be allotted to the $^7F_0 \rightarrow^5 D_0$ of the first site. The other bands, however, are difficult to assign. Measurements at deeper temperatures would extinguish the hot bands and make things more clear.

Hence the spectrum would only display the two $^7F_0 \rightarrow ^5 D_0$ transitions of the two Eu sites. However, the spectrometer does not feature a cooling system to enable such measurements.

Appendix B.

$SrAl_2O_4$: Nd (100%)

Undoped $SrAl_2O_4$ has a monoclinic crystal structure. The same applies for (co-)doped systems with small doping concentrations. However, at a certain doping concentration the structure must change because divalent Sr atoms are substituted with trivalent REs. Therefore it was decided to synthesise $SrAl_2O_4$: Nd (100%) and to analyse it by XRD and reflectance spectroscopy. Nd was chosen because of its good absorption properties in the Vis and NIR range.

The XRD spectrum and all measurement conditions are shown in figure B.1. Although the stoichiometric ratios of the preparation was 1:2:4, the empirical formula that was found is $NdAlO_3$. In addition the powder is single phase. It has a rombohedral perovskite structure. There is only one Nd site.

The reflectance spectrum was measured at ambient temperatures and is given in figure B.3. It shows all transitions from the ${}^4I_{9/2}$ ground level to the CF split RS multiplets. The ${}^4I_{9/2} \rightarrow {}^2P_{1/2}$ transition is of particular interest because the final state is not degenerate. Nevertheless there can obviously be seen at least two peaks. A detailed view of this range discloses that there are three bands (figure B.2). They needed to be smoothed by a Savitzky-Golay algorithm because of the already high zoom and the limited resolution. These three bands emerge because of the hot band system. Different from Eu^3+ it is not due to the next higher RS level that is already too high in energy to be populated at room temperature. However, the ground state is CF split. These levels are populated at ambient temperature and consequently lead to the hot band system.

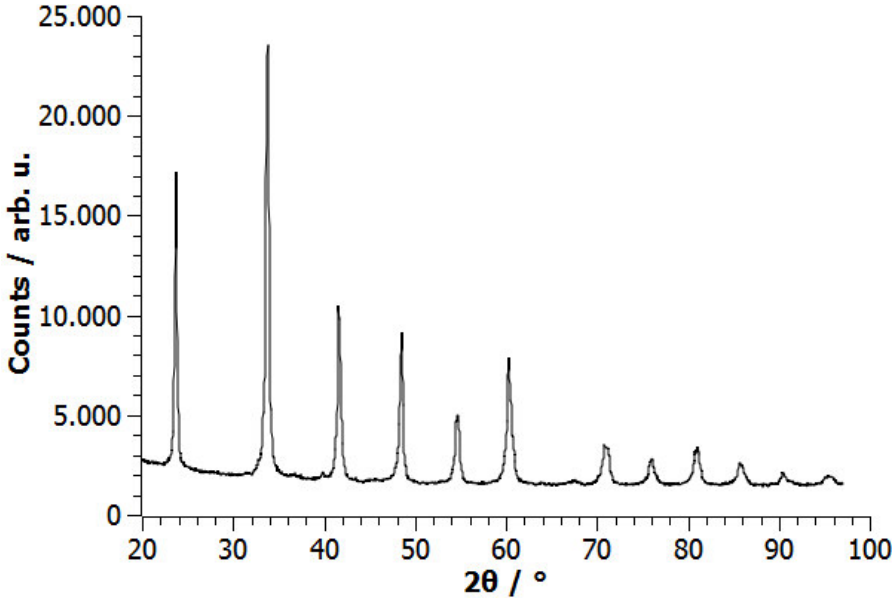

Figure B.1.: XRD spectrum of $NdAlO_3$.

Start	20°θ	End	96.98°θ	Step size	0.02°θ
Receiving slit	0.1 mm	Anode	Cu	K-α1	1.5406 $\AA$

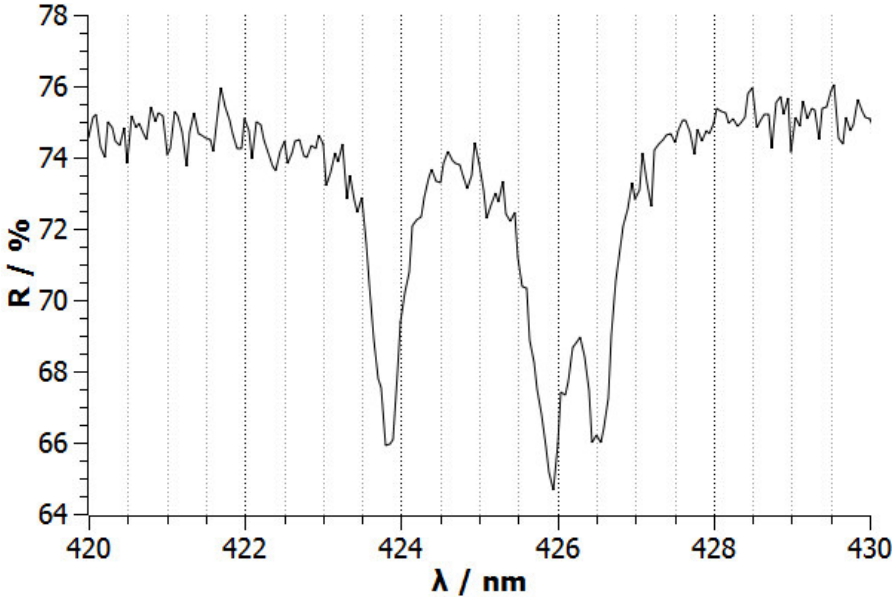

Figure B.2.: $^4I_{9/2} \rightarrow^2 P_{1/2}$ transition of $NdAlO_3$: All bands in the spectrum are hot bands. They emerge because the ground state is CF split.

Lamp	W	Detector	PMT	Start	440 nm
End	400 nm	Step size	0.05 nm	Slit size	0.2 nm

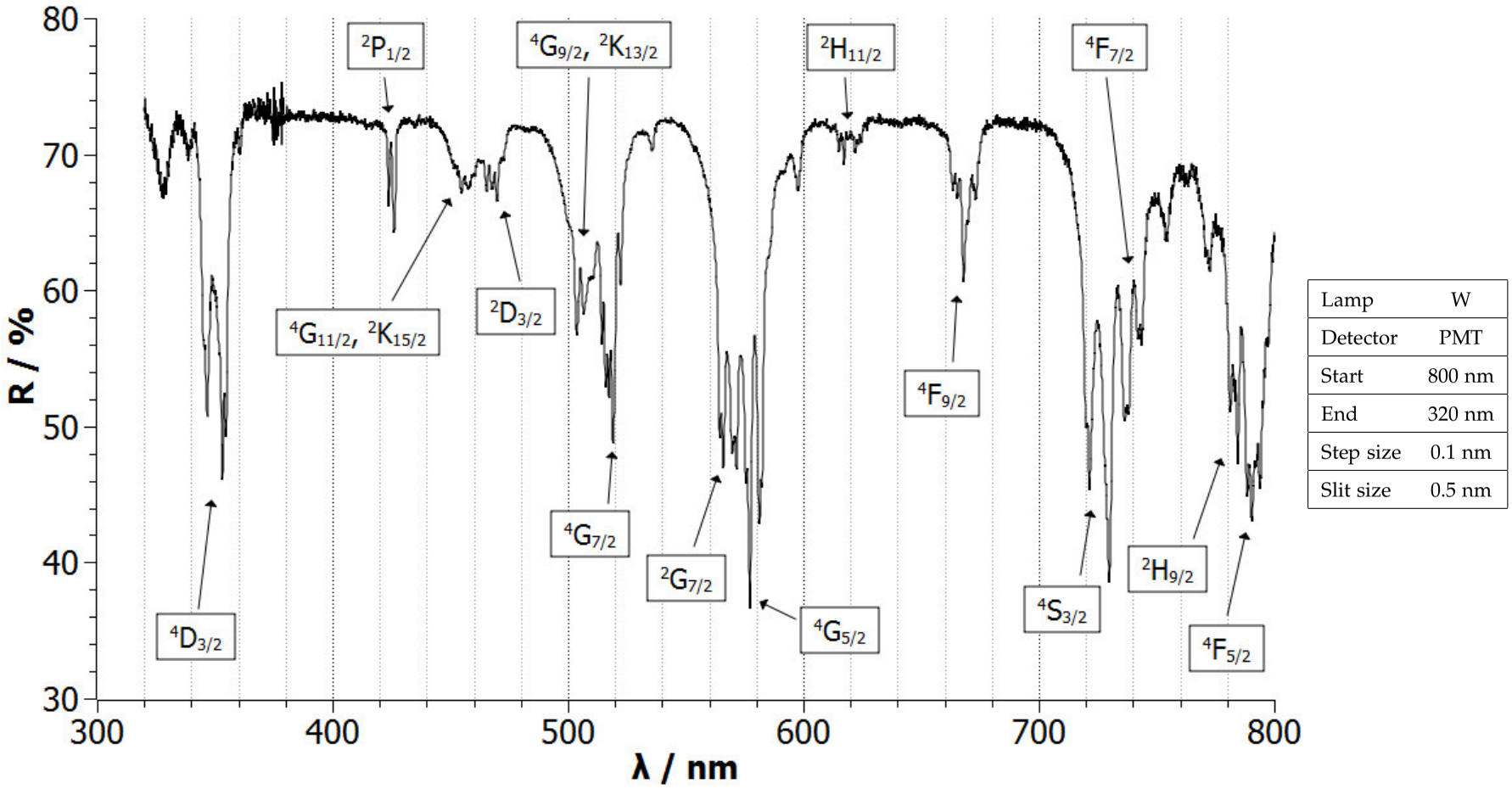

Lamp	W
Detector	PMT
Start	800 nm
End	320 nm
Step size	0.1 nm
Slit size	0.5 nm

Figure B.3.: Reflectance spectrum of $NdAlO_3$.

Appendix C.

Dieke Diagram

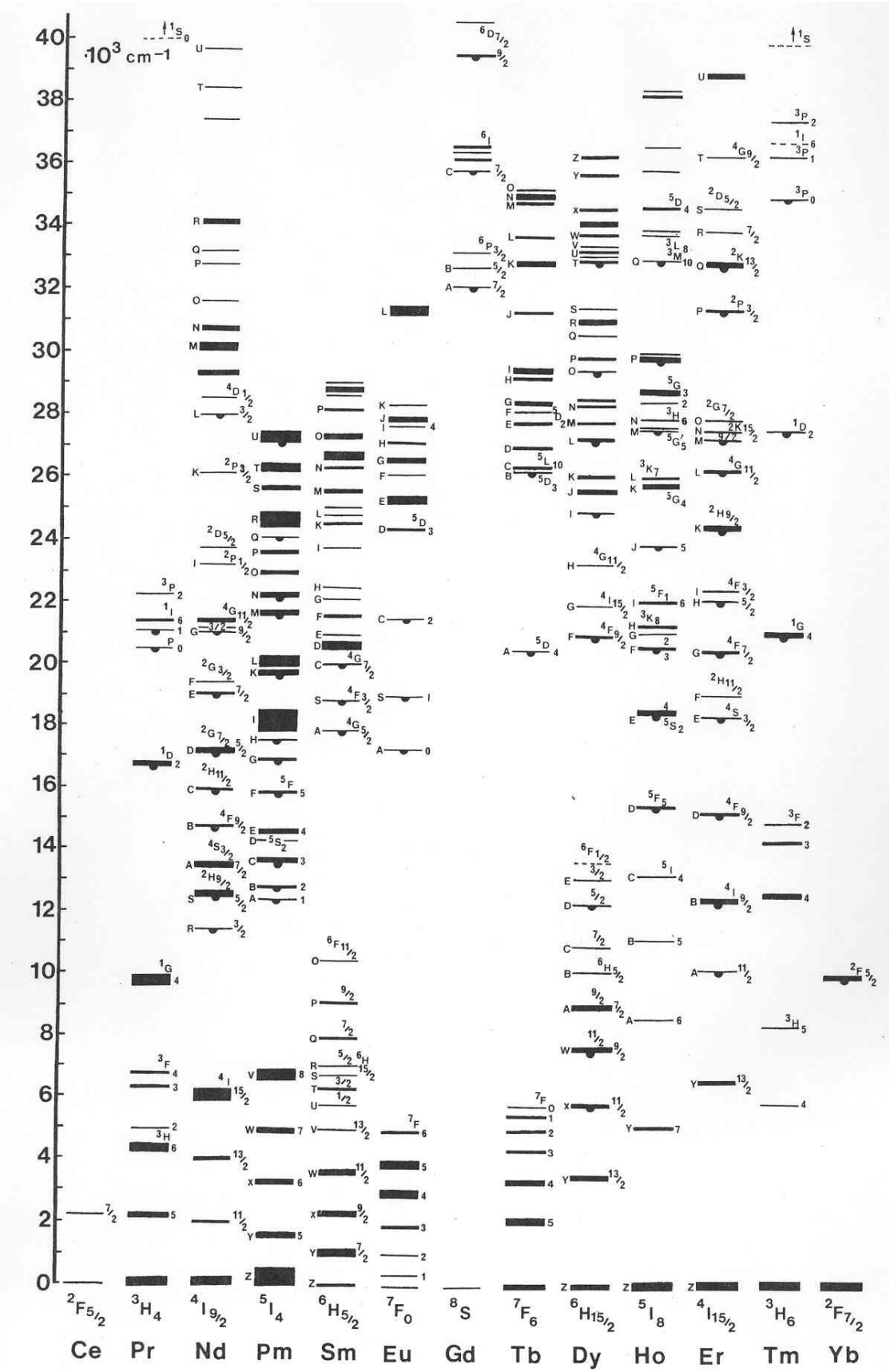

Figure C.1.: The Dieke diagram for all RE^{2+} from Ce to Yb [19].

Appendix D.

EDXA of Figure 4.14

P:\projects\projects by number\146xx\14653_TUG_Gatterer_pp\ux12163.spc

Label:ux12163: SrAl2O4, u88657-1, 10kV

kV:10.0 Tilt:0.0 Take-off:35.0 Det: Octane Super

Res:129 Amp.T:7.68 FS:28978 Lsec:50 10-Jul-2015 11:46:08

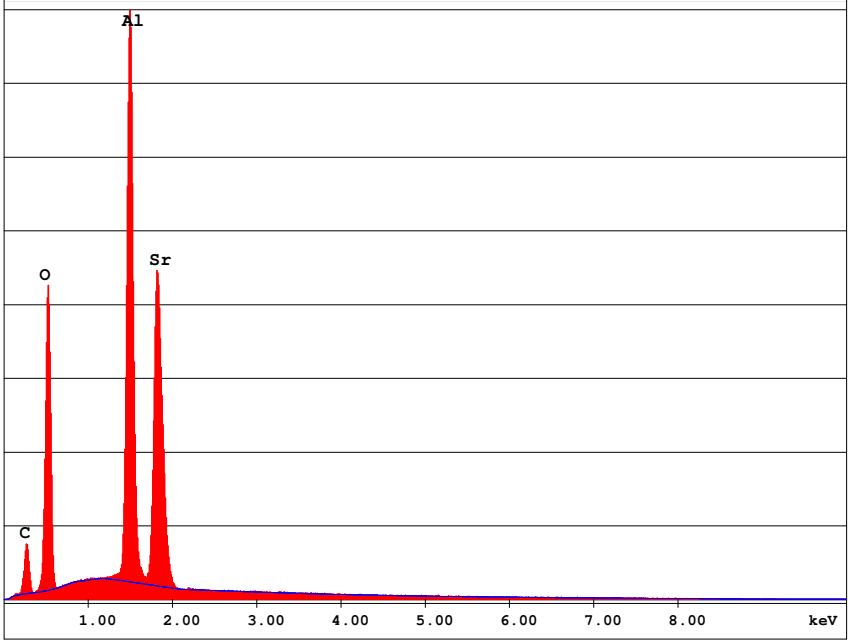

EDAX PhiRhoZ Quantification (Standardless)
Element Normalized
SEC Table : User X:\shared data\guests\Thomas Meier\spektra_sec_20140819\sec-genesis-u

Element	Wt %	At %	K-Ratio	Z	A	F
O K	29.55	55.54	0.1416	1.2124	0.3952	1.0003
AlK	26.30	29.31	0.2482	1.0691	0.8758	1.0079
SrL	44.15	15.15	0.3284	0.8203	0.9067	1.0000
Total	100.00	100.00				

Element	Net Inte.	Bkgd Inte.	Inte. Error	P/B
O K	1519.16	53.92	0.38	28.17
AlK	3662.19	137.92	0.24	26.55
SrL	2340.14	119.06	0.31	19.66

Figure D.1.: EDXA of area 1 in figure 4.14.

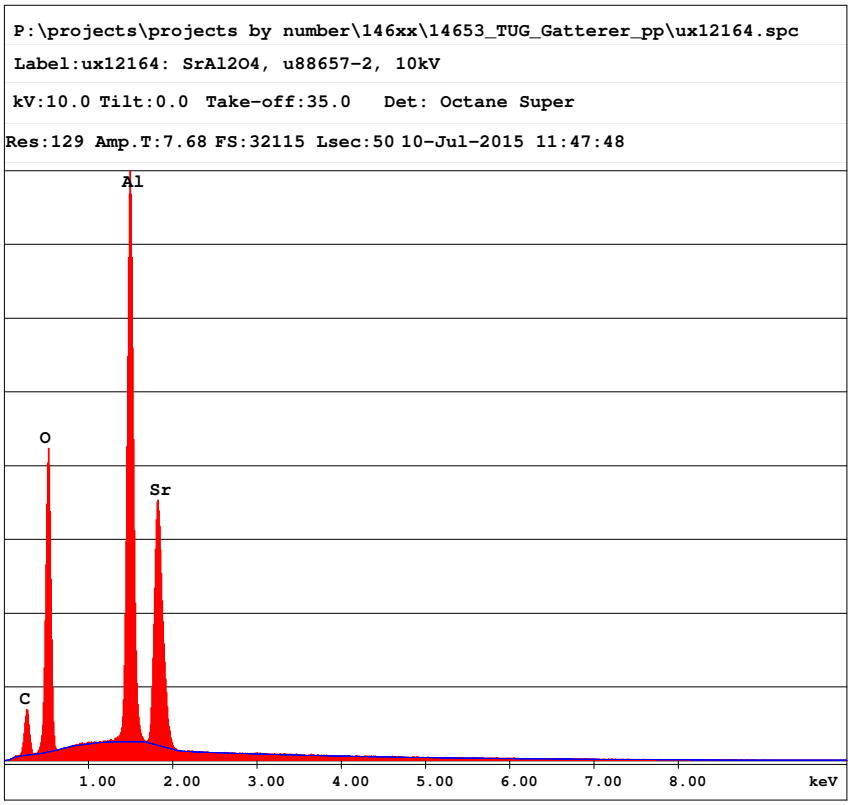

EDAX PhiRhoZ Quantification (Standardless)
Element Normalized
SEC Table : User X:\shared data\guests\Thomas Meier\spektra_sec_20140819\sec-genesis-ul

Element	Wt %	At %	K-Ratio	Z	A	F
O K	31.63	56.27	0.1569	1.1940	0.4154	1.0003
AlK	29.47	31.09	0.2746	1.0526	0.8793	1.0068
SrL	38.90	12.64	0.2816	0.8075	0.8964	1.0000
Total	100.00	100.00				

Element	Net Inte.	Bkgd Inte.	Inte. Error	P/B
O K	1677.20	54.92	0.36	30.54
AlK	4037.92	161.42	0.23	25.02
SrL	1999.82	148.64	0.34	13.45

Figure D.2.: EDXA of area 2 in figure 4.14.

Bibliography

[1] IUPAC: luminescence. http://goldbook.iupac.org/L03641.html (2015-09-03).

[2] T. Jüstel, H. Nikol, C. Ronda, Angew. Chem. Int. 37 (1998) 3084-3103.

[3] T. Jüstel; FH Münster, Lecture on Incoherent Light Sources.

[4] J. Hölsä; ECS Interface 18 (2009) 42-45.

[5] X. Qu, L. Cao, W. Liu, G. Su, P. Wang, I. Schultz; Mater. Res. Bull. 47 (2012) 1598-1603.

[6] H. Swart, J. Terblans, O. Ntwaeaborwa, E. Coetsee, B. Mothudi, M. Dhlamini; Nucl. Instrum. Methods 267 (2009) 2630-2633.

[7] L. Jiang, C. Chang, D. Mao; J. Alloy. Compd. 360 (2003) 193-197.

[8] H. Matsuo, K. Ikeda, S. Hata, H. Nakashima, H. Yamada, C. Xu; J. Alloy. Compd. 577 (2013) 507-516.

[9] H. Lange; US Patent 3294699 (1966).

[10] T. Matsuzawa, Y. Aoki, N. Takeuchi, Y. Murayama; J. Electrochem. Soc. 143 (1996) 2670-2673.

[11] T. Katsumata, T. Nabae, K. Sasajima, S. Komuro, T. Morikawa; J. Electrochem. Soc. 144 (1997) 243-245.

[12] D. Wang, Q. Yin, Y. Li, M. Wang; J. Lumin. 97 (2002) 1-6.

[13] T. Katsumata, S. Toyomane, R. Sakai, S. Komuro, T. Morikawa; J. Am. Ceram. Soc. 89 (2006) 932-936.

[14] J. Kingsley, K. Suresh, K. Patil; J. Solid State Chem. 87 (1990) 435-442.

[15] Z. Qiu, Y. Zhou, M. Lü, A. Zhang, Q. Ma; Acta Mater. 55 (2007) 2615-2620.

[16] T. Peng, H. Yang, X. Pu, B. Hu, Z. Jiang, C. Yan; Mater. Lett. 58 (2003) 352-356.

[17] X. Yu, C. Zhou, X. He, Z. Peng, S. Yang; Mater. Lett. 58 (2003) 1087-1091.

[18] E. Shafia, M. Bodaghi, M. Tahriri; Curr. Appl. Phys. 10 (2010) 596-600.

[19] S. Hüfner; Optical Spectra of Transparent Rare Earth Compounds, Academic Press, New York (1978) chapter 2.

[20] Physics: Is there experimental evidence for the model of discrete intervals and orbital distances for electrons around the atomic nucleus?. http://physics.stackexchange.com/questions/186837/is-there-experimental-evidence-for-the-model-of-discrete-intervals-and-orbital-d (2015-09-08).

[21] V. Abbruscato; J. Electrochem. Soc. 118 (1971) 930-930.

[22] T. Aitasalo, J. Hölsä, H. Jungner, M. Lastusaari, J. Niittykoski; J. Lumin. 94-95 (2001) 59-63.

[23] C. Beauger; Thesis, Université de Nice, Nice, France (1999).

[24] F. Clabau, X. Rocquefelte, S. Jobic, P. Deniard, M. Whangbo, A. Garcia, T. Le Mercier; Chem. Mater. 17 (2005) 3904-3912.

[25] F. Clabau, X. Rocquefelte, T. Le Mercier, P. Deniard, S. Jobic, M. Whangbo; Chem. Mater. 18 (2006) 3212-3220.

[26] P. Dorenbos; J. Electrochem. Soc. 152 (2005) H107-H110.

[27] T. Aitasalo, J. Hölsä, H. Jungner, M. Lastusaari, J. Niittykoski; Phys. Chem. B 110 (2006) 4589-4598.

[28] S. Carlson, J. Hölsä, T. Laamanen, M. Lastusaari, M. Malkamäki, J. Niittykoski, R. Valtonen; Opt. Mater. 31 (2009) 1877-1879.

[29] J. Hölsä, T. Laamanen, M. Lastusaari, M. Malkamäki, E. Welter, D. Zajac; Spectrochim. Acta, Part B 65 (2010) 301-305.

[30] F. Clabau, X. Rocquefelte, S. Jobic, P. Deniard, M. Whangbo, A. Garcia, T. Le Mercier; Solid State Sci. 9 (2007) 608-612.

[31] S. Ekambaram, K. Patil, M. Maaza; J. Alloy. Compd. 393 (2005) 81-92.

[32] Database of Ionic Radii. http://abulafia.mt.ic.ac.uk/shannon/ptable.php (2015-09-03).

[33] E. Shafia, M. Bodaghi, S. Esposito, A. Aghaei; Ceram. Int. 40 (2014) 4697-4706.

[34] R. Chen, Y. Wang, Y. Hu, Z. Hu, C. Liu; J. Lumin. 128 (2008) 1180-1184.

[35] D. Kshatri, A. Khare; J. Lumin. 155 (2014) 257-268.

[36] F. Palilla, A. Levine, M. Tomkus; J. Eletrochem. Soc. 115 (1968) 642-644.

[37] Y. Zhou, J. Lin, S. Wang, H. Zhang; Opt. Mater. 20 (2002) 13-20.

[38] R. Sakai, T. Katsumata, S. Komuro, T. Morikawa; J. Lumin. 85 (1999) 149-154.

[39] H. Kubo, H. Aizawa, T. Katsumata, S. Komuro, T. Morikawa; J. Cryst. Growth 275 (2005) e1767-e1771.

[40] G. Ju, L. Chen, X. Wang, Z. Mu; Phys. B 415 (2013) 1-4.

[41] D. Kshatri, A. Khare, P. Jha; Chalcogenide Lett. 10 (2013) 121-129.

[42] Y. Kamiyanagi, M. Kitaura, M. Kaneyoshi; J. Lumin. 122-123 (2007) 509-511.